

**Dissertation zur Erlangung des Doktorgrades
Der Fakultät für Chemie und Pharmazie
Der Ludwig-Maximilians-Universität München**

**Tip-enhanced Near-Field Optical
Spectroscopy on Single-Walled Carbon
Nanotubes**

von
Huihong Qian
aus
Jiangsu, China

Juli, 2008

Erklärung

Diese Dissertation wurde in Sinne von § 13 Abs. 4 der Promotionsordnung vom 29. Januar 1998 von Herrn Prof. Dr. Achim Hartschuh betreut.

Ehrenwörtliche Versicherung

Diese Dissertation wurde selbstständig, ohne unerlaubte Hilfe erarbeitet.

München, am 08.07.2008

(Unterschrift des Autors)

Dissertation eingereicht am 08.07.2008

1. Gutachter: Prof. Dr. Achim Hartschuh
2. Gutachter: Prof. Dr. Christoph Bräuchle

Mündliche Prüfung am 19.09.2008

This thesis is dedicated to my parents:

*Yongqin Qian
and
Linzhen Gu*

Acknowledgement

This thesis covers my three and half years of Ph.D work, contains both theoretical understanding and experimental finding focusing on my research field. Besides, those unselfish help and supports are absolutely necessary in the whole work that will be presented. At the first position, I would like to acknowledge the following people, without whom I could not proceed my work successfully.

I thank **Prof. Dr. Achim Hartschuh** for almost five years continual support and encouragement. I thank him for guiding me in the field of both near-field optical microscopy and single-wall carbon nanotubes, giving me many opportunities to present the work, and helping me for the movement to München.

I thank **Prof. Dr. Alfred J. Meixner** for many good suggestions, support and encouragement during the first one year and three months of my Ph.D in university of Tübingen. I thank him for leading me into the microscopy world at the very beginning.

I thank **Prof. Dr. Ado Jorio** for the discussion on the Raman properties of carbon nanotubes and part of the near-field results presented in this work. I also thank him for the support during my stay in his group in Brazil and our successful collaboration.

I would like to thank **Carsten Georgi** for the experimental support including the fabrication of high quality gold tips and contribution to some data analysis on peak fitting. I would also like to thank **Paulo T. Araújo** (UFMG, Brazil) for some near-field photoluminescence measurements and valuable discussions regarding the obtained results and carbon nanotubes.

The DNA-wrapped CoMoCAT nanotube samples in my major publications are provided by **Alexander A. Green** and **Prof. Mark C. Hersam** (Northwestern University), therefore I would like to thank them for the great samples. For the preparation of the DNA-wrapped

HiPCO nanotubes samples and the histogram of emission energies in Figure 42(a,b) I would like to thank **Tobias Gokus**. For the sample deposition on substrates I would like to thank **Nicolai Hartmann**.

I would like to thank my former colleagues **Antonio Virgilio Failla**, **Mathias Steiner**, **Rafal Korlacki** and **Hui Qian** in university of Tübingen for great discussions on different fields and collaborated publications that helped me build the sense of science. I would also like to thank **Cinzia Casiraghi** (Freie Universität Berlin) for spending time in our lab performing Rayleigh scattering and Raman measurements on graphene and the very useful discussion on the results.

I thank **Andreas Keilbach** for spending his time reading my thesis draft, taking care of me and encouraging me in my life. I couldn't go through many difficulties without his great support.

In addition, I would like to thank **Elke Nadler** (Uni Tübingen) and **Steffen Schmidt** (LMU) for the SEM measurements on all gold tips, providing easy selection of good tips throughout my work.

I gratefully acknowledge the financial support provided by the Deutsche Forschungsgemeinschaft (DFG-HA4405/3-1 and the Nanosystems Initiative Munich (NIM)) and the Deutscher Akademischer Austausch Dienst (DAAD Probral).

At the end, I would like to thank my parents for the endless love and the encouragement on both of my life and studies abroad.

Abstract

High resolution optical methods overcome the diffraction limit, a step essential for understanding the physical and chemical properties of nanostructures. In this work, I applied tip-enhanced near-field optical microscopy (TENOM) to study the optical properties of single-wall carbon nanotubes (SWNTs) with nanoscale spatial resolution. Simultaneously obtained near-field Raman scattering and photoluminescence (PL) data is shown to provide information with unprecedented detail on the nanotube structure and the resulting phonon and exciton properties. Near-field PL is found to be more localized along single nanotubes than Raman scattering in most cases due to defects and environmental perturbations. By detecting near-field PL spectra, my work has shown exciton energy variations along the same nanotubes induced by the environment. The local PL energy response to DNA-wrapping reveals large DNA-induced redshifts of the exciton energy that are two times higher than indicated by spatially averaging confocal microscopy. Exciton energy transfer between two semiconducting nanotubes is observed for the first time limited to small distances because of competing fast non-radiative relaxation. The transfer mechanism is explained by Förster-type electromagnetic near-field coupling. In addition, towards the end of a nanotube, PL decay is observed on a length scale of 15-40 nm which is attributed to exciton propagation followed by additional non-radiative relaxation at the nanotube end. The different enhancement mechanisms of Raman scattering and PL lead to different enhancement factors of the two signals. The PL enhancement can be stronger than the Raman enhancement because of the very low initial quantum yield of nanotubes. The signal enhancement of Raman scattering and PL is also found to exhibit different tip-sample distance dependencies because of the PL quenching effects from the gold tip. The results achieved in my thesis highlight the enormous capabilities of TENOM for the investigation of nanoscale surfaces.

Contents

1	Introduction	5
2	Introduction to single-wall carbon nanotubes	9
2.1	Formation of SWNTs and their structures	9
2.2	Electronic properties of SWNTs	14
2.3	Phonon structures of SWNTs	19
2.4	Raman scattering of SWNTs	20
2.5	Photoluminescence of SWNTs	24
2.6	DNA-wrapped SWNTs	27
3	Tip enhanced near-field optical microscopy	31
3.1	High-resolution microscopy	31
3.1.1	Angular spectrum representation	31
3.1.2	Resolution limits	33
3.1.3	Sub-wavelength Imaging Concepts	35
3.2	Field-enhancement at a metal tip	37
3.3	Signal enhancement for Raman scattering and photoluminescence	40
4	Experimental	43
4.1	Tip-enhanced near-field optical microscopy	43
4.2	Gold tip fabrication	47
4.3	SWNTs sample preparation	50

5	Near-field Raman and PL imaging and spectroscopy of SWNTs	53
5.1	Near-field Raman scattering in SWNTs	53
5.2	Near-field PL in SWNTs	56
5.2.1	PL imaging and spectroscopy	56
5.2.2	PL energy variation along the nanotubes	58
5.2.3	Highly localized PL in SWNTs	61
5.3	Simultaneous Raman scattering and PL of single SWNTs	64
5.4	Signal enhancement: Comparison for Raman scattering and PL	68
6	Local optical response of nanotubes to DNA-wrapping	77
7	Exciton transfer and propagation in SWNTs	87
7.1	Exciton energy transfer between two semiconducting nanotubes	87
7.2	Förster-type energy transfer modeling in 1D nanotubes	93
8	Exciton propagation towards the end of nanotubes	97
9	Conclusion and outlook	101
	Bibliography	103
	Appendices	125
A	Near-field measurement on graphite and graphene	125
B	Tip artifacts and near-field enhancement by a double tip	129
C	Abbreviations	133
D	Curriculum vitae	135

E Publications	137
F Conferences and workshops	139

List of Figures

1	Honeycomb lattice of graphene.	10
2	The unit cell of graphene.	11
3	Parallel equidistant cutting lines for nanotubes.	13
4	Energy dispersion and DOS of graphene.	15
5	Energy dispersion and DOS of (4,2) nanotube.	16
6	Kataura plot.	17
7	Polarization dependent optical transitions in nanotubes.	18
8	Phonon dispersion and phonon density of graphene and (10,10) nanotube.	19
9	Different Raman processes of nanotubes.	21
10	Typical Raman spectrum of nanotubes	23
11	PL spectra of three semiconducting SWNTs with different chiralities.	25
12	Energy diagram of single-wall carbon nanotubes.	26
13	Simulation of DNA-wrapping around nanotubes.	28
14	Morphology of DNA-nanotube hybrid systems.	29
15	Illustration of the transition from B form DNA to Z form DNA.	30
16	Illustration for the angular spectrum representation.	32
17	Illustration of the resolution limit.	34
18	Two approaches in near-field optical microscopy.	37
19	Field induced surface charge density at the metal tip and a laser illuminated gold tip.	39
20	Signal enhancement in both Raman scattering and PL spectra.	41
21	Schematic of the experimental setup.	44
22	Shear-force feedback mechanism.	46

23	Frequency modulated mode signal.	47
24	Schematic of the mode converter.	48
25	Schematic of the etching procedure.	49
26	SEM images of gold tips.	50
27	Confocal images of DNA-wrapped HiPCO nanotubes on glass.	54
28	Simultaneous topography and near-field Raman scattering of nanotubes.	55
29	Simultaneous topography and near-field PL of nanotubes.	57
30	PL energy variations of SDS-encapsulated nanotubes on mica.	59
31	PL energy variations of DNA-wrapped CoMoCAT nanotubes on mica.	60
32	Different extension of PL along a single nanotube.	62
33	Localized photoluminescence along single nanotubes	63
34	Simultaneous near-field Raman, PL and topography of single nanotubes.	65
35	Simultaneous topography, near-field Raman G-band and D-band images.	66
36	Raman images and PL image obtained by integrating intensities at different spectral windows	67
37	Near-field Raman scattering and PL for signal enhancement comparison.	69
38	Field polarization components at the gold tip and optical transition energies for few nanotubes	71
39	Distance dependent near-field Raman scattering and PL signal of the same nanotube.	72
40	Distance dependent near-field PL measured with different gold tips and the calculated result using a 80 nm gold spherical particle.	73
41	2D map of distance dependent PL spectra.	74
42	Histogram of PL emission energies using confocal microscopy.	78
43	Simultaneously recorded topography and near-field PL image of a DNA-wrapped CoMoCAT (6,5) nanotube on mica.	80

44	PL intensities along the nanotube representing two distinct energetic levels. . . .	81
45	PL spectra taken during tip approach and retracting	82
46	Comparison of confocal and near-field spectra and schematic of the excited state of DNA-wrapped nanotubes.	84
47	Simultaneously recorded near-field PL and topography of nanotubes.	88
48	Energy transfer between two semiconducting nanotubes from a thin bundle. . . .	90
49	Energy transfer between two intersecting nanotubes.	91
50	Energy level scheme of resonant transfer and energy transfer efficiencies.	92
51	Förster-type energy transfer between two dipoles	94
52	Förster-type energy transfer modeling between 1D nanotubes	95
53	PL quenching towards the nanotube end I.	98
54	PL quenching towards the nanotube end II.	100
55	Confocal Raman images of graphite.	126
56	Near-field measurement on graphite and graphite wrinkle.	127
57	Confocal Rayleigh scattering image and Raman spectra of graphene layers. . . .	128
58	Near-field images scanned by a double tip.	130
59	Illustration of field enhancement at a double tip	131

1 Introduction

Optical spectroscopy uniquely provides noninvasive imaging and characterization of materials and has been widely applied in investigations of vibrational and electronic properties of nanostructures. The information that can be extracted ultimately depends on the sensitivity and the resolution of optical systems. Conventional optical techniques however are limited by diffraction that largely broaden the spatial dimensions of images from nanoscale samples. The general aim of near-field optical microscopy is to extend the spatial resolution beyond the diffraction limit [1,2]. Probes close to the sample that can carry evanescent waves to extend the spectrum of spatial frequencies probed are generally used in the near-field optical microscopy. The introduction of the aperture probe [3] has allowed optical imaging with sub-diffraction resolution and has stimulated interests in many disciplines, especially the material and biological sciences [4]. Alternatively, the use of laser-illuminated metal tips for near-field imaging has been suggested by Wessel [5] and discussed by many groups [6–12]. The strong electric fields confined to the vicinity of the metal tip increase both excitation and radiation rates providing high spatial resolution imaging as well as enormous signal enhancement. The versatility of the technique allows the study of a variety of spectroscopic signals of surfaces, such as Raman scattering and fluorescence on the nanoscale.

In my thesis, I applied TENOM to study the optical properties of single-wall carbon nanotubes (SWNTs). SWNTs were first discovered in 1993 by Iijima two years after he succeeded in the growth of multi-wall carbon needles [13, 14]. SWNTs are seamless cylinders consisting of a rolled-up graphene sheet, with 0.7 nanometers to several nanometers in diameter and up to tens of millimeters in length. Because of their unique quasi-one-dimensional structure, carbon nanotubes have been investigated as a model system in studies of fundamental physical phenomena. In addition, they have large potential for various applications in photonics, opto- and nano-electronics as well as biosensing [15–20].

Single nanotube spectroscopy is ideally suited for studying the optical properties of nanotubes and can be used to determine the diameter and chirality (n,m) . Raman scattering of SWNTs reveals the structure information of nanotube, and can be used to distinguish semiconducting and metallic nanotubes. PL of nanotubes has been reported for the first time for an ensemble of SWNTs encapsulated in micelles [21]. The PL of nanotubes results from exciton recombination that decays on picosecond time-scales [22–24] in the near-infrared spectral range [22, 25–28]. Observation of PL energies and dynamics from single nanotubes provides access to the properties

of excitonic states in SWNTs with specific chirality (n,m) . The energy and dynamical variations observed from nanotube-to-nanotube of the same chirality indicate local distortions arising from both defects and environmental perturbations [28–32]. It is generally expected that bundling leads to quenching of the PL of nanotubes with large bandgap caused by rapid energy transfer to small bandgap and metallic nanotubes. Surfactants such as sodium dodecyl sulfate (SDS), sodium cholate and DNA have facilitate sorting or isolating nanotubes into individual ones [18, 19, 33, 34] thus increasing the probability for observing single nanotubes.

TENOM provides high resolution imaging and spectroscopy combined with the topography of nanotubes permitting a direct correlation between the optical signal and the sample morphology on the nanometer scale. Probing the optical properties along individual nanotubes is essential for studying optical responses of nanotubes under local perturbations.

This thesis presents the first detailed view inside the optical properties of carbon nanotubes by measuring the near-field Raman scattering and PL signal on the nanometer scale. The local optical information at relevant length scales, such as the exciton diffusional range and the nanotube-nanotube coupling range, can be obtained. The thesis is arranged in the following way. Section two gives an overview of single-wall carbon nanotubes including structure, electronic properties and phonon properties. Raman scattering and photoluminescence as two distinct optical processes for nanotubes characterization are included. At the end of this section, DNA-wrapped nanotubes are introduced including the present understanding of the wrapping mechanism and wrapping effects.

Section three provides the theoretical explanation of physical principles underlying the diffraction limit using the angular spectrum representation and introduces several sub-wavelength imaging concepts. The field enhancement at the tip is described in detail in this section. Using this information, the experimental requirements and expected properties of the enhanced fields are discussed. In addition, a theoretical comparison of the signal enhancement of Raman scattering and PL is shown based on the different enhancement mechanisms.

Section four provides a detailed introduction of the tip-enhanced near-field microscope used in this work. The advantage of using frequency modulation as feedback mode to control the shear-force detection with small tip-surface distances will be explained in this section. The gold tip fabrication and sample preparations are described in this section.

Section five starts with high resolution near-field Raman scattering imaging by detecting the characteristic Raman, G-mode of carbon nanotubes. In the following, near-field PL imaging

is presented. PL is found to occur both extended and highly localized along the nanotubes. Near-field spectroscopy reveals PL energy variations along the single nanotubes on the length scale of 30 nm. The origin of both PL localization and PL energy variation are discussed and attributed to defects and local environment perturbations. Simultaneous near-field Raman and PL imaging are obtained from individual nanotubes, providing the correlation between phonon properties and electronic properties of nanotubes. Based on the simultaneous detection of Raman and PL signals on the same nanotubes, the enhancement of the two signals are compared. By decomposing the electric field at the tip into parallel and perpendicular polarization contributions from optical transitions with different orientations with respect to the nanotube axis are discussed. The PL enhancement can be stronger than the Raman enhancement because of the very low initial quantum yield of nanotubes.

Section six provides a detailed example of PL energy variations along a single nanotube due to DNA-wrapping. Two distinct emission bands are identified and assigned to emission from DNA-wrapped segments unwrapped segments. The PL energy shift along nanotubes induced by DNA segments turns out to be a factor of two higher than the value determined from confocal measurements representing spatial averaging. The transition between two energetic levels are estimated to be smaller than the spatial resolution of 15 nm in the current measurement.

Section seven presents the observation of energy transfer between two semiconducting nanotubes and based on the data the efficiency, the range and the time-constant of energy transfer have been estimated. The range of efficient transfer is found to be limited to a few nanometers because of competing fast non-radiative relaxation responsible for low photoluminescence quantum yield. Using Förster-type energy transfer modeling in 1D nanotubes, the energy transfer is explained by Förster-type electromagnetic near-field coupling. Finally, section eight presents experimental results that towards the end of nanotubes, PL decay is observed on a length scale of 15-40 nm which is attributed to exciton propagation followed by additional non-radiative relaxation at the nanotube end. The long decay length also reflect the effects of excitons mobility.

My thesis presents several new results on the PL properties of nanotubes taking advantage of the high resolution TENOM technique, including the PL variation on the nanometer scale, local optical response of nanotubes to DNA-wrapping, exciton energy transfer between two individual semiconducting nanotubes and the direct observation of PL decay at the nanotube end. TENOM is proven to be a powerful tool for investigations on individual nanotubes with a nanometer scale resolution, providing novel information on carbon nanotube photophysics.

2 Introduction to single-wall carbon nanotubes

2.1 Formation of SWNTs and their structures

Single-wall carbon nanotubes (SWNTs) can be described as seamless cylinders with different helicities rolled from a graphene sheet. The structure of a nanotube is determined by the chiral vector C_h along which a graphene sheet is rolled up, as shown by the large blue arrow in Figure 1, and formulated as [35,36]

$$C_h = n\hat{a}_1 + m\hat{a}_2 \quad (1)$$

with \hat{a}_1 and \hat{a}_2 being the vectors of the hexagonal unit cell of graphene. n and m are two indices uniquely describing the structure of nanotubes. The chiral vector around the nanotube circumference connects two crystallographically equivalent sites on the graphene sheet (A and B in Figure 1). A nanotube is formed by rolling along the chiral vector C_h to make A meet B and A' meet B'. The chiral angle θ is defined as the angle between the zigzag axis (red dashed arrow marked with zigzag) or \hat{a}_1 and the chiral vector. There are three types of SWNTs according to different tuple (n,m) : Zigzag nanotubes correspond to $(0, m)$ or $(n, 0)$ and have the chiral angle $\theta=0^\circ$, armchair nanotubes correspond to $n=m$ and have the chiral angle $\theta=30^\circ$. Chiral angle $0^\circ < \theta < 30^\circ$ defines so-called chiral nanotubes. The two ends can be capped with half of a fullerene molecule, which is cut in the equatorial plane corresponding to the fivefold axis for armchair tubes, while threefold axis for zigzag tubes [37]. According to tight binding calculations nanotubes with $(2n + m) \bmod 3 = 0$ (n divisible by m) are metallic, nanotubes with $(2n + m) \bmod 3 = 1$ or 2 are semiconducting nanotube S1 or S2, respectively [38]. In Figure 1, the yellow dots denote the metallic nanotubes, the blue dots denote S1 nanotubes while the green dots denote S2 nanotubes. The diameter d_t of the SWNTs and the chiral angle θ are the main parameters that will give rise to differences in the properties of the various carbon nanotubes. The nanotube diameter can be written as [35,36]

$$d_t = \sqrt{3}a_0 \frac{\sqrt{n^2 + nm + m^2}}{\pi} \quad (2)$$

a_0 is the length a of carbon-carbon bond in graphene being 1.421 Å. The chiral angle θ is given by [35,36]

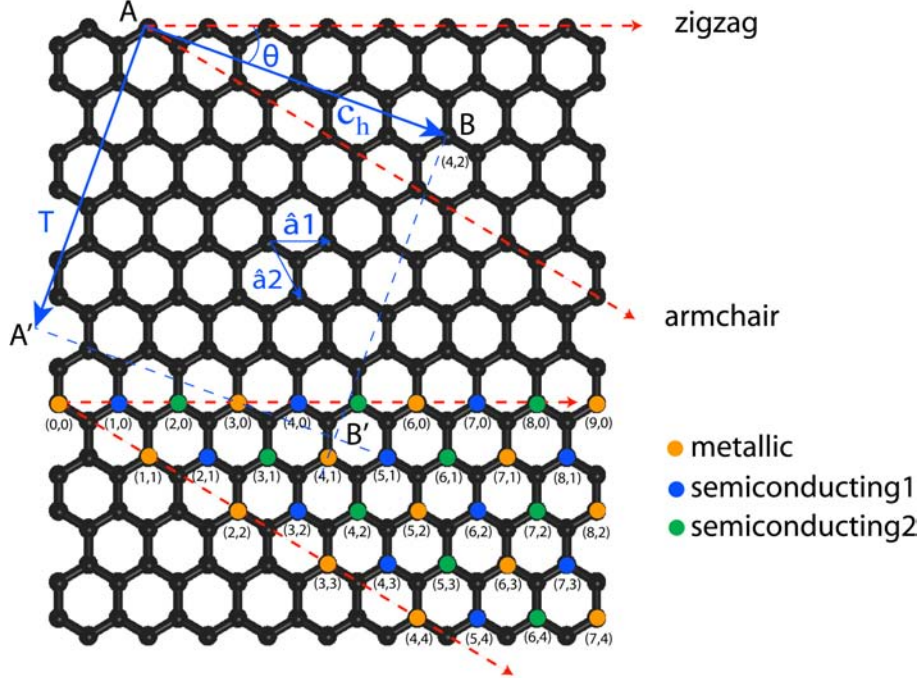


Figure 1: Honeycomb lattice of graphene with unit vector \hat{a}_1 and \hat{a}_2 . Rolling up the sheet along chiral vector C_h forms a single-wall carbon nanotube, with structure described by tuple (n,m) as for $(4,2)$ nanotube in the figure. T is the translational vector of nanotube. The rectangle $ABB'A'$ defines the unit cell of the nanotube. Nanotubes are classified into chiral and achiral nanotubes, or metallic and semiconducting nanotubes as denoted by dots. See details in the main text.

$$\theta = \tan^{-1} \frac{\sqrt{3}m}{m + 2n} \quad (3)$$

As we see, both d_t and θ can be defined in terms of the integers (n,m) which can therefore be used to specify the nanotube structure. The rectangle $ABB'A'$ is defined as the unit cell of the nanotube.

To understand the unusual structure of carbon nanotubes, we start with understanding of the unit cell in real space and the corresponding first Brillouin zone in reciprocal space for two-dimensional graphene, as shown in Figure 2. Figure 2(a) shows the unit cell of graphene in real

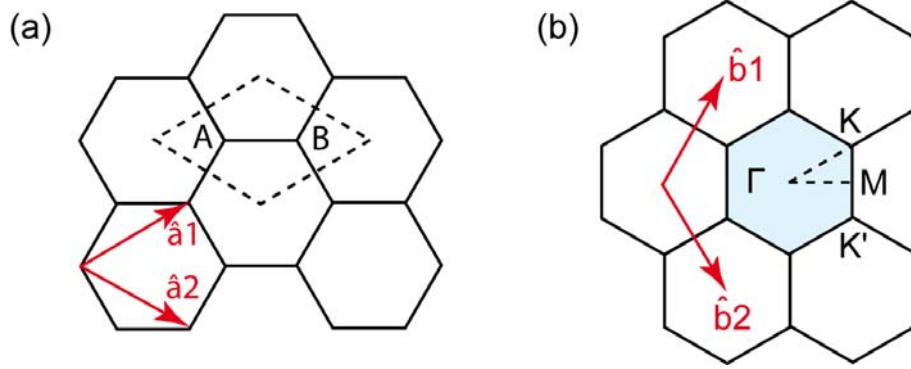


Figure 2: The unit cell of graphene in real space (rhombus in a) containing two equivalent carbon atoms A and B and the corresponding first Brillouin zone in reciprocal space for two-dimensional graphene (b). The vectors \hat{a}_1 and \hat{a}_2 , \hat{b}_1 and \hat{b}_2 represent lattice vectors in real space and in reciprocal space, respectively.

space marked with the dashed rhombus, consisting of two equivalent carbon atoms A and B. \hat{a}_1 and \hat{a}_2 are basis vectors in real space, expressed as [35, 36]

$$\hat{a}_1 = \left(\frac{\sqrt{3}}{2}a, \frac{1}{2}a\right), \quad \hat{a}_2 = \left(\frac{\sqrt{3}}{2}a, -\frac{1}{2}a\right) \quad (4)$$

where $a = \sqrt{3}a_0 = 2.46 \text{ \AA}$ is the lattice constant of graphene. Figure 2(b) shows first Brillouin zone in reciprocal space for two-dimensional graphene by the blue filled hexagon. Similarly, the basis vector in reciprocal lattice \hat{b}_1 and \hat{b}_2 are expressed as [35, 36]

$$\hat{b}_1 = \left(\frac{2\pi}{\sqrt{3}a}, \frac{2\pi}{a}\right), \quad \hat{b}_2 = \left(\frac{2\pi}{\sqrt{3}a}, -\frac{2\pi}{a}\right) \quad (5)$$

corresponding to the graphene lattice constant of $4\pi/\sqrt{3}a$ in reciprocal space. There are three high symmetric points Γ , K and M in the Brillouin zone. It is also pointed out here that there are two equivalent K points in the hexagonal Brillouin zone denoted by K and K' .

In Figure 1, the rectangle $ABB'A'$ defines the unit cell for SWNTs, delineated by the perpendicular two vectors C_h and T . Vector T runs along the nanotube axis with the length of the shortest distance between equivalent carbon atoms and is known as translational vector expressed as [35, 36]

$$T = t_1 \hat{a}_1 + t_2 \hat{a}_2, \quad (6)$$

where the coefficients t_1 and t_2 are related to (n, m) by [35,36]

$$t_1 = \frac{2m + n}{D}, \quad t_2 = -\frac{2n + m}{D}, \quad (7)$$

D is the greatest common divisor of $(2n + m, 2m + n)$ and is given by [35,36]

$$D = \begin{cases} d, & \text{if } n - m \neq 3d, \\ 3d, & \text{if } n - m = 3d. \end{cases} \quad (8)$$

d is the greatest common divisor of the chiral indices (n, m) . The length of T is calculated by [35,36]

$$|T| = \frac{\sqrt{3}}{D} |C_h|. \quad (9)$$

With these parameters, one can have a intuitive picture of a unit cell of a nanotube with diameter d_t and nanotube length $|T|$. Both vectors C_h and T connect two equivalent carbon atoms, therefore the unit cell of nanotube has an integer number of hexagons and can be calculated by dividing the nanotube surface area by the area of the hexagonal unit cell of graphene. This leads to

$$N = \frac{2(n^2 + m^2 + nm)}{D}. \quad (10)$$

We can derive the number of carbon atoms in one unit cell of nanotube since each hexagon contains only two carbon atoms as

$$N_c = 2N = \frac{4(n^2 + m^2 + nm)}{D}. \quad (11)$$

Since the unit cell of nanotubes in real space is much larger than that of a 2D graphene sheet, the first Brillouin zone in reciprocal space is smaller than that of graphene. Brillouin zone-folding

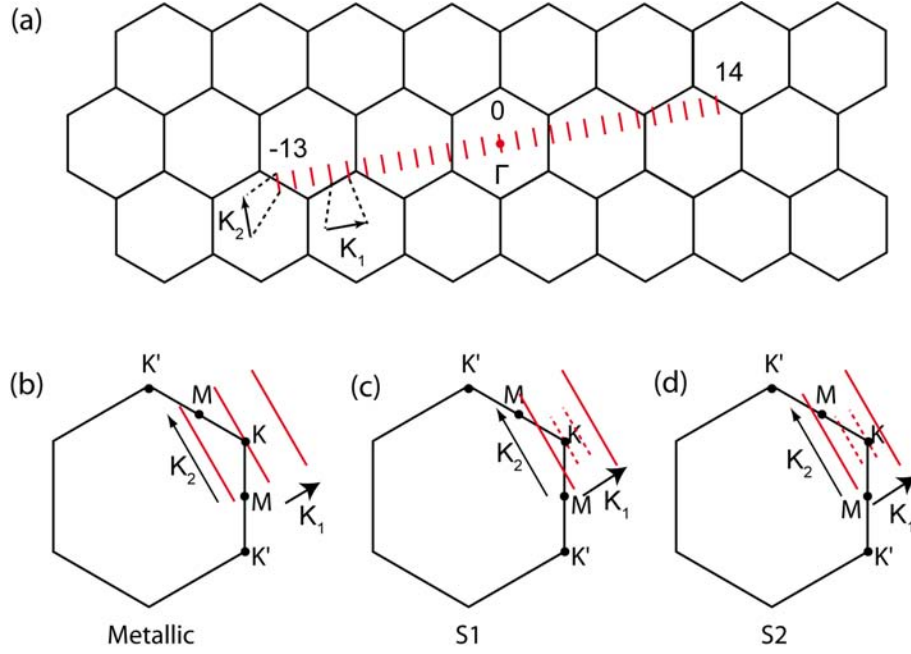


Figure 3: (a) Parallel equidistant cutting lines (red lines) with index μ from -13 to 14 for (4,2) nanotube. In the direction of K_1 , discrete k values are obtained by periodic boundary conditions for the circumferential direction of the carbon nanotubes, while in the direction of the K_2 vector, continuous k vectors are shown in the one-dimensional Brillouin zone. For metallic nanotubes (b), the red line passes a K point (corner of the hexagon). For the semiconductor nanotubes (c) and (d), the K point is always one-third of the distance between two red lines representing S1 and S2, respectively.

has been commonly used to obtain the approximate electron and phonon dispersion relations for carbon nanotubes with specific (n, m) geometrical structures [39].

The two vectors in reciprocal space corresponding to C_h and T in real space are K_1 and K_2 , as indicated in Figure 3. K_1 and K_2 represent a discrete unit wave vector along the circumferential direction, and a continuous vector along the nanotube axis direction, respectively. For a (n, m) nanotube K_1 and K_2 are given by [39]

$$K_1 = \frac{(2n + m)\hat{b}_1 + (2m + n)\hat{b}_2}{N \cdot D}, \quad K_2 = \frac{m\hat{b}_1 - n\hat{b}_2}{N}. \quad (12)$$

In Figure 3(a) parallel equidistant cutting lines with the index μ from -13 to 14 (from $1-N/2$ to

$N/2$) for a (4,2) nanotube are shown. The separation between two adjacent lines and the length of the cutting lines are given by the absolute value of K_1 and K_2 vectors being

$$|K_1| = \frac{2}{d_t}, \quad |K_2| = \frac{2\pi}{|T|} = \frac{2D}{\sqrt{3}d_t}. \quad (13)$$

For each discrete value μ of the circumferential wave vectors, a 1D electronic energy band appears (one π -band and one π^* -band, section 2.2), whereas each μ gives rise to 6 branches in the phonon dispersion relations (section 2.3). In Figure 3(b-d) several cutting lines near the K point are shown. For a particular (n,m) nanotube, if the cutting line goes through the K point of the 2D Brillouin zone (Figure 3(b)), where the π -band and π^* -band are degenerated therefore no band gap at this point, the nanotube is defined as metallic. When the K point is located between two cutting lines, which is always located at a position one-third of the distance between two adjacent K_1 lines (Figure 3(c)) [40], the nanotube is defined as a semiconducting nanotube with a finite energy gap. Depending on the position of the K point, Figure 3(c) and (d) represents semiconducting nanotube S1 and S2, respectively (section 2.2).

2.2 Electronic properties of SWNTs

We first describe the electronic states in carbon nanotubes focusing on the electronic density of states in a zone-folding approximation. The starting point of this analysis is the tight-binding expression for the π orbitals of a graphene sheet, which is then modified to account for the confinement around the nanotubes circumference [41, 42]. Theoretical calculations [43–45] reveal that the electronic structure of nanotubes is determined completely by their geometric structure.

The physics behind can be understood with the help of a band-folding picture [45]. A graphene sheet has a unique band structure which has states crossing the Fermi level at two K points. Figure 4(a) shows electronic dispersion for the occupied π band and unoccupied π^* bands of 2D graphene in the first Brillouin zone [38]. The inset shows the energy dispersion along the high symmetry lines between the Γ , M , and K points. The valence π band (lower part) and the conduction π^* band (upper part) are degenerate at the K points in the hexagonal Brillouin zone what corresponds to the Fermi energy at the Fermi wavevector. Graphene is a zero-gap. The linear dispersion of these two bands around the K point of graphene is also shown in Figure 4(b) by a tight-binding calculation [46].

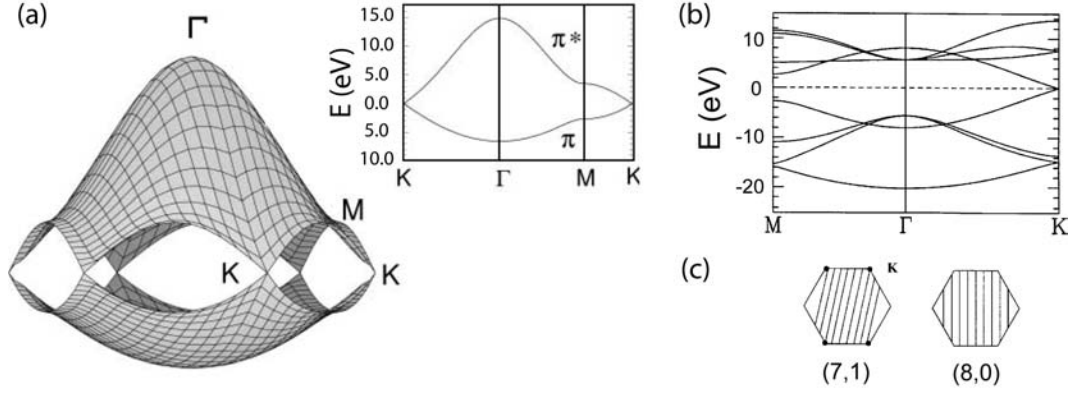


Figure 4: (a) the energy dispersion relations for 2D graphene in the Brillouin zone. The inset shows the energy dispersion along the high symmetry lines between the Γ , M , and K points. The valence π band (lower part) and the conduction π^* band (upper part) are degenerated at the K points in the hexagonal Brillouin zone which corresponds to the Fermi energy. (b) linear dispersion of valence band and conduction band of graphene by tight-binding calculation. (c) allowed k-vectors of the (7,1) and (8,0) tubes mapped onto the graphite Brillouin zone.

When forming a tube by rolling up the graphene sheet, owing to the periodic boundary conditions imposed in the circumferential direction, only a certain set of k states of the planar graphene sheet is allowed. The allowed states, e.g. indicated by the cutting lines in Figure 4(c) for (7,1) nanotube and (8,0) nanotube, respectively, depend on the diameter and chirality of the nanotube. The relative position of the K point to the cutting line determines the metallicity of the nanotubes. Importantly, the states close the Fermi energy in both the metallic and the semiconducting tubes are all from states near the K point, and hence their transport and other properties are related to the properties of the states on the cutting lines. For example, the conduction band and valence bands of a semiconducting tube originate from states along the line closest to the K point. However, because of the high curvature of nanotubes with small radius, strong rehybridization between the σ and π states can modify the electronic structure.

The cutting lines of allowed wave vectors in reciprocal space of (4,2) nanotubes can be represented in the Brillouin zone of 2D graphene sheet as indicated by the thick solid lines in Figure 5(a). The electronic dispersion of nanotubes can be derived in the same way as for graphene (Figure 4) and by superimposing the cutting lines into the 2D electronic energy surface as shown in Figure 5(b). As the cutting lines of (4,2) nanotube do not pass through the K point, a band-gap in the electronic band structure is resulting (b). The bands below the Fermi

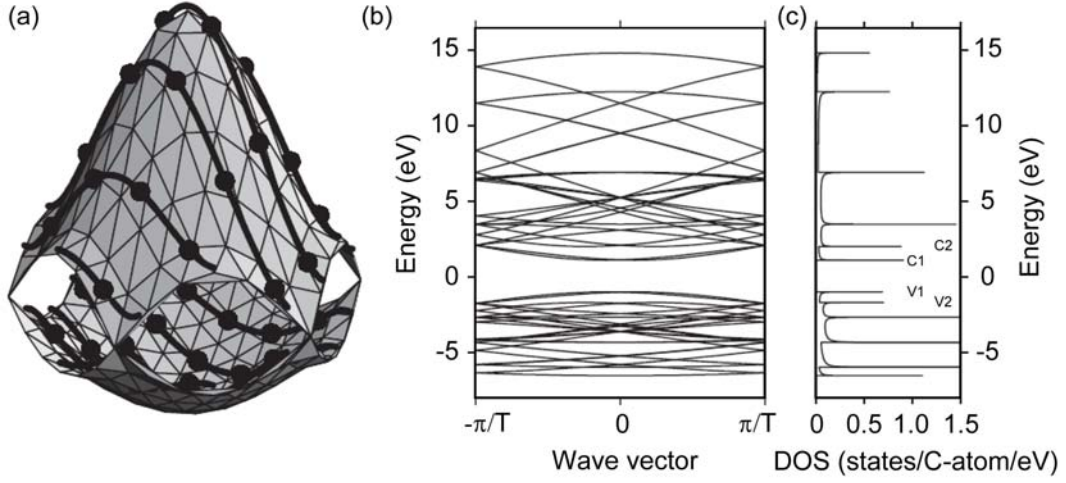


Figure 5: (a) the energy dispersion relations for 2D graphene in the Brillouin zone, with cutting line of (4,2) nanotube as indicated by thick solid lines. (b) Electronic energy band diagram for the (4, 2) nanotube obtained by zone-folding from (a). (c) Density of electronic states for the band diagram shown in (b). v1,c1,v2 and c2 denote the lowest two valence bands and conduction bands.

level are valence bands and bands higher than the Fermi level are conduction bands. Figure 5(b) can be simplified by considering the 1D density of states (DOS) predicting van Hove singularities for maximum and minimum (vHSs). Optical transitions occur between the valence bands and conduction bands, whose energies are defined as E_{ii} , with i denoting the order of the valence and conduction energy bands. The closest band to the Fermi level originates from the cutting line closest to the K point in the 2D Brillouin zone.

Since vHSs in the DOS profile arise from different cutting lines with lines separation determined by nanotube diameters as defined in equation 13, the energy differences between vHSs are thus inversely diameter dependence, which can be expressed by [39]

$$E_{ii}^M = \frac{6a_0\gamma_0}{d_t}, \quad E_{ii}^S = \frac{2a_0\gamma_0}{d_t}, \quad (14)$$

with γ_0 being the transfer integral. M and S denote the metallic and semiconducting nanotubes, respectively. What's more, the direction of cutting lines follow the chiral vector with a chiral angle θ leading to a θ dependence of vHSs separation. The two factors lead to a (n,m) dependence of transition energies between vHSs. Therefore, every nanotube has its unique transition energy.

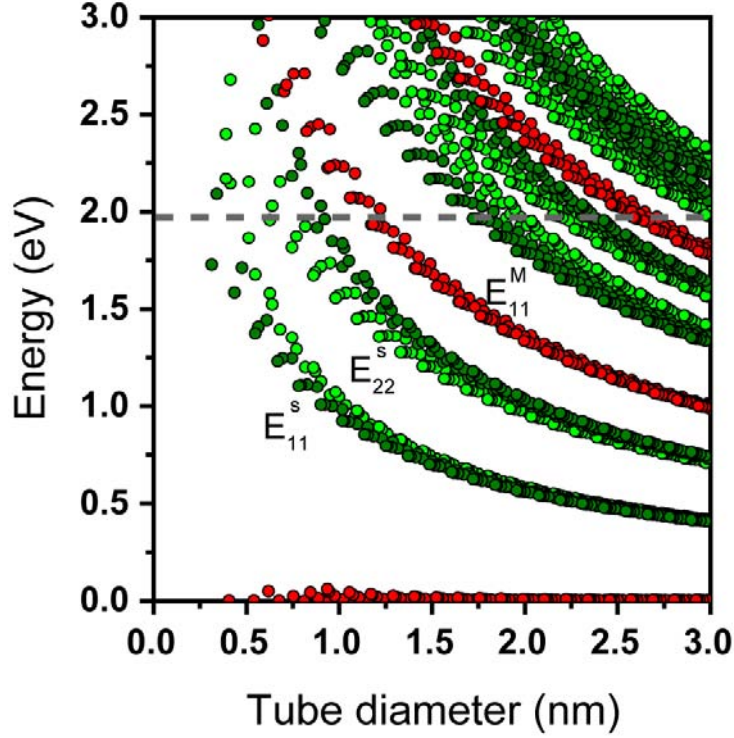


Figure 6: Kataura plot showing the variation in optical transition energy (E_{ii}) as a function of SWNT diameter d_t . Red dots, light green dots and dark green dots denote the metallic nanotubes, S1 semiconducting nanotubes and S2 semiconducting nanotubes.

Figure 6 is known as Kataura plot [47]. It shows the electronic transition energies E_{ii} vs. nanotube diameter d_t for SWNTs calculated by the overall function including the diameter dependence, the chiral angle dependence and the many-body corrections as shown

$$E_{ii}(p, d_t) = a \frac{p}{d_t} \left[1 + b \log \frac{c}{p/d_t} \right] + \beta_p \cos 3\theta / d_t^2 \quad (15)$$

with $a = (1.074 \pm 0.002)$ eV.nm, $b = (0.467 \pm 0.004)$ and $c = 0.812 \text{ nm}^{-1}$ [48]. The integer p ($= 1, 2, 3, 4, \dots$) is for E_{11}^S , E_{22}^S , E_{11}^M , E_{33}^S and so on. The experimental values for β_p at the lower (higher) branches for $E_{ii}^{S,M}$ are: $-0.07(0.09)$, $-0.18(0.14)$, $-0.18(0.29)$, $-0.33(0.49)$, $-0.43(0.59)$, $-0.60(0.57)$, $-0.60(0.73)$ and $-0.65(-)$ for p from 1 to 8. A correction factor $\gamma p/d_t$ with $\gamma = (0.0596 \pm 0.0005)$ nm.eV is added for higher transitions (from E_{33}^S to higher E_{ii}^S , from E_{22}^M to higher E_{ii}^M). Each dot in the plot represents a nanotube with specific (n,m). Red dots, light

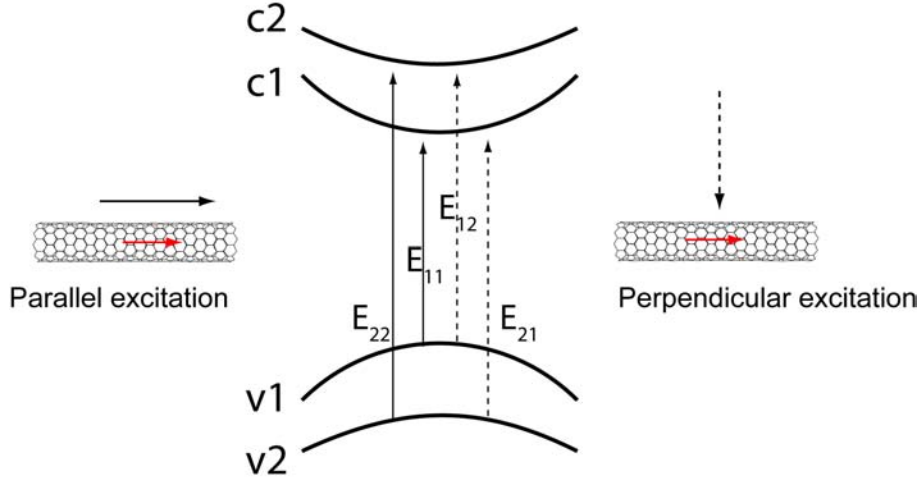


Figure 7: Schematics of optical transitions in nanotubes corresponding to parallel (black solid) and perpendicular (black dashed) absorptions indicated by the arrows for external electric field (black) and transition dipoles in the nanotube (red).

green dots and dark green dots denote the metallic nanotubes, S1 semiconducting nanotubes and S2 semiconducting nanotubes, respectively.

Over the past years, the polarization dependent optical transitions of SWNTs have been investigated and it has been demonstrated that the optical signals are strongest when the polarization of the incident radiation is parallel to the nanotube axis and vanishes when perpendicular due to the suppressed absorption [10, 28, 49–52]. Under perpendicular polarized field, the induced charges on the surface of the nanotube produce a depolarizing field inside the nanotube that can cancel the external field which is known as depolarization effect [49, 50]. From the selection rule, in the case of parallel polarization excitation, only the optical transitions between subbands with the same quasi-angular momentum are allowed ($\Delta\mu=0$ or E_{ii} transitions), while perpendicular polarization excitation allows $\Delta\mu=\pm 1$ transitions (μ is the index of cutting lines, see in Figure 3), e.g. E_{12} denotes the transition between the first valence band to the second conduction band as illustrated in Figure 7. Recently, transitions E_{12} using perpendicular excitation have been detected both in polarized photoluminescence excitation (PLE) experiment [53] and in the absorption spectrum [54], although the perpendicular transition is expected to be strongly suppressed by the depolarization effect [10, 28, 49–52].

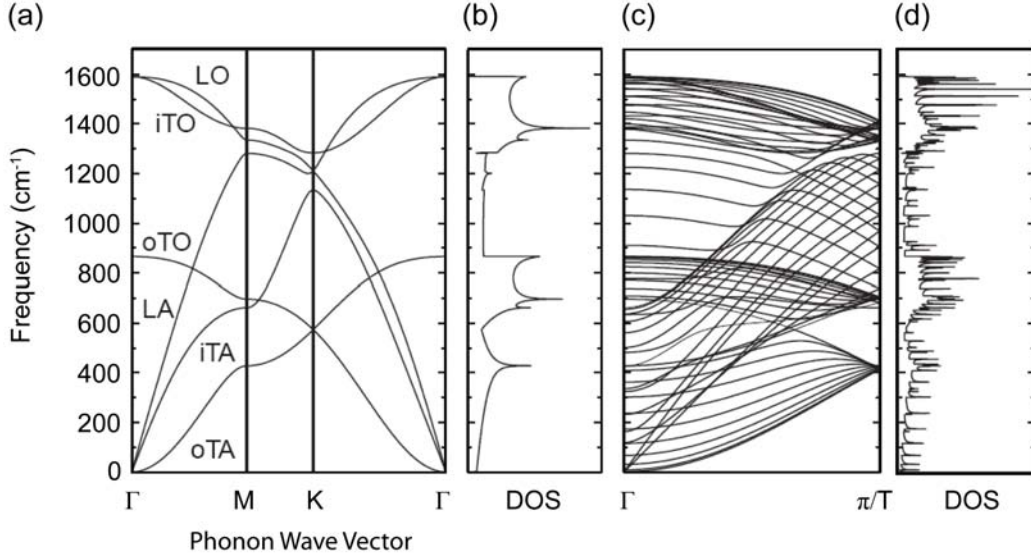


Figure 8: (a) the phonon dispersion of graphene using the force constants from [57], with the six phonon branches labelled: out-of-plane transverse acoustic (oTA), in-plane transverse acoustic (iTA), longitudinal acoustic (LA), out-of-plane transverse optic (oTO), in-plane transverse optic (iTO) and longitudinal optics (LO) respectively. (b) the phonon density of states of graphene. (c) the calculated phonon dispersion relations of (10,10) nanotube and (d) the corresponding phonon density of states.

2.3 Phonon structures of SWNTs

The phonon modes of carbon nanotubes can be calculated in a way similar to what has been used to obtain the electronic dispersion by applying the zone-folding scheme to the 2D phonon dispersion relation of the graphene sheet [38]. The phonon dispersion relations of the graphene can be calculated by a force constant model [38], by tight-binding [55] or *ab initio* [56] methods.

The 2D graphene sheet with two atoms A and B in the unit cell of graphene (Figure 2) give rise to six phonon modes because of the three degrees of freedom per atom. Figure 8(a) shows the phonon dispersion of graphene, with the six phonon branches labeled: out-of-plane transverse acoustic (oTA), in-plane transverse acoustic (iTA), longitudinal acoustic (LA), out-of-plane transverse optic (oTO), in-plane transverse optic (iTO) and longitudinal optic (LO) respectively [36]. The zone-folding scheme neglects the curvature of a nanotube wall [58]. The in-plane and out-of-plane phonon modes of graphene are coupled because of the curvature especially in the low frequency acoustic phonon modes. One in-plane acoustic mode results in the acous-

tic phonon mode of the nanotube corresponding to the vibrational motion along the nanotube axis. The out-of-plane acoustic phonon mode give rise to the radial breathing mode (RBM, the vibrational motion in the radial direction of the nanotube). The phonon density of states of graphene is shown in Figure 8(b). Using this zone-folding scheme, the phonon dispersion of (10,10) nanotube is obtained in Figure 8(c) and its phonon DOS in Figure 8(d). Among the large amount of phonon modes, only 15 or 16 are Raman-active and only 7, 8 or 9 are infrared-active as predict by group theory [59].

Phonon-assisted absorbance features observed in photoluminescence excitation spectra [60, 61], and phonon sidebands observed in photoconductivity spectra [62] demonstrate the importance of the involvement of phonons for optical processes in nanotubes resulting from electron-phonon coupling. The electron-phonon coupling leads to a high intensity of phonon-assisted optical transitions and a large broadening of excited electronic states induced by inelastic electron-phonon scattering. The electron-phonon interactions provide an efficient mechanism for non-radiative relaxation to the ground electronic state, which would explain very low efficiencies of nanotube emission typically observed in ensemble studies [61]. Details will be discussed in section 2.5.

2.4 Raman scattering of SWNTs

Raman spectra provide deep insight into the physical properties as well as the material quality. In the Raman spectra of SWNTs, there are many features that can be identified with specific phonon modes and with specific Raman scattering processes that contribute to each Raman feature. Raman scattering can be classified as one-phonon, two-phonon and multi-phonon scattering, depending on the number of emitted phonons. The order of a Raman scattering process is defined as the number of scattering sequences, including elastic scattering by an imperfection (such as a defect or edge) of the crystal.

Figure 9 shows different Raman processes [36]. In all processes, the electron first absorbs a photon at k state, then another phonon with wave vector q is emitted for one-phonon Raman scattering (Figure 9(a,b,c,e,f,g)) or two phonons with wave vector q and $-q$ emitted for two-phonon Raman scattering (Figure 9(d,h)). The electron is scattered back to the original k position and recombines with the hole. In first order Raman scattering, the electron recombines with the hole at the original state (Figure 9(a,e)). While in second order Raman scattering, the electron is scattered by a phonon with a wave vector q to the $k + q$ state and scattered

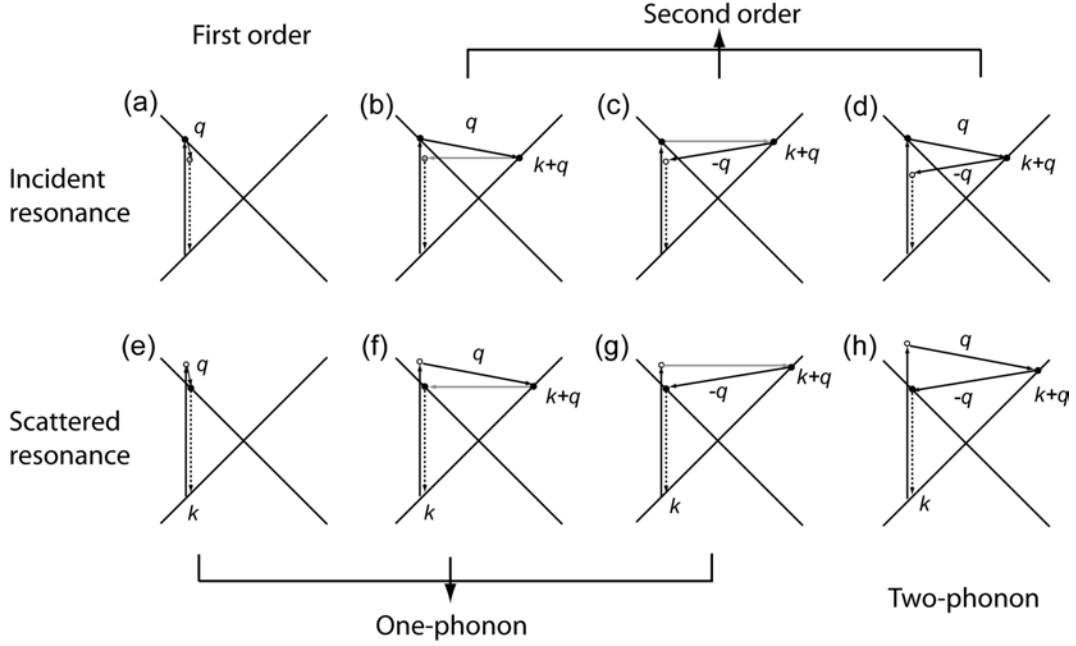


Figure 9: Different Raman processes of nanotubes, first order (a,e) and second order (b,c,d,f,g,h) Raman scattering, one-phonon (a,b,c,e,f,g) and two-phonon (d,h) Raman scattering, incident phonon resonance Raman (a,b,c,d) and scattered phonon resonance Raman (e,f,g,h). Resonance points are shown as solid circles.

back to the original k state elastically (one-phonon process, Figure 9(b,c,f,g)) or by a phonon with wave vector $-q$ (two-phonon process, Figure 9(d,h)). There are two resonance conditions for optical transitions in carbon nanotubes: resonance with the incident laser photon (incidence resonance, Figure 9(a,b,c,d)) and resonance with the scattered photon (scattered resonance, Figure 9(e,f,g,h)). When the laser energy has the same energy as vHSs energies in the DOS of nanotubes with specific (n,m) , the Raman intensity is resonantly enhanced. Resonant Raman scattering of nanotubes gives the possibility to detect individual nanotubes. The laser used in this work is a HeNe laser at 632.8 nm corresponding to 1.96 eV as marked with a gray dashed line in Figure 6 covering a number of nanotubes in resonance with laser energy.

There are several bands in a typical Raman spectrum as shown in Figure 10, the radial breathing mode (RBM), the disorder-induced D-band, its corresponding second-order G'-band and the tangential G-band modes. Single nanotube spectroscopy has revealed that each band reflects many physical phenomena concerning their dependence on diameter and chirality. The RBM scattering is governed by a first order Raman process with the frequency proportional to $1/d_t$,

$$\nu_{RBM} = \frac{C1}{d_t} + C2 \quad (16)$$

where both C1 and C2 are constants. The absolute values for C1 and C2 vary in literature. Bachilo *et al.* [27] estimated C1=223.5 and C2=12.5, Jorio *et al.* [63] fixed C1=248 and C2=0 by using optical measurements from a number of individual nanotubes on SiO_2 substrate. Several different formula have been proposed for describing the relation between RBM frequency and tube diameter as well as corrections from the effect of the substrate and from tubetube interactions. Resonant RBM Raman scattering is a powerful tool for (n,m) assignment of nanotubes using the theory of resonant transition [63,64].

The G-band in graphene originate from the tangential stretching phonon mode between two dissimilar carbon atoms (A and B in the unit cell of graphene, Figure 2(a)) appearing as a single Lorentzian peak at 1582 cm^{-1} . The band shape of the G-band in nanotubes however is more complicated because of the folding of the graphite Brillouin zone into the SWNT zone, and due to the symmetry-breaking effects associated with the nanotube curvature. The G mode of graphite splits into several modes with different symmetries in the Raman spectra of nanotubes [65,66]. The tangential G mode is also governed by the first order Raman processes. The G-band in Raman spectra can be used for nanotube characterization such as metallic or semiconducting nanotubes assignment, and for probing the charge transfer arising from doped nanotubes [65].

G-bands of semiconducting nanotubes and metallic nanotubes exhibit distinct differences in band shape. Semiconducting nanotubes have G_-^S (lower frequency peak) and G_+^S (higher frequency peak) bands originating from the vibrations of carbon atoms along the circumferential direction (TO mode) and vibrations along the nanotube axis (LO mode), respectively. Therefore the G_-^S band is strongly diameter dependent. The Raman spectrum of metallic nanotubes exhibits two peaks abbreviated as G_-^M and G_+^M for lower and higher frequency modes, respectively. G_-^M has a single Lorentzian band shape, while G_+^M has an asymmetric band shape described as Breit-Wigner-Fano peak (BWF) in the early model, with the line shape function [67]:

$$I(\omega) = I_0 \frac{[1 + (\omega - \omega_{BWF}/q\Gamma)]^2}{1 + [(\omega - \omega_{BWF}/\Gamma)]^2} \quad (17)$$

The BWF line shape indicates the coupling with a plasmon-based electronic continuum spectra. In this BWF function, $1/q$ is a measure for the interaction of the phonon with a continuum of

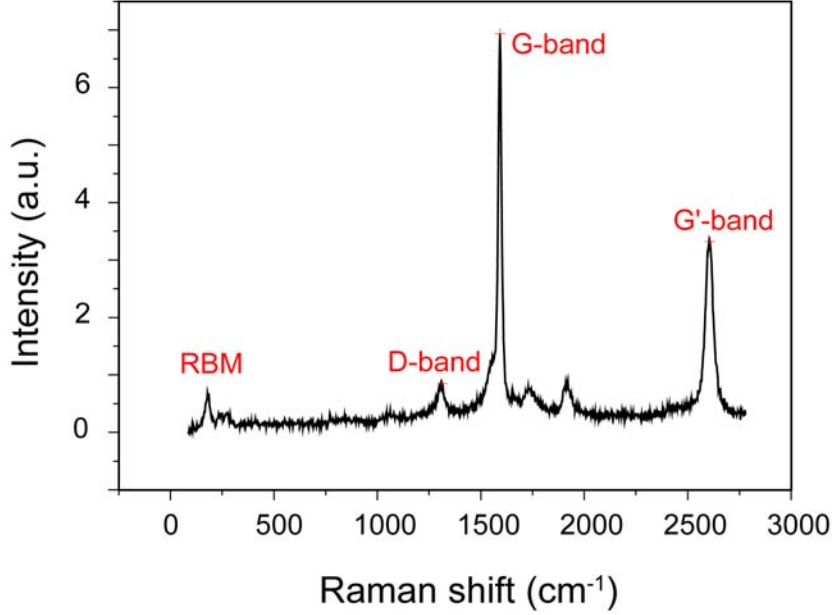


Figure 10: Typical Raman spectrum of nanotubes with different Raman bands marked in red, the radial breathing mode (RBM), the disorder-induced D-band and its corresponding second-order G'-band, the tangential G-band modes.

states, and ω_{BWF} is the BWF peak frequency at maximum intensity I_0 [67]. The BWF peak G_+^M is sensitive to the nanotube diameter since the curvature of nanotube sidewall will affect coupling to continuum states. However, the theory for phonon-plasmon coupling can not predict the band shapes and their diameter dependence. In Ferrari's work [68], they consider dynamic, curvature and confinement effects in nanotubes, and assign G- peaks the shape of Kohn anomalies, with the TO (circumferential) and LO (axial) modes, the opposite of semiconducting SWNTs.

The D-band Raman process is a one-phonon second order Raman scattering. The electron is elastically scattered back by a defect to the original k state in order to satisfy momentum conservation (Figure 9(b,c,f,g)) [69]. Therefore D-band Raman scattering is a disorder or defect-induced Raman process. The D-band peak is centered at $\approx 1350 \text{ cm}^{-1}$ and its frequency is a linear function of the laser energy [69, 70]. D-band strength can be used to measure the crystal order in SWNTs by measuring the intensity ratio of D-band and G-band as I_D/I_G [71].

The G'-band is a second order Raman process of the D-band with two phonons involved and its peak position is located at $\approx 2700 \text{ cm}^{-1}$. The electron is scattered back by another phonon with a momentum $-q$ to the original state instead of by a defect (Figure 9(d,h)). The two phonons with momentum q and $-q$ satisfy the momentum conservation. Since G'-band Raman scattering does not require any defects, the intensity ratio of $I_D/I_{G'}$ can also be used to measure the relative concentration of defects in nanotubes [71]. The G'-band also has a strong dispersion behavior as a function of laser energy, similar to the D-band.

2.5 Photoluminescence of SWNTs

Semiconducting nanotubes are direct-gap materials with the gap formed by the two nearest cutting lines closest to the K point (section 2.2). Once an electron is excited to the conduction band, it forms a hole in the valence band and photoluminescence (PL) arises from the electron and hole recombination. The optical transition in nanotubes can not be considered as transition between free particle bands (equation 18) because of the much stronger electron-hole interaction in 1D systems compared with other 2D or 3D solid materials. The bound electron-hole pairs known as excitons in nanotubes with Bohr-radii of 2-5 nm [72, 73] exhibit large binding energies E_{bind} ranging from 300 meV to 900 meV as has been confirmed by two-photon excitation [25, 74, 75].

$$E_{PL} = E_{fp} \quad (\text{Free - particle}) \quad (18)$$

PL of nanotubes results from exciton recombination that decay on picosecond time-scales [22–24] in the near-infrared spectral range with emission energies controlled mainly by the nanotube chirality (n,m) (Figure 11) [22, 25–28]. Since nanotubes consist of surface atoms only, the exciton binding energy will be sensitive to screening. This results in a significant change in the optical transition of nanotubes by changing the dielectric environment described by its relative dielectric constant ϵ .

To model the effect of the dielectric constant on the PL energies in carbon nanotubes, the interaction between different particles need to be considered besides the electron-hole Coulomb interaction. The electron-electron Coulomb interaction E_{e-e} increases the single-particle band gap counteracting the large exciton binding energy E_{bind} on the PL energy as illustrated in Figure 12(b) and equation 19.

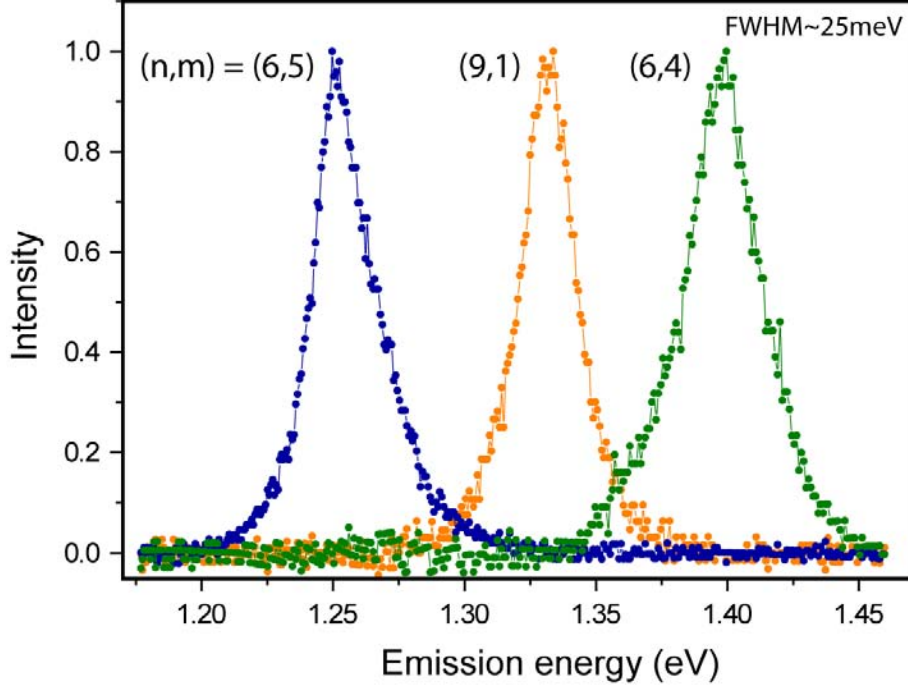


Figure 11: PL spectra of three semiconducting SWNTs with different chiralities. Different (n,m) nanotubes have different emission energies as marked beside each spectrum.

$$E_{PL} = E_{sp} + E_{e-e}^0 - E_{bind}^0 \quad (Unscreened) \quad (19)$$

Both E_{e-e} and E_{bind} are sensitive to screening and have been derived as a function of ϵ . E_{e-e} simply scales as ϵ^{-1} [48]. This is more difficult for E_{bind} because of the heterogeneous nature of the dielectric environment. Two functions were derived as $E_{bind} \propto \epsilon^{-1.4}$ [76] without considering the heterogeneous environment and $E_{bind} \propto \epsilon^{-1.2}$ [77] considering heterogeneous environment. The optical transition in the screened environment is thus summed by ϵ influenced E_{bind} and renormalized by the band gap through E_{e-e} [76–80], see equation 20 and 21.

$$E_{PL} = E_{sp} + E_{e-e} - E_{bind} \quad (Screened) \quad (20)$$

$$\Delta E_{PL} = \Delta E_{e-e} - \Delta E_{bind} \quad (21)$$

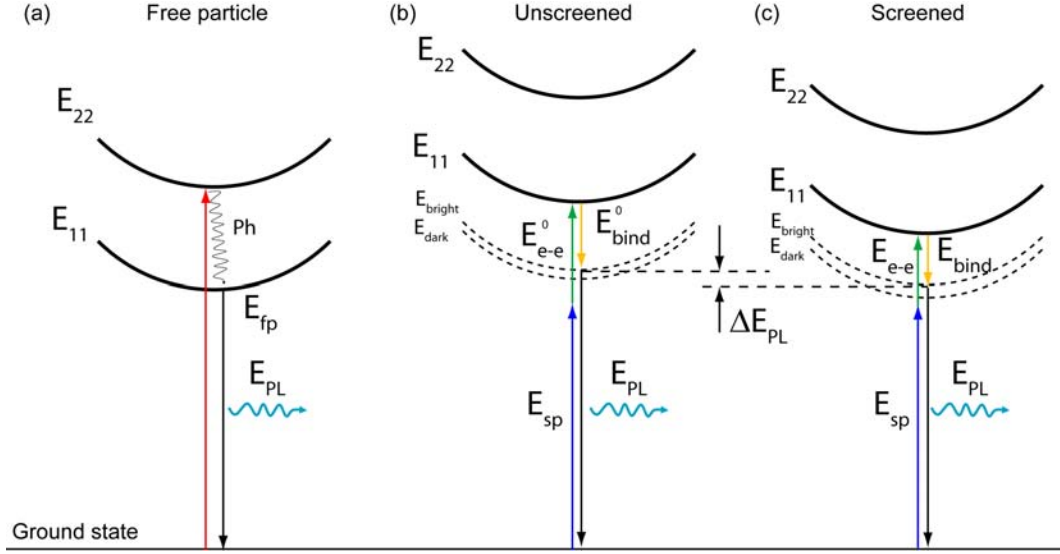


Figure 12: (a) Energy diagram in the free-particle picture. The electron is excited to E_{22} and scattered by phonons to E_{11} . When the electron recombines with the hole, a photon is emitted with energy E_{PL} , which is also the free-particle energy E_{fp} . (b,c) Energy diagram of the effect of electron-electron interaction energy and exciton binding energy on the PL energy in two environments: unscreened (b) and screened (c). The excitation and phonon scattering are neglected in order to have a clear view. The band gap energy is renormalized by electron-electron interaction energy E_{e-e} counteracting with exciton binding energy E_{bind} . E_{bright} and E_{dark} denote the bright excitonic states that emit and the dark excitonic states without emission, respectively.

In the experiment, the dielectric constant can vary from 1 (in vacuum) to a large number (for example in water). The screening effect causes a PL energy shift especially for small ϵ values < 2 , while for large ϵ value, e.g. $\epsilon > 5$, theoretical calculations [81] shows that the optical transition energy is almost the same with and without the screening effect, because the Coulomb interaction between carriers become very small. Thus the transition energy approaches the free-particle energy.

In 1D confinement in nanotubes, excitons are mobile along the nanotubes [82,83]. An exciton diffusional range of about 100 nm has been deduced from blinking traces [82,83]. In general, exciton mobility will result in an effective energy redistribution in which locally generated mobile excitons would be trapped at lower energetic levels within a diffusion radius of about $100/2$ nm = 50 nm. The resulting emission energies will therefore depend on the competition between

exciton decay and exciton mobility which is difficult to quantify experimentally. Exciton decay can be both radiative and non-radiative. SWNTs are low emissive material with quantum yield $Q \approx 10^{-3}$ dominated by effective non-radiative decays [21, 23]. Highly luminescent nanotube samples with quantum yield by over an order of magnitude have been reported from aqueous nanotube suspensions [84] and suspended nanotubes [85]. The photoluminescence quantum yield is generally used to measure the PL output for any fluorescent molecules and is expressed as

$$Q = \frac{k_r}{k_r + k_{nr}} \quad (22)$$

where k_r is the radiative decay rate and k_{nr} denotes the non-radiative decay rate. The non-radiative relaxation is associated with various pathways such as coupling to vibrations, energy transfer to the environment, or quenching by other molecules. PL measurements on single nanotubes using confocal microscopy revealed variations of emission energies and excited state decay times from nanotube to nanotube [22, 28, 32]. Moreover, near-field PL measurements along single nanotubes reveal emission energies varying along the same nanotube indicating a significant role of defects and environmental perturbations. Similarly, these localized perturbations can be expected to limit the spatial extent of delocalized excitonic states along a nanotube and thus reduce the nanotube quantum yield. The mobile excitons moving to the additional quenching site at the nanotube ends will also reduce the PL quantum yield [86, 87], details will be discussed in section 8.

2.6 DNA-wrapped SWNTs

Most growth methods of nanotubes form parallel bundles or ropes in nanotubes are held together by van der Waals interaction [88]. Nanotube bundling perturbs the electronic structure of the nanotubes and was a particular problematic in the past years. Attempts to separate the nanotubes by size or type, or to isolate them into individual nanotubes were raised up for nanotube characterizations [21, 33, 89–92]. The use of DNA for hybridization of carbon nanotube sidewalls has facilitated sorting nanotubes and building chemical sensors [18, 19, 33, 34, 89].

The DNA-wrapping mechanism is simulated by molecular density (MD) calculations [93, 94] in aqueous solution. One of the simulations started with constructing a nanotube initially wrapped with a 60 base long poly GT((GT)₃₀) sequence adopting an 18 nm pitch helix. This structure was proposed by Zheng et al. and used to explain AFM measurements in [89], see in Figure 13(a).

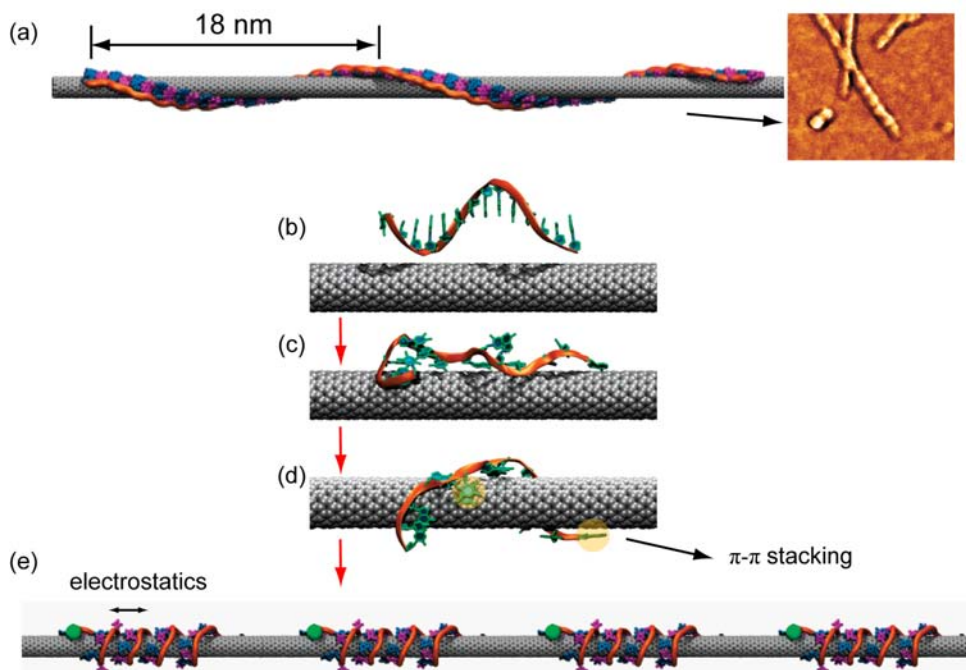


Figure 13: Simulation of DNA-wrapping around nanotubes in solution using molecular density (MD). (a) The simulations started with constructing a nanotube initially wrapped with a 60 base long poly GT((GT)₃₀) sequence adopting an 18 nm pitch helix, same as Zheng et al. used in the AFM measurements in [89]. During energy minimization oligonucleotides of general sequence adsorb on the nanotube surface via π - π stacking interaction (b to d, yellow shadow). The interactions between the phosphate backbone are electrostatic and torsional interactions. DNA forms most stable helical formation around the nanotube (e) [93].

However, both theory and calculations (Figure 13(b) to (e)) predict that this is not the most favorable configuration. The presence of SWNT in solution induces a conformational change in ssDNA that enables oligonucleotides of general sequence to adsorb on nanotube surface via the π - π stacking interaction (process from Figure 13(b) to (d)) as well as electrostatic and torsional interactions of the phosphate backbone (Figure 13(e)) [93–95], finally resulting in a helical formation of DNA-wrapping around the nanotube. However, such processes causes an overall reduction in pitch range from 2 nm to 8 nm resulting in a more tight wrapping as shown in Figure 13(e). Pitch values over about 10 nm as suggested by Zheng are unfavorable. Each strand of DNA forms a segment with finite length as determined by the number of (GT)-bases in the ssDNA.

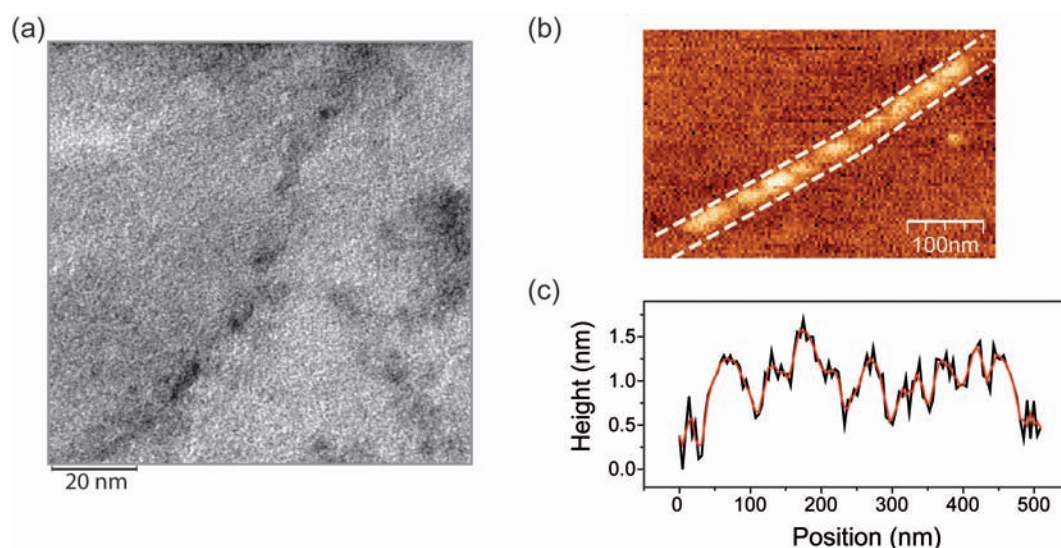


Figure 14: Morphology of DNA-nanotube hybrid systems. (a) Transmission Electron Microscopy (TEM) image of a DNA-wrapped nanotube prepared by depositing a very thin layer of DNA-nanotube from solution on the TEM grid. The scale bar is 20 nm. The distances between black areas are about 20 to 30 nm. (b) Topography of a DNA-wrapped nanotube spin-coated on mica scanned by the gold tip in TENOM. The topographic resolution is ≈ 15 nm. Segments with length of about 25 nm can be clearly seen along the nanotube which is attributed to DNA-wrapping. (c) is the profile along the nanotube summed between two white dashed lines in (b). The red curve is the smoothed data. The periodic height variations are attributed to the DNA segments.

Transmission Electron Microscopy (TEM) is applied for DNA-nanotube imaging. The contrast in the image results from the intensity of transmitted beam reflecting the volume and density difference of the material. First TEM images of the helically wrapped DNA strands around a single nanotube were presented in [96]. Figure 14(a) shows an example of TEM image of a DNA-wrapped HiPCO nanotube from the sample used in my thesis taken at PC LMU by Steffen Schmidt. Black features attributed to DNA segments with distances between 20 and 30 nm can be resolved. Signatures of DNA segments along nanotubes through topography by Jin et al. reveals ≈ 20 nm regular band patterns formed by $(GT)_{15}$ -DNA strands [95]. Such regular band patterns can also be seen in Figure 14(b), displaying the topography of a DNA-nanotube prepared on freshly cleaved thin mica layer. The resolution is ≈ 15 nm. Clear segments with length of about 25 nm can be seen along the nanotube which is attributed to DNA-wrapping. The corresponding profile curve plotted in (c) shows clearly periodic height variations.

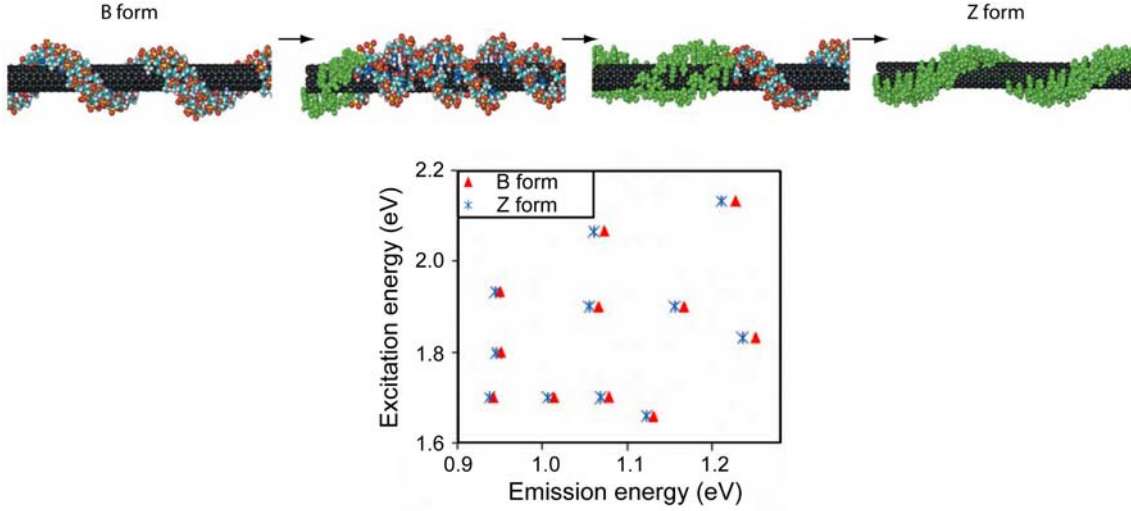


Figure 15: Illustration of DNA undergoing a conformational transition from the B form (top) to the Z form (bottom) on a carbon nanotube [97]. The emission energy of Z form wrapped DNA is redshifted due to decreased ϵ resulting from an increased surface coverage, which is without the consideration of the renormalized band gap.

The effect of helical wrapping by the charged DNA backbone on the electronic properties of SWNTs was modeled by applying a helical potential causing a symmetry break of the nanotube electronic structure and small energetic shifts for semiconducting nanotubes (0.01 meV in water) [98, 99]. It is well known that DNA-wrapping redshifts the PL energy depending on the nanotube chirality by several tens of meV compared to the values reported for micelles encapsulated nanotubes in aqueous solution [27, 100, 101], which can be attributed to an increasing ϵ [80]. This has been applied in detecting the conformational transition from the B form DNA to the Z form DNA in whole blood and tissue (Figure 15) by a decreased emission energy. This decrease in energy was attributed to a decrease in dielectric function resulting from an increased surface coverage from Z form DNA [97]. However, the emission energy decreases with the increasing ϵ from the equation 20 and 21. In [97], since they didn't consider the renormalized the band gap that counteracts with the ϵ influenced exciton binding energy, the result is therefore in opposite.

3 Tip enhanced near-field optical microscopy

Optical microscopy uniquely provides noninvasive imaging and characterization of materials. Particularly, imaging speed, sensitivity, resolution, cost-efficiency are constantly improving as new technology becomes available. Conventional optical microscopy techniques however still suffer from the diffraction limit that is a consequence of the wave nature. Evanescent waves are non-propagating waves that decay exponentially upon increasing the distances to the source. On the other hand, evanescent fields are of major importance for the understanding of optical information from the sample as there is minimum information loss with the field confined to sub-wavelength dimensions. The angular spectrum representation is a powerful mathematical technique to describe physical principles underlying the diffraction limit that is associated with the optical far-field formed by propagating waves and describes their evanescent counterpart dominating the near-field of a radiation source [102].

This section provides the theoretical explanation of the diffraction limit using the angular spectrum representation and introduces several sub-wavelength imaging concepts. High resolution imaging beyond the diffraction limit can be achieved in either far-field concepts or near-field concepts and have been carried out in many applications [102, 103]. In my thesis, a laser illuminated metal tip is introduced in near-field imaging. This section will show how optical fields are confined and enhanced at the tip apex to produce a truly nanoscale light source. Using this information, the experimental requirements and expected properties of the fields are discussed. In addition, theoretical comparison of the signal enhancement for Raman scattering and PL is shown to derive an understanding of enhancement mechanisms.

3.1 High-resolution microscopy

3.1.1 Angular spectrum representation

The angular spectrum representation can be used to describe any light propagation and light focusing in homogeneous media. Here let $\mathbf{E}(\mathbf{r})$ be the electric field at any point $\mathbf{r}=(x, y, z)$ in space. Considering a plane with $z=\text{constant}$, see in Figure 16, we can evaluate the two dimensional Fourier transform of the field \mathbf{E} as [102]

$$\hat{\mathbf{E}}(k_x, k_y, z) = \frac{1}{4\pi^2} \int \int_{-\infty}^{+\infty} \mathbf{E}(x, y, z) e^{i(k_x x + k_y y)} dx dy, \quad (23)$$

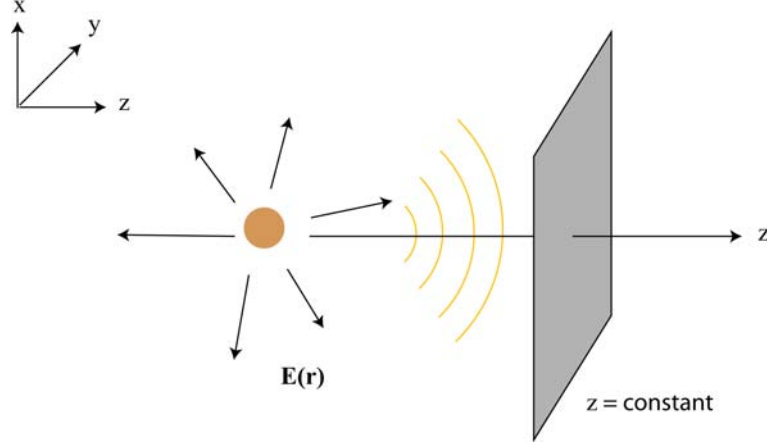


Figure 16: In the angular spectrum representation, the electric fields are evaluated in x, y plane with $z=\text{constant}$ perpendicular with an arbitrarily axis z .

here x, y are the Cartesian transverse coordinates and k_x and k_y are the corresponding spatial frequencies. Similarly, the inverse Fourier transform is expressed as [102]

$$\mathbf{E}(x, y, z) = \int \int_{-\infty}^{+\infty} \hat{\mathbf{E}}(k_x, k_y; z) e^{i(k_x x + k_y y)} dk_x dk_y. \quad (24)$$

Since we assume the field \mathbf{E} is a monochromatic field with angular frequency ω , it has to satisfy the wave equation [102, 104]

$$(\nabla^2 + k^2)\mathbf{E} = 0 \quad (25)$$

where $k = (\omega/c)n$ with n the index of refraction. Therefore we can define

$$k_z \equiv \sqrt{(k^2 - k_x^2 - k_y^2)} \quad (26)$$

with $\text{Im}(k_z) \geq 0$. By equation 24, 25 and 26, the Fourier spectrum $\hat{\mathbf{E}}$ along the z -axis can be expressed as [102]

$$\hat{\mathbf{E}}(k_x, k_y, z) = \hat{\mathbf{E}}(k_x, k_y; 0) e^{\pm i k_z z}. \quad (27)$$

thus we can say the Fourier spectrum $\hat{\mathbf{E}}$ at plane $z=\text{constant}$ along the arbitrary z axis can be determined by multiplying the spectrum in the plane at $z=0$ by the factor $\exp(\pm ik_z z)$, which is called propagator in reciprocal space. Using equation 24 and 27, we can write the inverse Fourier transform as [102,104]

$$\mathbf{E}(x, y, z) = \int \int_{-\infty}^{+\infty} \hat{\mathbf{E}}(k_x, k_y; 0) e^{i(k_x x + k_y y)} e^{\pm ik_z z} dk_x dk_y \quad (28)$$

which is known as the angular spectrum representation, representing a superposition of plane waves. For lower spatial frequencies, which means $k_x^2 + k_y^2 \leq k^2$, k_z is real and the factor $\exp(\pm ik_z z)$ is a phase factor. The plane waves propagate in the direction defined by k . For high spatial frequencies, $k_x^2 + k_y^2 > k^2$, k_z is imaginary and the factor $\exp(\pm ik_z z)$ gives the exponential decay of the field intensity, the field is called evanescent field. The two solutions can be written as [102]

$$\begin{aligned} \text{Plane waves :} & \quad e^{i(k_x x + k_y y)} e^{\pm i|k_z|z}, & k_x^2 + k_y^2 \leq k^2 \\ \text{Evanescent waves :} & \quad e^{i(k_x x + k_y y)} e^{-i|k_z||z|}, & k_x^2 + k_y^2 > k^2 \end{aligned} \quad (29)$$

therefore the angular spectrum can also be considered as a superposition of plane waves and evanescent waves. There are two boundary conditions. First, a plane wave propagating in z direction will have no oscillations in the transverse plane ($k_x^2 + k_y^2 = 0$). Second, a plane wave with highest spatial oscillations in the transverse plane ($k_x^2 + k_y^2 = k^2$) propagating in z direction will show fastest decay along the z -axis. The higher the spatial frequencies of an evanescent wave are, the faster the field decay along the z -axis will be.

3.1.2 Resolution limits

The angular spectrum representation shows if we have a radiating point source, the image far away has a finite bandwidth. On propagation from the source to the image, high frequency components are lost, e.g. evanescent waves with $k_x^2 + k_y^2 > k^2$. The bandwidth of the image can be determined using a point-spread function assuming a dipole as a radiating electric unit, whose radiation is collected by a high numerical aperture (NA) objective and focused by a second lens for point detection. The paraxial point-spread function in the image plane for a dipole oriented along the x -axis is expressed as [102]

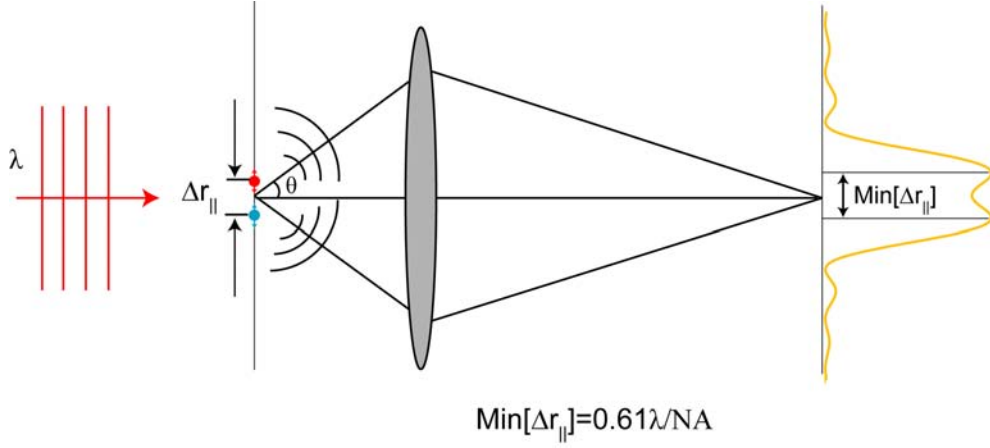


Figure 17: Illustration of the resolution limit. The two radiation point sources (red dot and blue dot) are separated by $\Delta r_{||}$, generating two point-spread functions in the image plane overlapping with each other. The minimum distance that can be resolved is limited by diffraction, being $0.61\lambda/NA$.

$$\mathbf{Lim}_{\theta_{max} \ll \pi/2} |\mathbf{E}(x, y, z = 0)|^2 = \frac{\pi^4}{\varepsilon_0^2 n n'} \frac{\mu_x^2}{\lambda^6} \frac{NA^4}{M^2} \left[2 \frac{J_1(2\pi\tilde{\rho})}{(2\pi\tilde{\rho})} \right]^2, \quad \tilde{\rho} = \frac{NA\rho}{M\lambda} \quad (30)$$

where ε_0 is dielectric constant, n and n' are reflective indices of medium, μ_x is the dipole momentum in x-axis, M is the magnification from the source to the image plane, J_1 is the first-order Bessel function and ρ is the size of the focus area [102]. The width of the point-spread function Δx is usually defined as the radial distance for which the value of the paraxial point-spread function becomes zero, which is [102]

$$\Delta x = 0.61 \frac{M\lambda}{NA} \quad (31)$$

From the equation we can see the size of the image simply depends on the NA, the wavelength and the magnification of the system. However, when there are two emitters staying close to each other separated by a distance $\Delta r_{||} = (\Delta x^2 + \Delta y^2)^{1/2}$ in the object plane, the finite width will limit the imaging to distinguish them because the point-spread functions are overlapped with each other, see Figure 17. The bandwidth of spatial frequencies $\Delta k_{||} = (\Delta k_x^2 + \Delta k_y^2)^{1/2}$ is used for resolving optical systems. Similar to the Heisenberg uncertainty principle in quantum mechanics, here we have [102]

$$\Delta k_{\parallel} \Delta r_{\parallel} \geq 1 \quad (32)$$

To minimize the separation Δr_{\parallel} that can be resolved, we need to achieve high spatial frequency Δk_{\parallel} . The upper bound of Δk_{\parallel} is given by the wavenumber $k = (2\pi/\lambda)n$, therefore the highest resolution will be $\text{Min}[\Delta r_{\parallel}^0] = \lambda/2\pi n$. In practice, the highest Δk_{\parallel} which can be reached is determined by the NA ($\text{NA} = n \sin \theta$), which is $\Delta k_{\parallel} = k \sin \theta_{max}$ ($0 < \theta < \pi/2$), resulting in the minimum distance $\text{Min}[\Delta r_{\parallel}] = \lambda/2\pi \text{NA}$. The evaluation is based on a dipole oriented along the x-axis, while Abbe's formulation considers the paraxial point-spread function of two dipoles with axes perpendicular to the optical axis and obtained the minimum distance corresponding to the distance between the maximum of one point-spread function and the first minimum of the second point-spread function. The distance is defined as

$$\text{Min}[\Delta r_{\parallel}] = 0.61 \frac{\lambda}{\text{NA}} \quad (33)$$

known as Abbe's diffraction limit. The distance between two point sources does not become distorted for dipoles with unequal strength in Abbe's diffraction limit because of this minimum-maximum overlap.

3.1.3 Sub-wavelength Imaging Concepts

It seems that the only way to have sub-wavelength resolution is available in an evanescent field, so called near-field optical microscopy. However, this technique requires close surface interaction, which is not practical in imaging the interior of cells. Life sciences pushes concrete and feasible concepts in breaking the diffraction limits in detection of propagating waves.

Sub-wavelength imaging in far-field optics by reducing the focus spot (high NA) or multiphoton excitation (small λ) pushes the diffraction limit down to 200 nm [103], e.g. confocal microscopy reduces the focal spot size using point like illumination and detection. The effective spot is described by

$$E_{illu}(x, y, z) E_{em}(x, y, z) \approx E^2(x, y, z) \quad (34)$$

resulting in a reduction of the spot by $\approx \sqrt{2}$. Precise single molecule localization with nanometer accuracy can be recorded by fixing the position of each emitting molecule in the (x, y) plane. The accuracy is only determined by the signal-to-noise ratio and instrument response function [105–108]. Moreover, if the photons arrive at the detector, they can be distinguished by energy, polarization or arrival time, they can be separated in the image with far-field techniques even in case they are very close or overlapped. All this can be achieved by active control, e.g. through stimulated emission depletion (STED) [109] or passively using stochastic readout based on photophysical and photochemical effects of the source such as photo-blinking, -bleaching or -switching through photo-activated localization microscopy (PALM) [110] and stochastic optical reconstruction microscopy (STORM) [111]. The accuracy of both PALM and STORM rely on the "quality" of data requiring high signal-to-noise ratio and efficient detection. The absorption cross section or Raman scattering cross-section of a molecule is at least two or three orders of magnitude smaller than the cross section of a focused laser beam, resulting in very weak signal. Fluorescence, on the other hand, exhibits a low background signal, which provides much better signal-to-noise ratios [112]. The far-field schemes providing no signal enhancement, are therefore not suitable for Raman scattering measurements or weakly fluorescent materials.

The central idea of near-field optical microscopy is to retain the spatial frequencies associated with evanescent waves and thereby extend the spatial resolution beyond the diffraction limits. The evanescent waves are bound to the surface of the specimen and decay exponentially away from the surface on a nanometer scale, which can be understood from the angular spectrum representation [104]. Probes close to the sample that can carry evanescent waves are generally used in scanning near-field optical microscopy (SNOM). Such probes can be illuminated aperture probes (Figure 18(a)) or illuminated metal tips (Figure 18(b)).

The commonly used aperture probes are based on a metal coated fiber tip with an uncoated spot at the apex. The metal coating, most often an aluminum coating, prevents the field from leaking through the sides of the probe. The light propagating in the fiber can be considered as propagation in a hollow metal waveguide [113, 114]. SNOM using aperture probes for the first time allowed optical imaging of nanometer-scale features such as tissue sections in the early 1990s [115] and were applied in single molecule fluorescence lifetime measurements [4, 116]. Later on, near-field imaging combined with shear-force microscopy were used in living cell imaging with sub-wavelength resolution [3, 117]. Unfortunately, the diameter of the waveguide decreases constantly towards the probe apex, leading to a cut-off of waveguide modes. For small diameter apertures, the propagating field decays exponentially towards the tip apex, e.g. only $\leq 10^{-4}$

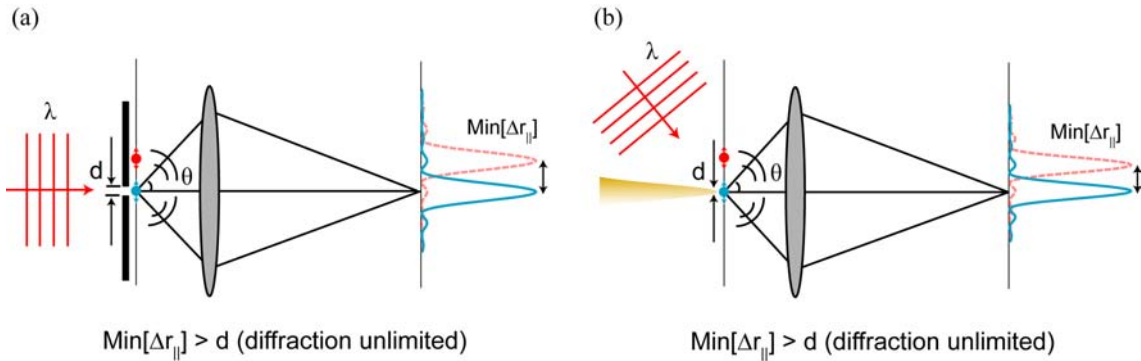


Figure 18: Two approaches in near-field optical microscopy. (a) An aperture with diameter d is placed in front of the sample to reduce the excitation volume, the optical resolution is determined by the aperture size. (b) Alternatively, an illuminated sharp metal tip is placed in front of the sample and works as local excitation source, hence the optical resolution is determined by the diameter of the tip apex. The second approach is so called tip-enhanced near-field optical microscopy (TENOM), which is used in this work.

fraction of light coupled into fiber is emitted by aperture with diameter 100 nm, which limits the optical resolution or excitation efficiency.

Alternatively, a laser illuminated metal tip can be used for local field enhancement for tip-enhanced near-field optical microscopy (TENOM). This idea has been first suggested by Wessel in 1985 [5], even before the invention of atomic force microscopy (AFM). The local field has similar origins as the lightning-rod effect in electrostatics. In general, this scheme can be applied throughout the electromagnetic spectrum including THz, IR and VIS [118–120]. It was also pointed out that not only the excitation is enhanced due to the strong near fields, but also the inelastic spectroscopic response close to a metal particle [121, 122], in our case a metal tip [4, 7–12], is enhanced and modified because of the presence of metals. The techniques is therefore applicable to weak emitters with low quantum yield and intrinsically weak signals such as Raman scattering and is relevant to the realm of nano-science, conveying much more information via evanescent waves through their spectrum.

3.2 Field-enhancement at a metal tip

Field enhancement near nanoscale metal structures plays a central role for optical phenomena such as surface enhanced Raman scattering (SERS), second-harmonic (SH) generation [123],

and near-field microscopy. It is generally accepted that the largest contribution to the intensity amplification results from the electric field enhancement that occurs in the vicinity of small, interacting metal nanoparticles that are illuminated with light resonant or nearly resonant with the localized surface-plasmon frequency of the metal structure [102]. For understanding the field enhancement at the metal tip, we can extend the particle geometry straightforward to a sharp metal tip with finite length and small diameter at the apex. As far as the tip diameter is much smaller than the incident wavelength, $d \ll \lambda$, we can treat the tip apex as a single dipole. The field distribution around the tip is manifested by the charge density induced by the incident laser field. Therefore it is sensitive to the laser field polarization. The incident light drives the free electrons in the metal along the direction of polarization. While the charge density is zero inside the metal at any instant of time, charges accumulate at the metal surface. Figure 19(a) shows the induced charge density for two situations [124]. When the incident polarization is perpendicular to the tip axis, diametrically opposed points on the tip surface have opposite charges. As a consequence, the foremost end of the tip remains uncharged and no field enhancement is achieved. On the other hand, when the incident polarization is parallel to the tip axis, the induced surface charge density is almost rotationally symmetric and has the highest amplitude at the end of the tip [124–127], as illustrated in Figure 19(b).

In order to discriminate the signals from sample materials against the background from the illuminated area, the magnitude of the field enhancement factor is crucial for imaging applications. The far-field signal arises from the direct illumination of the sample without the presence of the tip. The enhancement factor is determined by the ratio of near-field signals and far-field signals taking the illuminated area into account e.g. the area determined by the tip for near-field and the area of the laser focus for far-field. The image contrast can reflect the higher or lower enhancement factors. To maximize the field enhancement, alternative probe shapes and materials have been proposed. Analytical calculations yielded that the use of a finite probe matched to the excitation source exhibiting very low radiation damping generates a higher field enhancement [127–131]. For all probe designs, the vicinity of the sharp tip can be treated as a dipole $\mu(\omega)$ with the magnitude [102]

$$\mu(\omega) = \begin{bmatrix} \alpha_{\perp} & 0 & 0 \\ 0 & \alpha_{\perp} & 0 \\ 0 & 0 & \alpha_{\parallel} \end{bmatrix} \mathbf{E}_0(\omega) \quad (35)$$

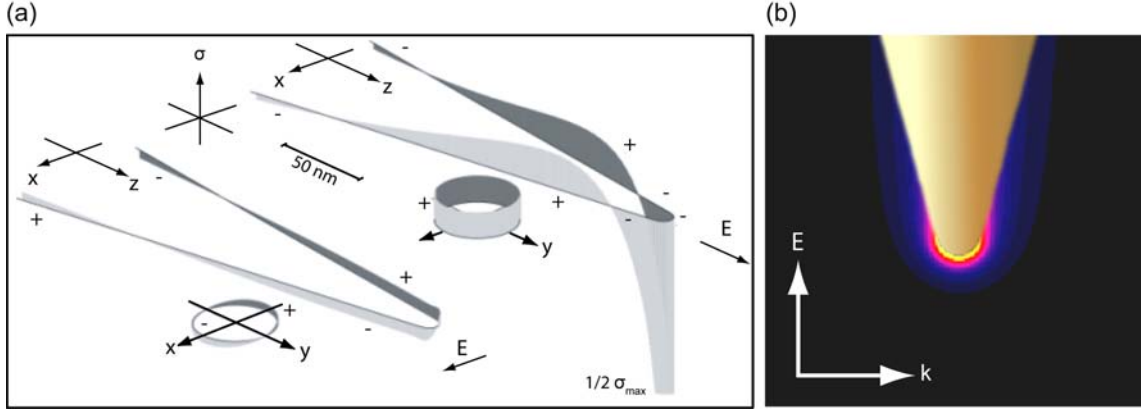


Figure 19: (a) Induced surface charge density. The surface charge forms a standing wave. When the incident polarization is perpendicular to the tip axis, diametrically opposed points on the tip surface have opposite charges. As a consequence, the foremost end of the tip remains uncharged and no field enhancement is achieved. When the incident polarization is parallel to the tip axis, the induced surface charge density has the highest amplitude at the end of the tip. (b) Laser illuminated gold tip. The laser polarization is parallel to the tip axis and indicated by \mathbf{E} and vector k [124].

$\mathbf{E}_0(\omega)$ is the electric field without the tip. α_{\perp} denotes the transverse polarization in the x,y plane perpendicular to the tip axis, while α_{\parallel} denotes the longitudinal polarization along the tip axis. They are defined by [102]

$$\alpha_{\perp} = 2\pi\epsilon_0 R^3 \frac{\epsilon(\omega) - 1}{\epsilon(\omega) + 2} \quad (36)$$

and

$$\alpha_{\parallel} = \pi\epsilon_0 R^3 f_{enhance}(\omega). \quad (37)$$

ϵ_0 is the bulk dielectric constant of the tip, R is the tip diameter and $f_{enhance}$ is the enhancement factor. With this tip dipole function, the electric field in the vicinity of the tip can be calculated as [102]

$$\mathbf{E}(\mathbf{r}, \omega) = \mathbf{E}_0(\mathbf{r}, \omega) + \frac{\omega^2}{\varepsilon_0 c^2} \vec{\mathbf{G}}(\mathbf{r}, \mathbf{r}_0, \omega) \mu(\omega), \quad (38)$$

where \mathbf{r}_0 specifies the origin of the dipole μ and $\vec{\mathbf{G}}$ is the dyadic Greens function.

3.3 Signal enhancement for Raman scattering and photoluminescence

TENOM is the ideal technique for optical characterization of both Raman and PL of nanostructures since the confined and enhanced electric field at the tip apex offers both high optical resolution and signal enhancement. Since STED, PALM/STORM are lacking signal enhancement, they are not suitable for weakly luminescent materials and Raman scattering measurements. Raman scattering and photoluminescence are distinct optical processes, involving different electronic states of the sample material with different degrees of coherence, therefore, the enhancement effects for each signal are expected to vary. A brief discussion of the enhancement mechanisms is given here.

Although Raman scattering has extremely low scattering cross-sections which are typically 14 orders of magnitude smaller than the cross-section of fluorescence in the case of organic molecules, surface enhanced Raman scattering (SERS), induced by nanometer-sized metal structures, has been shown to provide enormous enhancement factors of up to 10^{15} allowing for Raman spectroscopy even on the single molecule level [132, 133]. The strongest contribution to SERS is of electromagnetic origin, caused by the enhancement of the local field E_{local} with respect to the incident field E_0 .

In tip-enhanced Raman scattering and SERS, the electromagnetic enhancement factor M_i is defined as the ratio between the measured Raman cross section in the presence and in the absence of the metal tip for each scatterer i . The integrated photon flux Φ_{Raman} is a linear function of the intensity of the incident laser light I at frequency ω_I and results from the sum of the Raman scattering cross sections σ_R^i of all scatterers within the detection volume [134]

$$\Phi_{Raman} = \frac{I_I}{\hbar\omega_I} \sum_{i=1}^N \sigma_R^i M_R^i \quad (39)$$

The electromagnetic enhancement M_i is caused by enhancement of E_0 for both the incident field

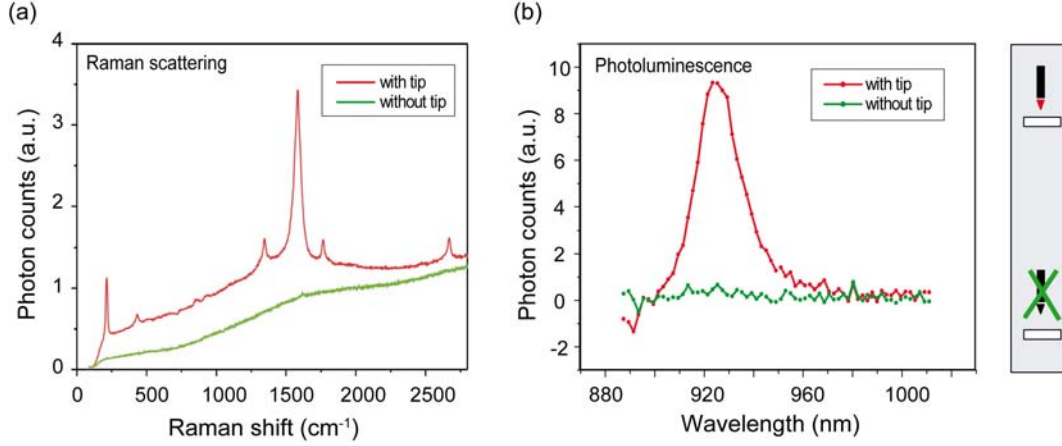


Figure 20: Signal enhancement measured in both Raman scattering spectrum (a) and PL spectrum (b). Without the gold tip (green curves), both Raman and PL signals are weak and hard to distinguish from the background signal. With the gold tip (red curves), different Raman features and emission band are strongly enhanced and rise up clearly [139].

at ω_I and the scattered field at $\omega_I - \omega_\nu$ and can be expressed as the product with the total local electric field E_{local} [134]

$$M_R = \left[\frac{E_{local}(\omega_I)}{E_0(\omega_I)} \right]^2 \left[\frac{E_{local}(\omega_I - \omega_\nu)}{E_0(\omega_I - \omega_\nu)} \right]^2 \approx \left[\frac{E_{local}(\omega_I)}{E_0(\omega_I)} \right]^4, \quad (40)$$

here $\omega_\nu \ll \omega_I$ for Raman scattering. Near-field Raman scattering induced by a laser-irradiated metal tip has been experimentally demonstrated by several groups. An enhancement in Raman scattering of up to 10^6 could be achieved [8, 10, 30, 133, 135–138]. For a single spherical particle M_R is supposed to be much lower. Figure 20 shows Raman scattering spectra of a single nanotube with and without the presence of the metal tip. Intensities of different Raman bands increase enormously by the enhancement of the tip.

The PL intensity is determined by the number of excitons relaxed radiatively from excited states to the ground state. The enhancement of PL therefore depends on the excitation rate and the quantum yield Q denoting the fraction of emitted photons (section 2.5). Accordingly, the PL enhancement due to the presence of the metal tip can be written as [134]

$$M_{PL} \approx (E_{local}/E_0)^2(Q_{PL}/Q_{PL,0}). \quad (41)$$

Here, Q_{PL} and $Q_{PL,0}$ are PL quantum yield with and without tip, respectively. In terms of the Raman enhancement (equation 40), the PL enhancement can be written as [134,140]

$$M_{PL} \approx (M_R)^{1/2}(Q_{PL}/Q_{PL,0}). \quad (42)$$

In a near-field measurement, both radiative decay rate k_r and non-radiative decay rate k_{nr} are affected by the presence of the metal structure: k_r is modified by the enhanced fields at the molecule location (Purcell effect) [140–142] and k_{nr} is increased by non-radiative decay channels created by energy dissipation inside the metal tip [140,143]. The $Q_{PL,0}$ of nanotubes is very low because of the high non-radiative decay rate k_{nr} . Thus Q_{PL} can be significantly increased in the presence of the tip as the enhanced rate k_r will predominantly increase the quantum yield. Such enhancement is not possible for systems with a quantum yield already close to 1, such as fluorescent dyes or quantum dots.

Since the distance between emitter and metal tip is very small (about 1 - 2 nm), non-radiative transfer of energy from the electronically excited molecule to the metal followed by non-radiative dissipation has to be taken into account. This process represents an additional non-radiative relaxation pathway and can extinguish the fluorescence. While the theory of energy transfer between molecules and flat metal interfaces is well understood in the framework of phenomenological classical theory [143,144], nanometer sized objects are more difficult to describe. Tip-induced radiative rate enhancement and quenching has been studied in literature theoretically [145–147]. Experiments on model systems formed by single molecules and spherical metal particles revealed a complex distance dependent interplay between competing enhancement and quenching processes [140,148,149]. Small cone angles in tip-shaped metal structures are expected to reduce energy dissipation as compared to spherical particles [147]. Details will be discussed in section 5.4.

4 Experimental

4.1 Tip-enhanced near-field optical microscopy

The experimental setup used in this thesis is based on an inverted optical microscope with an x, y scanning stage for raster scanning a transparent sample (Figure 21). The light source used for Raman scattering and photoluminescence experiments presented in this work is a HeNe laser operating at 633 nm. The laser beam is reflected by a dichroic beam splitter and focused by a high numerical aperture (NA) objective (1.4 NA) onto the sample surface. A sharp gold tip is positioned within the focus of the beam and maintained above the sample surface at a distance of ≈ 2 nm by means of a sensitive shear-force feedback mechanism [150]. The optical signal is collected with the same objective, transmitted by the beam splitter and filtered by a notch filter to remove the fundamental laser light. The signal is detected either by a combination of a spectrograph and a cooled charged coupled device (CCD) or by a single-photon counting avalanche photodiode (APD) after spectral selection by a narrow band pass filter or a longpass filter. A near-field optical image is established by raster scanning the sample and simultaneously recording the optical signal, as well as the shear-force detector recording topographic information.

In order to extract the information contained in evanescent fields, the tip-sample distance is required to be smaller than the field confinement (see section 3.2). Sensitive feedback is demanded in near-field measurement for such short range interaction. Shear-force feedback mechanism offers sensitive detection for very small tip-sample separation by coupling the shear-force interaction between tip and sample to a tuning fork thereby modifying the mechanical resonance of the tuning fork [150].

The tuning forks are made of quartz with two prongs (Figure 22(a)). These two prongs move oppositely in x -direction as indicated in Figure 22(a). The motion for the driven tuning fork is modeled as an effective harmonic oscillator (assuming small oscillation amplitude), the amplitude and phase response are given by [102, 151]

$$A(f) = \frac{A_0}{\sqrt{(1 - (f/f_0)^2)^2 + (f/(f_0Q))^2}}, \quad (43)$$

and

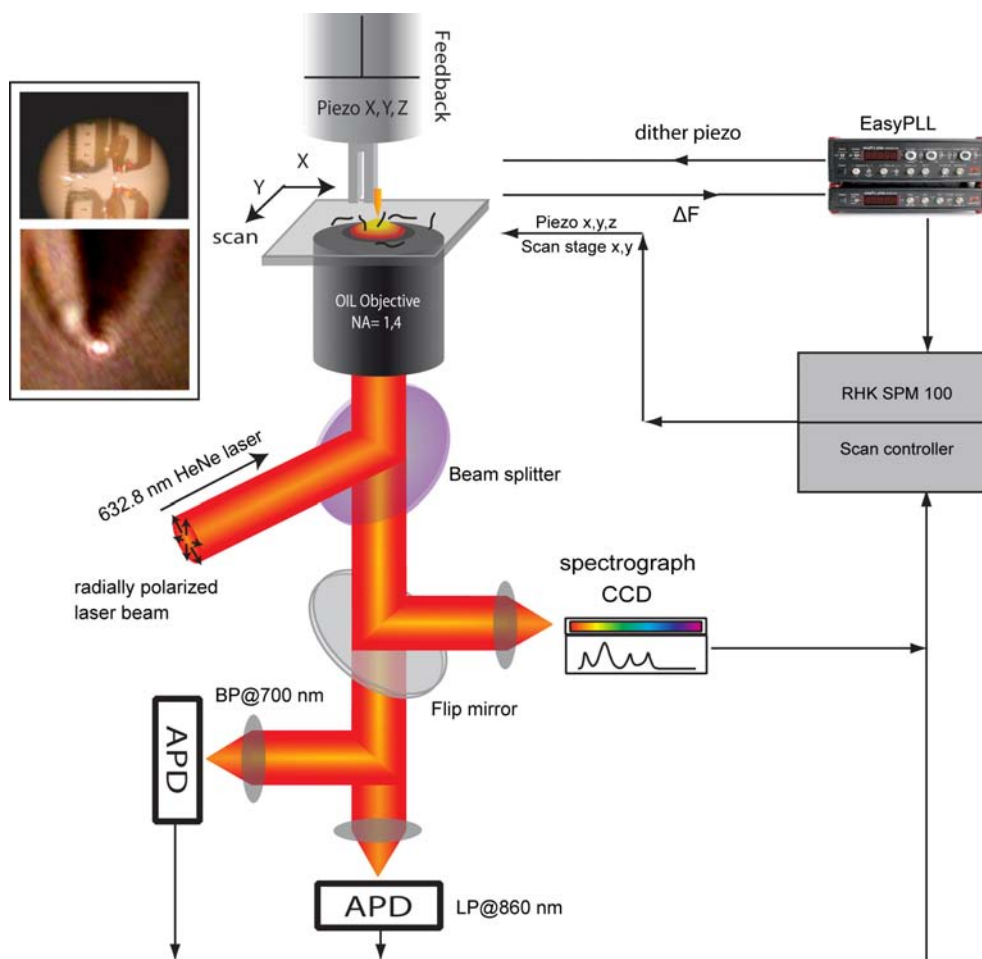


Figure 21: Schematic of the experimental setup combining an inverted optical microscope with an x, y scan stage for raster scanning a transparent sample and a shear-force control detector. HeNe laser at 632.8 nm is used for excitation to observe simultaneous Raman scattering and photoluminescence of carbon nanotubes. A sharp metal tip is positioned in a tightly focused radially polarized laser beam to get signal enhancement and topography. The optical signal is detected either by two avalanche photodiodes (APDs) for the VIS (Raman) and NIR (PL) spectral range or by a combination of a spectrograph and a CCD. An easyPLL (Phase Locked Loop) is used for dithering piezo and monitoring the frequency shift.

$$\phi(f) = \tan^{-1} \left[\frac{(1 - (f/f_0)^2)Q}{f/f_0} \right], \quad (44)$$

here f_0 is the resonance frequency, which is commonly about 32.768 kHz . After amounting a gold tip for near-field probing, the resonance frequency drops by hundreds of Hz depending on the mass of tip and adhesive, e.g. in Figure 22(b) the resonance frequency of the tuning fork is 31.428 kHz with a gold tip. The amplitude of the oscillation follows a Lorentzian lineshape function (black curve in Figure 22(b)) with a Q-factor [102,151],

$$Q = \frac{f_0}{\Delta f} \quad (45)$$

where Δf is the full width at half maximum (FWHM). The Q-factor of a tuning fork is in the range of 10^3 - 10^4 at ambient condition and can be higher in vacuum. Such high Q-factor results from the two prongs moving in opposite direction, so there is no center-of-mass motion. The bandwidth of the resonance peak is inversely proportional to the Q-factor, resulting in a slower response time of the amplitude for the tuning forks with high Q-factors. The response time of tuning fork can be defined as [102,151]

$$t_{response} = Q/2f_0 \quad (46)$$

The response time counteracts with the Q-factor in the amplitude feedback mode. It seems that the response of the phase does not suffer from this problem, but the phase shift is not clearly assigned to changes in tip-sample distance and hence is difficult for feedback controlling. Using resonance frequency shifts as a feedback signal is proposed, which works in the way that the vibration of the tuning forking is always adjusted so that the phase shift corresponds to the phase shift at resonance. In this method, also known as frequency modulated mode (FM-mode), the phase shift and the resonance frequency change instantaneously when the tip-sample interaction changes. Figure 23 describes such a variation. The changes in the tracked frequency are not affected by the Q-factor, also, the system response is independent of the tuning fork quality factor. In our work, the frequency shift is monitored by a phase locked loop (PLL, easyPLL, Nanosurf AG). The easyPLL consists of a controller and a detector, which are used for regulating the frequency from the tuning fork and outputting an analog voltage that is proportional to the change in the tuning fork frequency, see Figure 21 and 22. The voltages

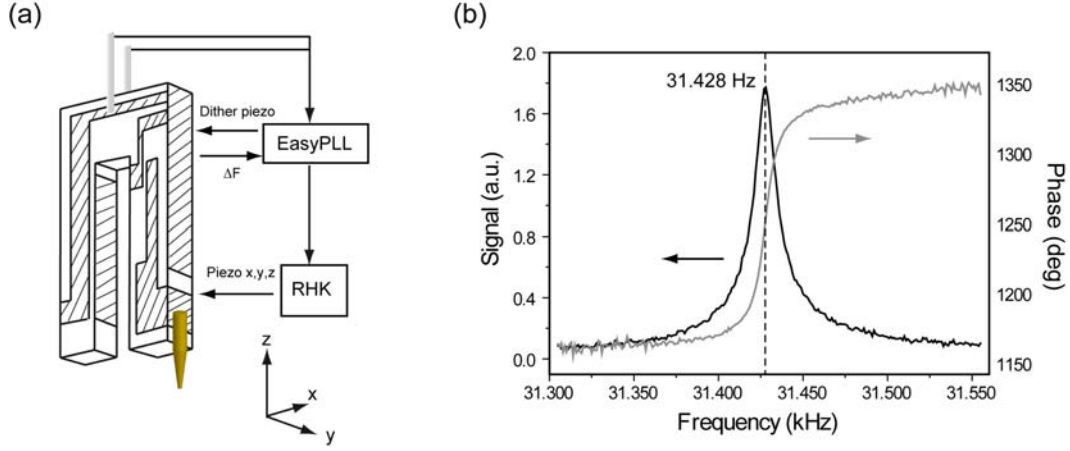


Figure 22: (a) Piezo element-tuning fork used in our setup. The dashed area are contact layer. A gold tip is mounted at the end of one of the prongs. The output signal from the detector is amplified/weakened by the controller and then applied for dithering the tuning fork. (b) Amplitude (black, left) and phase (gray, right) signals of a tuning fork mounted with a gold tip, showing a resonance frequency of 31.428 kHz.

are further calibrated into topographic height to form topography images. In FM-mode, the output signal from the detector is only amplified/weakened by the controller and then applied for dithering the tuning fork. An RHK control equipment (manufacturer: RHK Technology, USA) is used to apply a voltage to an x,y,z piezo to control the position of the tip as well as the data acquisition, see in Figure 21 and 22.

To establish a strong field enhancement at the tip, the electric field of the exciting laser beam needs to be polarized along the tip axis (section 3.2). To fulfill this condition in our on-axis illumination scheme, we use a higher order radially polarized laser mode [125,152] with strong longitudinal electric field component along the tip axis in the center of the focus. The HeNe laser device yields a fundamental Gaussian beam profile with the electric field transverse to the propagation direction, perpendicular to the tip axis. To convert the Gaussian laser mode to higher order laser modes, one can insert phase plates at different regions in the beam to retard the phase in different degrees. Shown in Figure 24(a), the mode converter is composed of 4 quadrants $\lambda/2$ waveplates with different optical axes. Each segment is oriented in the way that the beam polarization is retarded until it forms a radial direction. A spatial filter is required to filter out the unwanted higher-order modes. The finally obtained laser mode has a radial polarization in the transverse direction and non-propagating component in the longitudinal

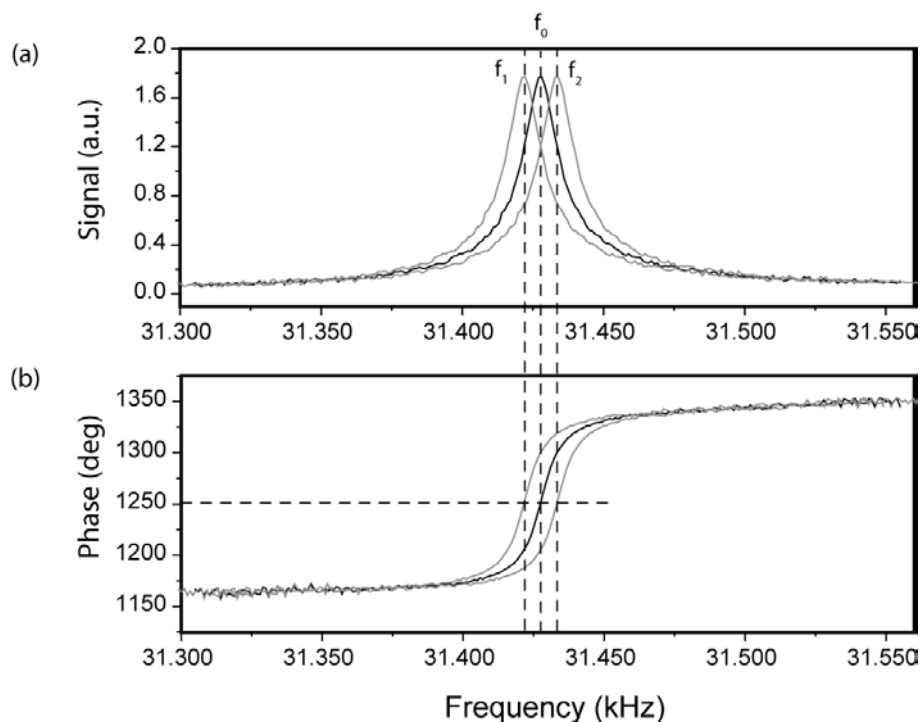


Figure 23: Frequency modulated mode signal. Amplitude (a) and phase (b) of the tuning fork mounted with a gold tip with resonance frequency at 31.428 kHz. The frequency and phase change with the tip-sample interaction. The changes in frequencies tracked is not affected by the Q-factor, also, the system response is independent of the tuning fork quality factor. See the text for details

direction in the center as simulated in Figure 24(b).

4.2 Gold tip fabrication

The key component in the TENOM is the laser illuminated metal tip. The tip fabrication has been established early in the context of field-ion microscopy (FIM) and scanning tunneling microscopy (STM) [153]. For STM, the tip shape is not crucial unless there is a foremost atom and there is sufficient conductivity along the tip. However, the influence of tip shape and material in TENOM is more important since the tip determines the resolution and field enhancement occurring at the extremity of the tips [127–130]. Tips from electrochemically etched gold wires have been proven to provide both high resolution imaging and strong field enhancement [10–12, 154]. Production of well-defined and reproducible tips is a very tedious

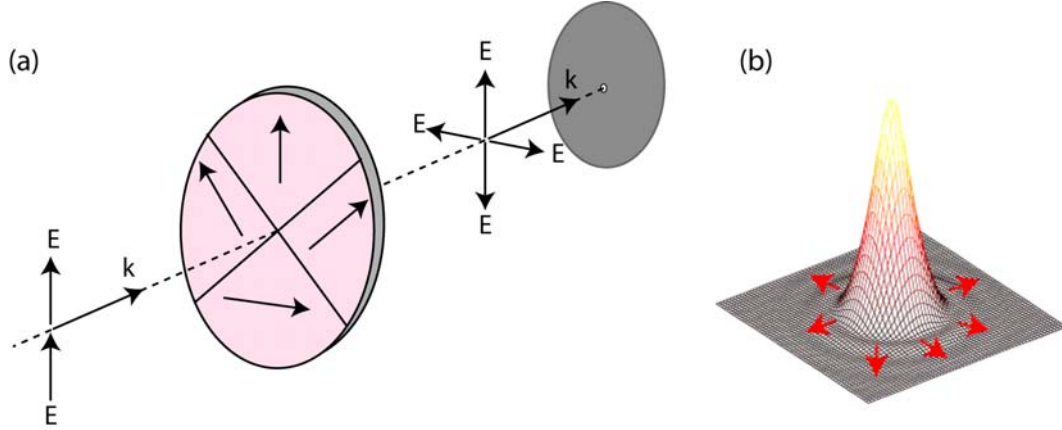


Figure 24: Mode converter. (a) the mode converter consists of four quadrants waveplates oriented in different optical axis in order to rotate the polarization into radial directions. A spatial filter with diameter $25 \mu\text{m}$ is used to filter out the unwanted higher-order modes. (b) Simulation of field of radially polarized laser beam, courtesy of Antonio Virgilio Failla.

task, and the yield to have a sharp tip with strong field enhancement is typically low being only 20%-30% [155].

The gold tips used in this work are electrochemically etched from $100 \mu\text{m}$ thick gold wires (manufacturer: ChemPur (Germany), purity: 99.995%). The gold wire is dipped in to a solution of hydrochloric acid (manufacturer: Sigma-Aldrich, purity: 37%) and a periodic voltage is applied. Figure 25 shows the schematic of the etching procedure. A function generator is used to generate the periodic voltage, with 3kHz frequency and 10% duty circle (determines the on-off time). The voltage used, usually 8 volts, is sent through a switch button and applied to the gold wire that dipped in the HCl solution centered in a circular-electrode made by platinum wire (manufacturer: ChemPur (Germany), purity: 99.99%, diameter: $100 \mu\text{m}$) $\approx 0.5 \text{ mm}$ below the interface of solution and air. The Pt ring can direct the current around the gold wire.

The chemical reaction occurs on the gold wire in HCl after applying voltage is following [156]



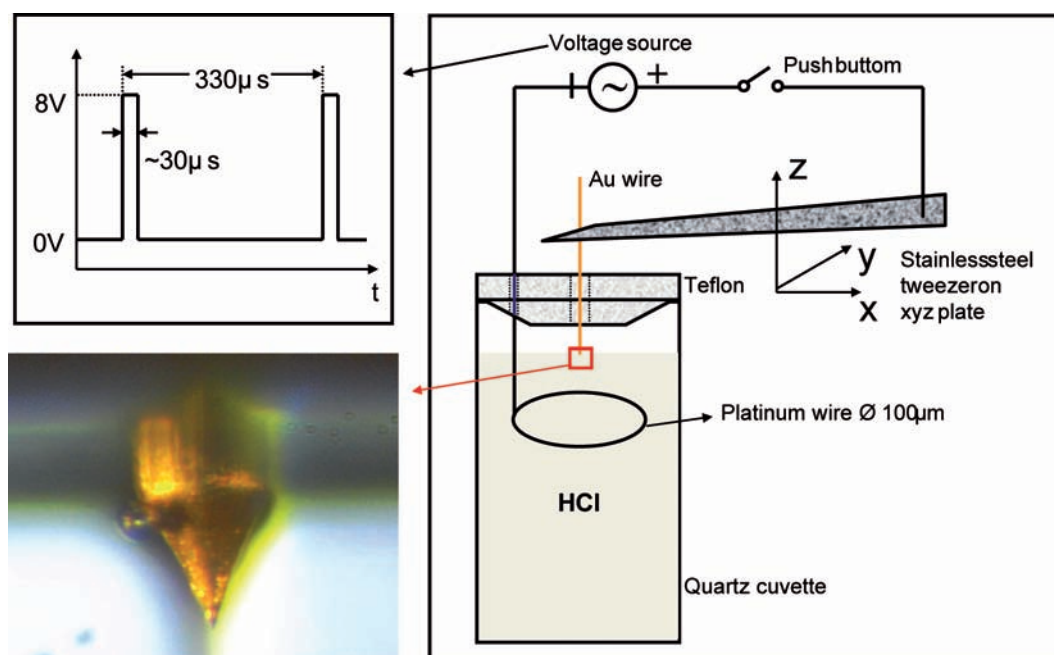


Figure 25: Schematic of the etching procedure. On the right, the gold wire is dipped in to a solution of hydrochloric acid and a periodic voltage is applied. The tip is positioned in the center of a circular-electrode made by platinum. A function generator is used to generate periodic voltage pulses, as shown on the upper left. The lower left image shows an etched tip below the meniscus surface of the HCl solution through a telescope.



The tip diameter decreases faster at the end of the gold wire. After continuously clicking the switch button for 2 or 3 minutes, a gold tip can be formed as shown in Figure 25. A x,y,z-axes position stage is used here to dip the tip $\approx 100 \mu\text{m}$ further into the HCl solution and after 2 or 3 times more clicking the switch button (this step is only from the experience to obtain sharper gold tip), the etching procedure is finished. The tip drawn out from the HCl solution is usually rinsed by distilled water to remove residues. The size of the apex as well as the roughness of the tip surface are mainly determined by the voltage amplitude and the purity of HCl. The size of bubbles formed by current flux, can be seen in the lower left image in Figure 25, directly effects the etching speed and roughness of the tip surface. Best quality gold tips result in the

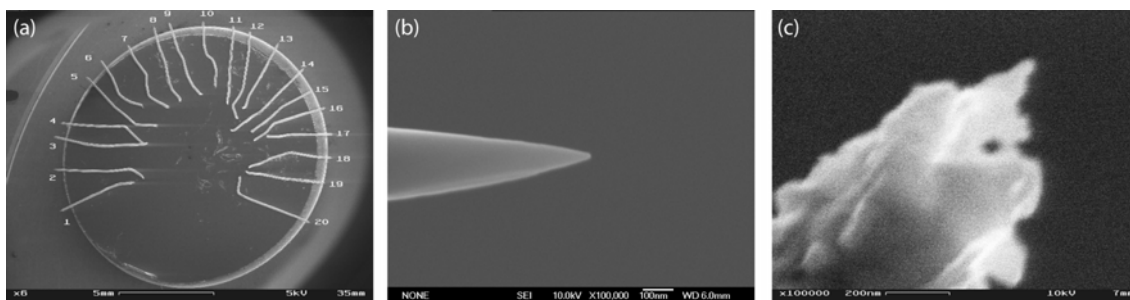


Figure 26: SEM images of gold tips. (a) SEM image of a whole tip sample holder with 20 gold tips stuck on. Usually tips are marked with numbers for later selection. (b) and (c) are examples for a good tip and a bad tip, respectively. The diameter of the tip in (b) is about 10 nm.

case of a continuous flow of small bubbles. The switch button is used to avoid too rapid and uncontrollable etching. With good control and parameter setting, one can achieve tip diameters down to 10 nm, giving near-field optical resolution below 10 nm.

Scanning electron microscope (SEM) is the next necessary tool to select gold tip candidates for near-field measurements. After collecting 2 or 3 SEM probes each with ≈ 20 gold tips, see Figure 26(a), SEM is used to resolve the tip ends and then select tips with diameter below 50 nm as possible near-field probes. As the tip etching is still a not perfectly controllable procedure, tips with enormous large diameter (hundreds of nanometers) or rough surface often exist among all the tips fabricated. Figure 26(b) and (c) give a good comparison between a good tip and a bad tip. However, the roughness of the tip surface is usually not a problem for topography measurements as far as the end is small, the tip quality is more critical for the field enhancement and there is still no way to evaluate how the field enhancement depends on the tip size in the real experiment. Sometimes a perfect shaped gold tip with diameter 15 nm might not give any enhancement because of an additional surface layer of carbon that increases the tip-sample distance, and sometimes a bad tip, e.g. Figure 26(c) gives enhanced near-field signal.

4.3 SWNTs sample preparation

Different types of nanotube materials are used in my present work. The samples are prepared and listed as following:

1. HiPCO nanotubes spin-coated on glass cover slide. HiPCO nanotubes were first dispersed in

dichloroethane by sonicating in a ultrasonic water bath for about 20 minutes. The concentration is very low that the solution appears almost transparent. About 20 μL solution was spin-coated on a glass cover slide.

2. DNA-wrapped HiPCO nanotubes spin-coated on glass cover slide. DNA-wrapped HiPCO nanotubes were prepared following the recipe in Ref. [33]. 1 mg/ml of ssDNA was mixed with 0.1M NaCl solution as aqueous DNA solution, then mixed with 1 mg of as-produced HiPco nanotube. The mixture was kept in an ice-water bath and sonicated for 90 min. After sonication, the samples were divided into 10 of 0.1 ml aliquots, and centrifuged for 90 min at 16,000g to remove insoluble material. The final DNA-dispersed nanotube solution was spin-coated on glass cover slide by about 50 μL .

3. DNA-wrapped CoMoCAT nanotubes spin-coated on thin mica layers. DNA-wrapped CoMoCAT nanotubes solutions are provided by Prof. Mark Hersam from Northwestern University. The CoMoCAT nanotubes are grown using CoMo alloy catalyst process [157]. The nanotubes were sorted by using discriminating surfactants and wrapped by DNA after sorting. Chirality enriched materials dominated by (6,5) nanotubes were finally obtained. About 100 μL nanotube solution was spin-coated on a freshly cleaved thin mica layer glued on a glass cover slide. The mica layer was positively charged with Mg^{2+} ions by exposure to 1 M MgCl_2 to make the negatively charged DNA-site of the hybrid adhere to the surface [95].

5 Near-field Raman and PL imaging and spectroscopy of SWNTs

Optical microscopy uniquely provides noninvasive imaging and characterization of materials and has been widely applied as a dominant characterization technique for investigation of structural and electrical properties of carbon nanotubes [36]. Single nanotube measurements revealed both tube-to-tube variations of phonon modes [30, 31], emission energies [28, 32] and excited-state lifetimes [22] for micelles-encapsulated tubes indicating the significance of both defects and environmental perturbations. For applications as 1D wires in long range energy and charge transfer, such variations occurring along individual nanotubes will play an important role. The spectroscopic data obtained in conventional confocal microscopy, on the other hand, only represents an average over a nanotube section of about 300 nm (Section 3.1.2). As introduced in Section 4.1, TENOM allows for simultaneous near-field Raman and photoluminescence (PL) imaging of SWNTs with a spatial resolution down to 10 nm, and is thus ideally suited to provide deep insights of optical properties of single nanotubes in ambient environment.

In this section, I will present optical characterization of carbon nanotubes using TENOM that provides superior spatial resolution down to 10 nm and also enormous signal enhancement. Section 5.1 starts with how typical near-field images are formed and what we can learn from the high resolution Raman images. High resolution PL images and spectra, presented in section 5.2, reveal PL energy variations along the nanotubes, as well as localized PL appearing as single spots or regular spaced dots. Simultaneously obtained near-field Raman scattering and PL images reflect the correlation between phonon properties and electronic properties of nanotubes. Whether PL is defect-induced as demonstrated in [158] and the correlation between D-band and PL will be discussed in section 5.3. Section 5.4 provides a detailed discussion on signal enhancement mechanisms for Raman and PL based on the experimental data obtained.

5.1 Near-field Raman scattering in SWNTs

Typical experiments start with confocal imaging of nanotubes in a large scanning range, e.g. $20\mu\text{m}\times 20\mu\text{m}$, providing an overview of the nanotube distribution on the substrate. Figure 27 shows the confocal Raman scattering (a) and PL (b) images of DNA-wrapped HiPCO nanotubes prepared on the glass cover slide, respectively. The excitation source is HeNe laser at 632.8 nm. The two images are recorded by two APDs, one following a bandpass filter at 700nm allowing

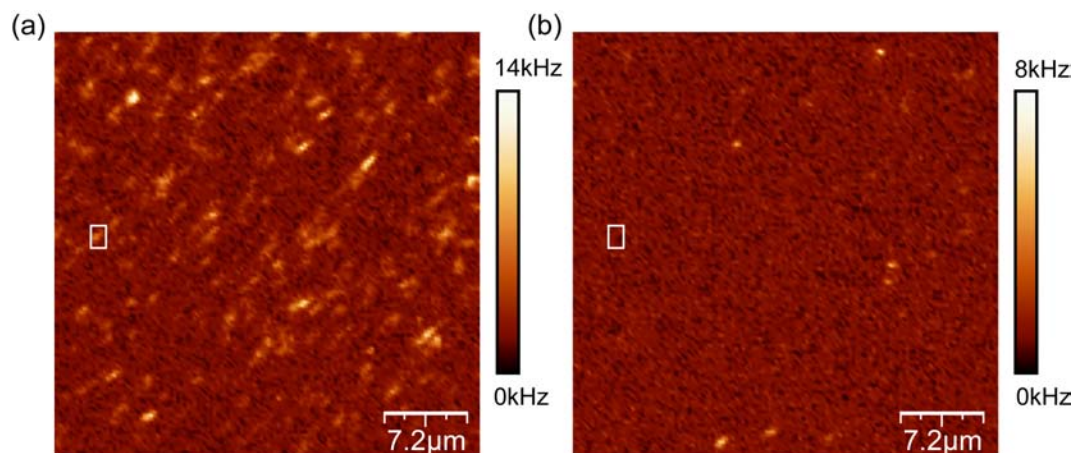


Figure 27: Confocal images of DNA-wrapped HiPCO nanotubes on glass. (a) Raman scattering image representing the integrated G-band intensity of nanotubes, a characteristic feature of all nanotubes. (b) PL image representing the integrated PL intensity at 950 nm from few nanotube species [27]. Laser excitation at 632.8nm, $50\mu\text{W}$ power. Because of the broad chirality distribution of the HiPCO nanotubes, we can see only a small amount of the nanotubes emitting at about 950 nm in (b).

the G-band signal of nanotubes to be transmitted, the other following a bandpass filter at 950 nm with 50 nm width allowing PL signals from a limited number of nanotube species to be transmitted (see section 2.4, 2.5, 4.1). The Raman scattering image visualizes all the nanotubes on the substrate since the G-band results from C=C stretching vibrations present in every nanotube. The signal amplitude is determined by the electronic resonances between laser excitation energy and electronic states of the nanotube. Figure 27(a) reveals a highly concentrated sample area with most of the nanotubes orientated in the same direction caused by the spin-coating. Figure 27(b) however gives few bright spots presumably from (8,3) nanotubes with an emission maximum at 952 nm [27] and a diameter of ≈ 0.8 nm. The wide chirality distribution of HiPCO nanotubes sample, with diameters ranging from 0.8 to 1.4 nm [159], determines that the number of nanotubes observed in the limited spectral window used here is very small.

Following the confocal imaging characterization, the gold tip is approached and scanned over the stationary sample at distances down to 2 nm from the surface using shear-force feedback control. By applying voltages on both x and y piezo using RHK equipment, the gold tip can be moved above the surface and finally centered approximately in the laser focus, as can see in the

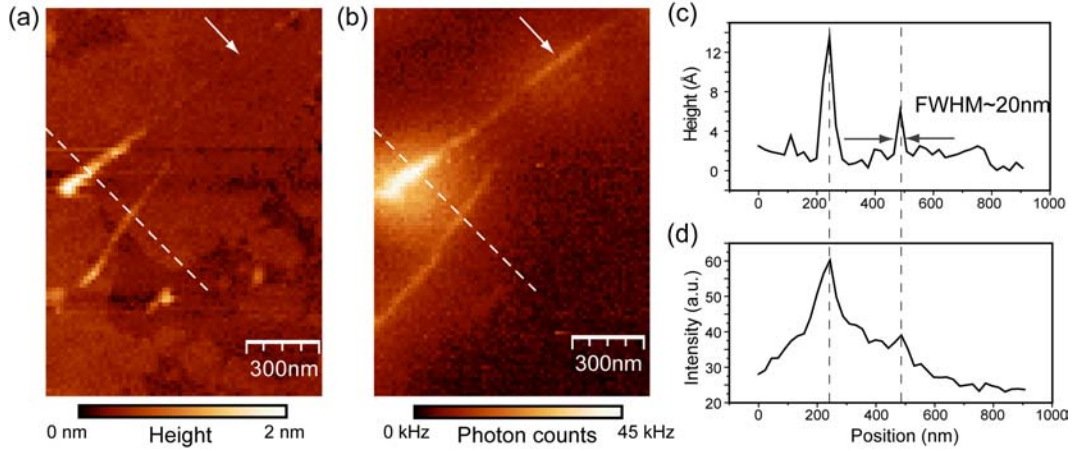


Figure 28: Simultaneously obtained topography (a) and near-field Raman scattering (b) images taken in the area marked by the white rectangle in Figure 27. No PL was observed from the nanotubes. The Raman scattering image is detected by integrating the G-band signal around 700 nm upon laser excitation at 632.8 nm. (c) and (d) are cross sections taken along the white dashed lines in (a) and (b), respectively. The upper nanotube appears non-uniform in height and the end of it is more likely to be a bundle distinguished from the height in (c). The lower structure nanotube is an individual nanotube according to the small and rather uniform height. In the Raman cross section (d), there is also a contribution from far-field signals.

insert of Figure 21. More precise adjustment of the tip position can be achieved by maximizing the background signal since it mainly comes from the luminescence signal from the gold tip. In the ideal case, once the tip axis is overlapped with the z-component of the laser focus, a near-field signal can be detected. While in the real experiments, the achievement of a near-field signal depends largely on the tip geometry and the sample quality. The scan speed must be moderate to avoid crashing the gold tip due to the slow response time of the tuning fork (see section 4.1).

Figure 28 shows an example of a near-field Raman image (b) of two DNA-wrapped HiPCO nanotubes taken in the area marked by the white rectangle in Figure 27, representing the intensity of integrated G-band signal around 700 nm upon laser excitation at 632.8 nm. The topography image is formed by shear-force detection (see section 4.1). Figure 28(c) and (d) are cross sections taken along the white dashed lines in (a) and (b), respectively. The resolution can be determined by the full width at half maximum (FWHM) as indicated in (c), being ≈ 20 nm. The upper nanotube in topography appears non-uniform with a thicker end at which the

corresponding Raman intensity is stronger. This indicates that the nanotube is more likely to be a bundle since there are no nanotubes with diameter 1.4 nm in resonance with the excitation energy of 632.8 nm corresponding to 1.96 eV (see in Figure 6). Besides the two nanotubes, the topography image also reveals two-dimensional features with a step height of about 3 Å as would be expected for a single layer of surfactant [21]. The presence of a surfactant layer however can affect the tip-sample distance and hence the signal enhancement. The nanotube segment marked by white arrows can hardly be distinguished in topography, while the Raman signal is stronger than for adjacent parts. In both Raman image (b) and its corresponding cross section (d), there is also contribution from the far-field signals varying on a length scale of about 300 nm.

5.2 Near-field PL in SWNTs

Photoluminescence has been used for studying the electronic properties of nanotubes since about 6 years. The PL energy is determined by the renormalized band gap and exciton binding energy and is sensitive to the environment. In 1D structures, the exciton diffusional range is confined and has been reported to be ≈ 100 nm along the nanotube axis [82, 83] (see section 2.5). The exciton diffusional range is a relevant length scale for studies on PL energies and dynamics of excitonic states in nanotubes [29, 160, 161], and PL quenching at specific locations along the nanotube [86, 87]. Near-field PL microscopy provides high spatial resolution tracking excitons within/far below their diffusional length.

5.2.1 PL imaging and spectroscopy

A long-held belief was the direct-grown nanotubes do not emit because the aggregation perturbs the electronic structure of nanotubes. Till in 2002, O'Connell et al. first observed the PL from micelles-encapsulate individual nanotubes in aqueous solution [21]. The observation of PL from single nanotubes proved that the emission is also possible for nanotubes prepared on glass substrate, although the fluctuations in the local environment such as electrostatic surface potential changes [162] or localized charges [163] can significantly perturb the PL of nanotubes [28].

Stable PL can be achieved more easily from DNA-wrapped nanotubes prepared on mica layers than from bare nanotubes on the glass substrate [83]. Figure 29 displays simultaneous topography and near-field PL from the DNA-wrapped CoMoCAT nanotubes on mica substrate. Several

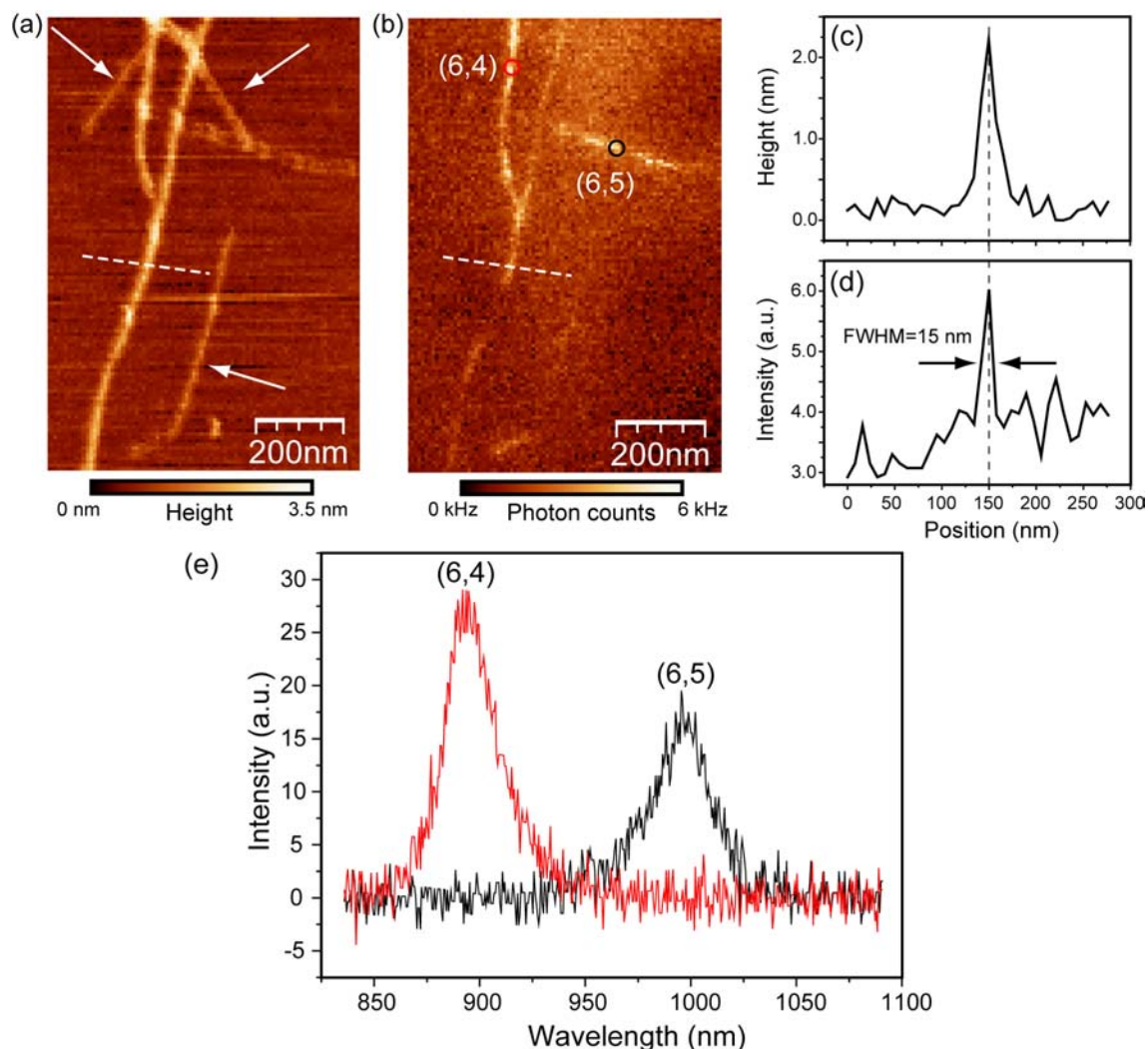


Figure 29: Simultaneously obtained topography (a) and near-field PL (b) images. The laser excitation is HeNe laser at 632.8 nm. The PL image is detected by integrating the intensity above 860 nm and below the up limit of the detector (≈ 1050 nm) using a long pass filter at 860 nm. (c) and (d) are cross sections taken along the white dashed lines in (a) and (b), respectively. The FWHM in (d) indicates an optical resolution of 15 nm. (e) Near-field PL spectra taken at the positions marked with circles in (b). The spectrum in red is from the red circle giving the emission energy at about 890 nm from (6,4) nanotubes. The spectrum in black is from the black circle giving the emission energy at about 1000 nm from (6,5) nanotubes.

nanotubes arranged randomly on the substrate as can be seen from the topography image (Figure 29(a)). The PL image is detected by integrating the intensity above 860 nm and below the upper limit of the detector (≈ 1050 nm) using a long pass filter at 860 nm. The PL signals extend from 100 nm to few hundreds of nanometers appearing as non-continuous PL segments with variable intensities. Nanotubes pointed by white arrows in (a) give no PL signals in (b), indicating either metallic character or emission energies beyond the detection window. The cross sections (c) and (d) are taken along the white dashed lines in (a) and (b), respectively. The FWHM in (d) indicates an optical resolution of 15 nm. PL energy of nanotubes is structure selective (see section 2.5) and near-field PL spectra can therefore be used to assign nanotube chiralities on the nanometer scale. Figure 29(e) shows near-field PL spectra taken at the two positions marked with circles in (b). The spectrum in red is from the red circle giving the emission energy of about 890 nm from (6,4) nanotubes. The spectrum in black is from the black circle giving the emission energy of about 1000 nm from (6,5) nanotubes. The red-shift compared to the 873 nm emission energy reported for the (6,4) nanotube and the 975 nm for (6,5) [27] results from DNA-wrapping [164] (see also section 6).

5.2.2 PL energy variation along the nanotubes

As introduced in section 2.5, the influence of the environment can renormalize the band gap energy through electron-electron interaction E_{e-e} and determines the exciton binding energy E_{bind} resulting from electron-hole interactions, thus significantly modifying the emission energy [76–80]. Here I show that near-field PL imaging provides a direct vision of PL from nanotubes and the intensity variations on the nanometer scale. Near-field PL spectroscopy offers information of exciton energies from the nanotubes within the confined detection volume.

Figure 30 shows simultaneously acquired topography (a) and near-field PL (b) images of SWNTs encapsulated with sodium dodecyl sulfate (SDS) on mica. In the present case, the PL occurs at the middle part of the nanotube and is extended over about 400 nm. Several localized bright spots along the extended PL are attributed to the non-uniform SDS coverage, evidenced in the topography image. The flakes in the background of the topography image with a height of about 1.4 nm are expected for a single layer of SDS surfactant. (c) and (d) are cross sections taken along the dashed line in (a) and (b), respectively. The height of the nanotube measured at the dashed line is about 3.5 nm. Based on the topographic data, it is not possible to distinguish between a single SDS-wrapped nanotube and a thin bundle.

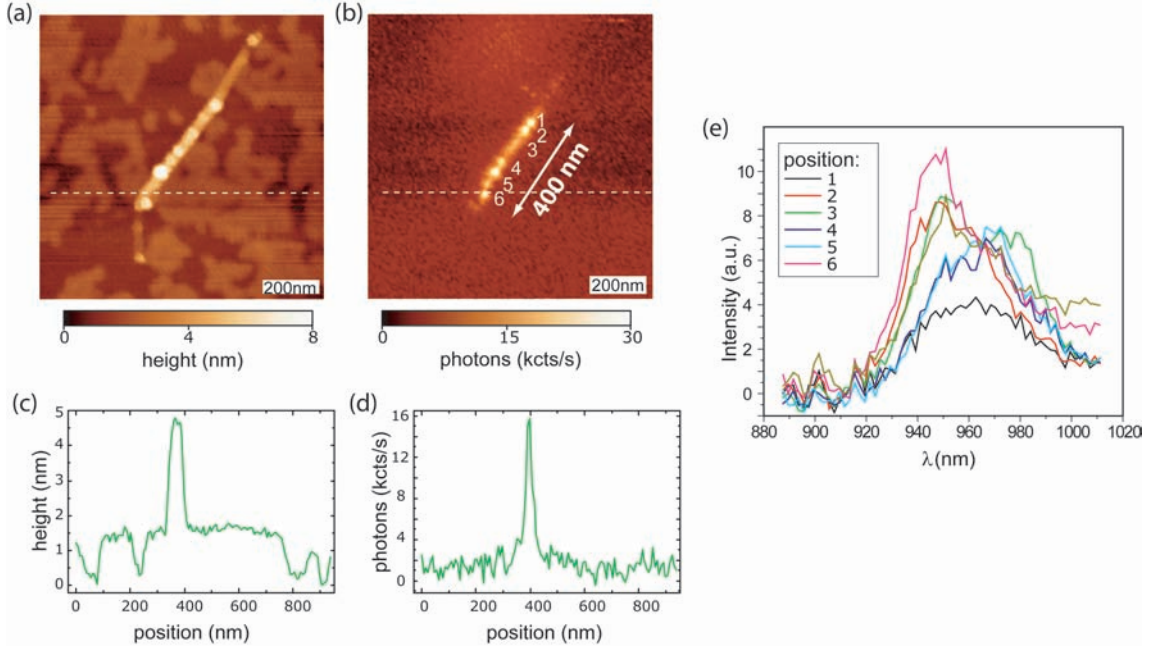


Figure 30: Simultaneously acquired topography (a) and near-field PL (b) images of SWNTs encapsulated with SDS on mica. The PL image represents the integrated intensity over the emission peak using a bandpass filter centered around 950 nm. (c) and (d) are cross sections taken along the dashed line in (a) and (b), respectively. (e) Near-field spectra taken at 6 positions along the nanotube marked with number 1 to 6 in the PL image. Emission energies variation within the small length range visualizes the excitonic energies variation along the nanotube.

Non-uniform PL energies along a single nanotube at a length scale of 30 nm has been first reported in one of our publications [165]. In this paper, near-field photoluminescence spectra detected by probing at 6 different positions along the nanotube with 30 nm steps, shown in Figure 30(e), reveal a significant variation of the emission energy ranging from ≈ 950 nm to ≈ 975 nm (corresponding to 33 meV). Such variation occurring on a 30 nm length scale reflects the local variation of excitonic energies. Both E_{e-e} and E_{bind} are modulated by an increasing dielectric constant ϵ (see section 2.5). This is supported by inspection of the topographic image shown in Figure 30(a), the nanotube is covered by uneven SDS surfactant appearing spots like features in the topography. In standard confocal microscopy, only a spatial average could be observed leading to a broadened emission band in the spectrum.

A regular variation of emission energies was observed from DNA-wrapped nanotubes. DNA-

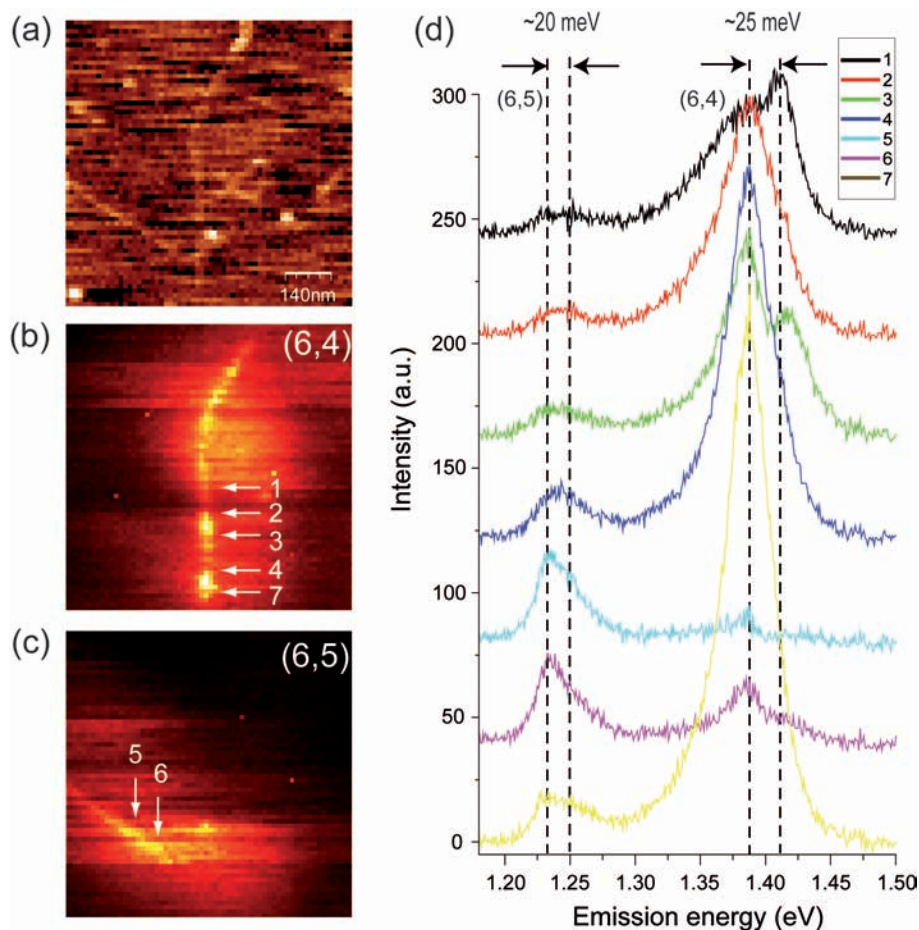


Figure 31: Simultaneously recorded topography (a) and near-field PL images (b, c) of two DNA-wrapped CoMoCAT nanotubes on mica. The PL images were obtained by measuring spectra at each pixel and represent the integrated intensity between 1.202 eV and 1.254 eV covering the emission range of (6,5) nanotube for (b), and between 1.345 eV and 1.432 eV covering the emission range of (6,4) nanotube for (c). The exposure time for each spectrum is 40 ms. Spectra taken with longer exposure time (1 s) at different positions along the two nanotubes are shown in (d), marked with numbers 1 to 7. Both nanotubes show two emission energies, the lower energy peak is induced by DNA-wrapping. The redshift of emission energy caused by DNA is 20 meV for the (6,5) nanotube, and 25 meV for the (6,4) nanotube. There are contributions of far-field signals in the near-field spectra of both nanotubes.

wrapping redshifts the PL energy depending on the nanotube chirality by several tens of meV compared to the values reported for micelle encapsulated nanotubes in aqueous solution [27, 97, 100, 101], which can be attributed to an increasing ε [80]. Figure 31 presents the near-field PL of DNA-wrapped CoMoCAT nanotubes. The topography (a) shows several thin nanotubes in the scanned area indicating well isolated individual nanotubes. Near-field PL images were obtained by acquiring a spectrum at each pixel during scanning and then converting spectra into images by integrating intensities in selected spectral windows. Figure 31 represents the integrated intensity between 1.202 eV and 1.254 eV covering the emission range of (6,5) nanotube for (b), and between 1.345 eV and 1.432 eV covering the emission range of (6,4) nanotube for (c). The PL is more extended along the nanotube except the two bright and intense spots at the end of the (6,4) nanotube. In both images, there are strong far-field contributions seen as slowly varying background in Figure 31. Spectra taken at different positions along the two nanotubes are displayed in Figure 31(d). Emission peaks from both nanotubes consist of a higher energy peak and a lower energy peak marked by the black dashed lines. The lower emission energy is attributed to DNA-wrapping [27, 100, 101]. The different degrees of redshift from (6,5) and (6,4) nanotubes is in agreement with the reported diameter dependent emission energy shift [80]. We can also see the far-field contributions in spectra, e.g. in the spectra 1-4 and 7 from (6,4) nanotube, one can see emission bands from (6,5) nanotube. A detailed investigation of the local optical response of carbon nanotubes is presented in section 6.

5.2.3 Highly localized PL in SWNTs

Near-field PL images, such as the presented Figure 29, Figure 30 and Figure 31, reveal extended PL and also localized PL signals along the nanotubes, e.g. some bright PL parts in Figure 29(b), bright spots like PL along the nanotube in Figure 30(b) and the two bright and intense spots at the end of the (6,4) nanotube in Figure 31(b). The photoluminescence signal along a single nanotube can have variable length of extension as illustrated in Figure 32. Dots like PL with even spacing has been observed as shown in Figure 33. Figure 33(a) and (c) are two topography images of DNA-wrapped CoMoCAT nanotubes on mica. The nanotubes are all individual ones determined from the topographic height (not shown). The resolution in the current measurement is not high enough to resolve the DNA segments. Figure 33(b) and (d) are corresponding near-field PL images with the image contrast provided by spectrally integrating over the photoluminescence peak centered at 950 nm. Regularly localized PL patterns with distances about 50 nm (Figure 33(b)) and 60 nm (Figure 33(d)) are observed. Although excitons could travel



Figure 32: Illustration of PL along the nanotube with different extension. (a) Extended PL along the nanotube. (b) Localized PL along the nanotube. (c) Localized PL with regular spacing along the nanotube.

along the nanotube and emission would result from the position associated with DNA-wrapped segments that have lower emission energy [22], both length scales between PL patterns are far too large compared with the length of DNA segments (section 2.6). Moreover, the short nanotube appearing on the upper right in Figure 33(b) and (d), which is from the same sample, shows clearly sequent PL without interruption.

The localized PL along the nanotubes appeared in most near-field PL images arises the question about the origin of localized PL. The dots like PL along nanotubes presented in Figure 33. unfortunately, are not enough to extract the origin of the equally spaced localization. Dekker et al. observed the similar potential patterns with even spacing of about 40 nm along the nanotube connected to two electrodes and gated with an AFM tip [166]. They attribute the patterns to localized charges near the nanotube, and mechanical deformations. Long range disorder of up to 100 nm due to, e.g., localized charges near the tube, intrinsic [167,168] or induced [167] defects, breaks the semiconducting tube into a series of quantum dots with large barriers [163], can also help to understand the observed dots like PL in Figure 33. The charges can come from the substrate surface or the metal tip that has been charged after a long time scanning. To examine whether there are quantum dots formed in nanotubes caused by local charging, we need to apply voltages on the nanotube, which is not done yet by far. Besides optical visualization of the localized excited states, femtosecond excitation correlation spectroscopy on nanotubes also revealed localized excitons determined by changing of PL lifetime with increasing temperatures that thermally drive the localized excitons into free exciton states [169].

In general, the observed localized PL reveals localized excited state along the nanotubes. The excited states relaxation in nanotubes is dominated by very efficient non-radiative decay channels. Trapping of excitons at impurity sites or at structural defects as well as coupling or branching to optically inactive excitons are discussed as competing processes to radiative relaxation [22–24, 165, 170, 171]. These localized perturbations can be expected to limit the spatial extent of delocalized excitonic states along the nanotube resulting in the low luminescence ef-

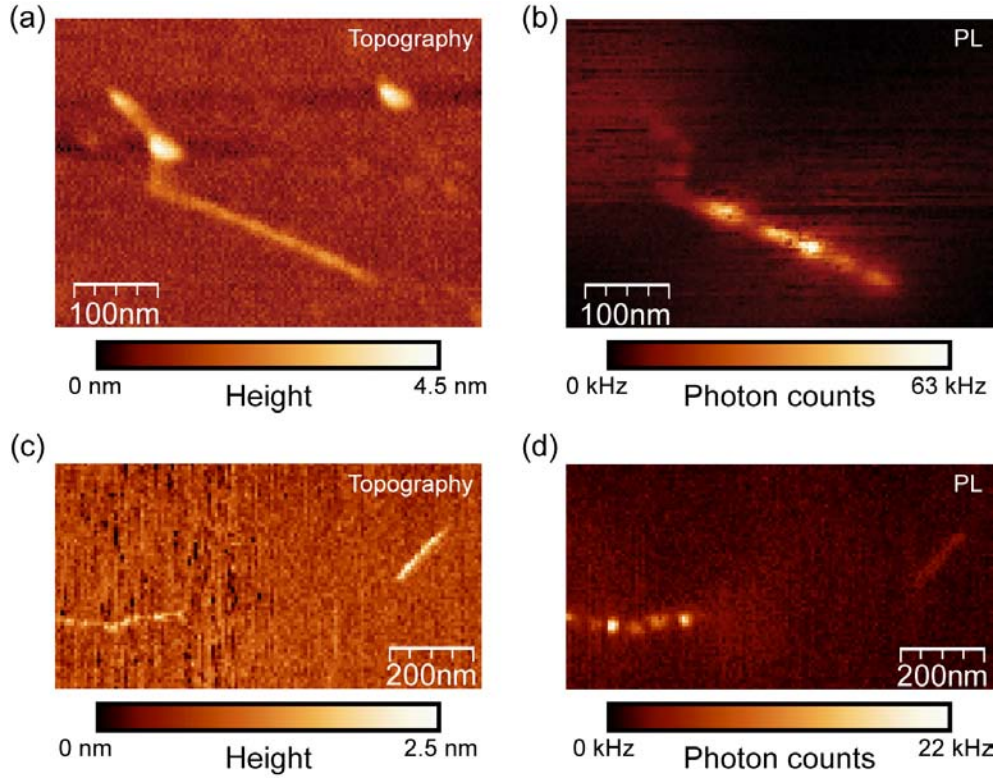


Figure 33: Two examples for localized PL along single nanotubes. Topography of DNA-wrapped nanotubes on mica (a,c) and the corresponding near-field PL images (b,d). Regularly localized PL patterns with distance about 50nm (b) and 60 nm (d) are observed. While the nanotube on the upper right of (d) shows continuous PL.

efficiency of nanotube and localize PL. Time-resolved fluorescence measurements of nanotubes reveal that the presence of free electrons or holes in nanotubes, arising, for example, from impurities or electric fields, may induce rapid annihilation of excitons through the Auger process strongly affecting the PL efficiency [172, 173]. High PL yields are from suspended nanotubes directly grown between two trenches which is supposed to have few defects caused in general harsh sample preparations for example, dissolving in solution, sonicating and so on [174]. In Raman scattering, defects usually break the selection rules, so that broadening and new peaks can usually be observed as reported for G' band in [158, 175]. The role of defects playing on photoluminescence however is very complicated since PL has been observed to be localized at defect sites along the SWNT [158], but also to be quenched towards the end of nanotube where is structural defect area [86, 87] (will be presented in section 8).

5.3 Simultaneous Raman scattering and PL of single SWNTs

Based on section 5.1 and section 5.2, I demonstrate now that simultaneously obtained near-field Raman scattering and PL signals from nanotubes can be used to study the correlation between phonon properties and electronic properties of nanotubes. Figure 34 shows simultaneously acquired near-field Raman (b) and photoluminescence (c) images of DNA-wrapped nanotubes on glass. The same laser excitation was used. The Raman image was detected by integrating the G-band intensity using a bandpass filter centered at 700 nm. The photoluminescence (PL) signal represents the intensity around 950 nm detected by using a bandpass filter centered at 950 nm. The topography (a) of the same sample area was detected simultaneously. Figure 34(d), (e) and (f) are zoom in images in the area marked with white rectangles in (a), (b) and (c). Figure 34(g), (h) and (i) show topographic and optical cross sections taken along the dashed lines in (a), (b) and (c), respectively. The optical resolution is about 14 nm as indicated in the PL image, which is far below the diffraction limit. In the topographic image (a), a nanotube can be seen to extend from the upper left to the lower right. The measured height in the cross section along the dashed line is about 2.5 nm. This is in agreement with the expected height of a single DNA-wrapped nanotube [95, 160, 161]. In both topography (a) and (d) images we can see the roughness of the glass cover slide, being about 5 Å. The patterns formed by surfactant as seen in Figure 28(a) fortunately do not exist in this sample area. The surfactant-free area gives the possibility to observe DNA-segments, as shown in Figure 14(b).

The Raman signal occurs along the nanotube, but disappears before the nanotube ends as determined from the topography image. The PL signal, on the other hand, is localized within about 90 nm and occurs just where the Raman signal ends. This observation can be explained by a change in chirality (n,m) along the nanotube. In the upper section, the nanotube's electronic states, given by (n,m), are in resonance with the laser energy leading to resonance Raman scattering. Here, the nanotube is either metallic, i.e. non-luminescent, or the emission energy is beyond the detection window of 950 ± 20 nm. The nanotube chirality (n,m) in the lower section is associated with weaker resonance Raman enhancement while non-resonant excitation leads to PL at about 950 nm. Structural transitions along individual nanotubes have been reported before based on Raman data [30, 176]. PL has been observed at the defects rich position along the nanotubes and attributed to local doping identified by the change of G' band shape [158]. The D-band intensity along the present nanotube however reflect the low D-band intensity at the end of the nanotube, where the near-field PL occurs, as shown in Figure 35. The absence of PL in the upper part can also be explained by the quenching effects due to the presence of

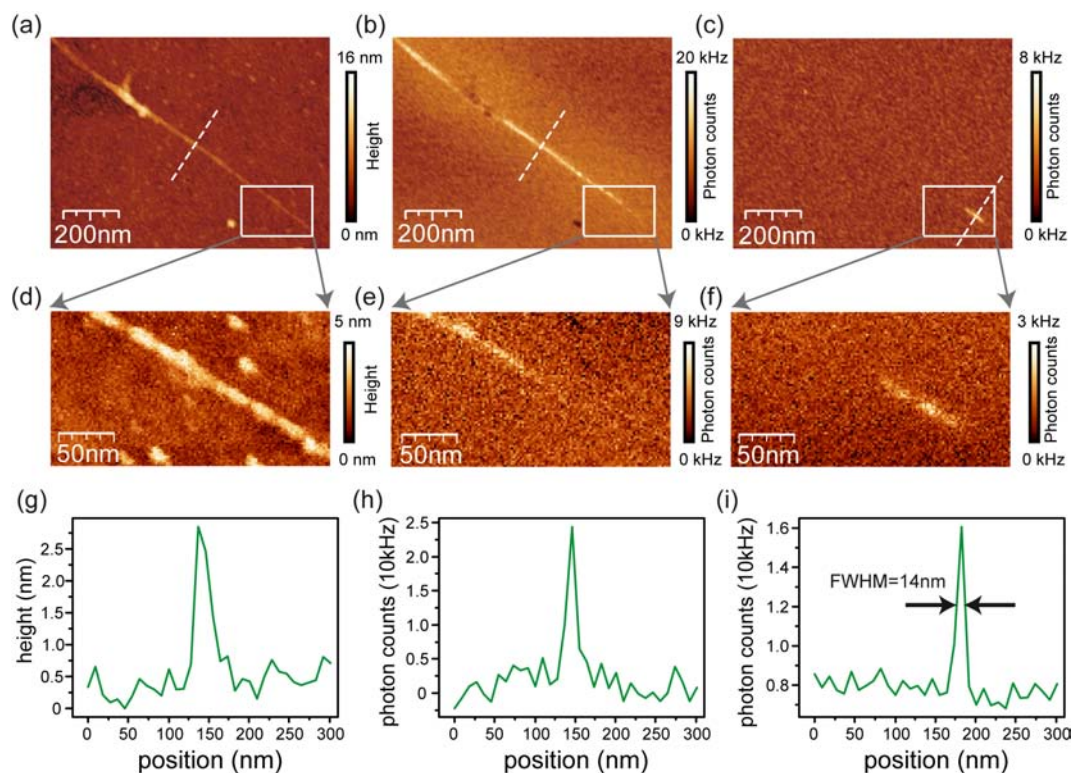


Figure 34: Simultaneously acquired topography (a), near-field Raman (b) and photoluminescence (c) images of DNA-wrapped nanotubes spin-coated on glass. (d), (e) and (f) are zoom in images corresponding to the areas marked with white rectangles in (a), (b) and (c), respectively. (g), (h) and (i) show topographical and optical cross sections taken along the dashed lines in (a), (b) and (c). The optical resolution is 14nm indicated by the cross section through the PL signal which is only determined by the diameter of the gold tip. The PL signal starts where the Raman signal ends indicating a possible intramolecular junction along the nanotube.

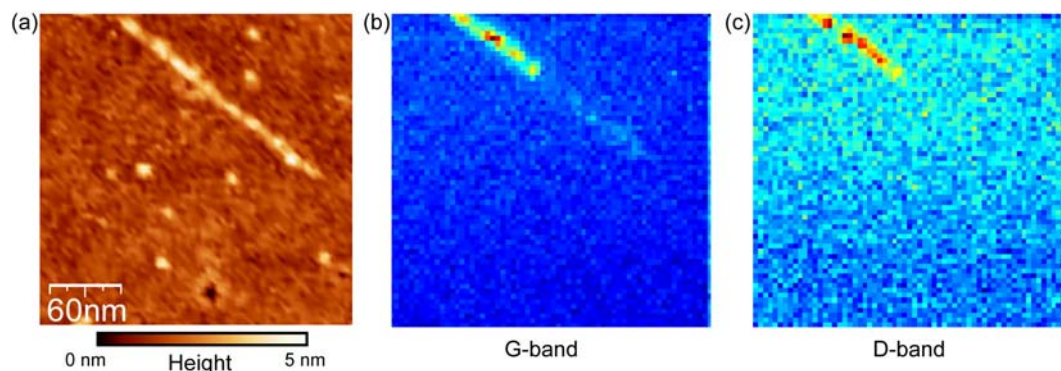


Figure 35: Simultaneous topography (a), near-field Raman G-band (b) and D-band (c) images of the same nanotube as in Figure 34. The G-band and D-band images are obtained by acquiring a spectrum at each pixel and integrating the intensity around 700 nm and 690 nm, respectively.

defects, similar discussion is presented in section 8.

It is notable that besides the signals from the nanotube, there are several big features appearing in the topography giving negative signals in the Raman image, e.g. the dark spot in the lower part of the Raman image (b) located next to the white rectangle is induced by the large particle that can be seen in the topography with a height of 14 nm. In near-field optical microscopy, the background signal results mainly from gold tip luminescence. At the position of the dark spot, the particle reduces the laser excitation of the gold tip and therefore reduces the luminescence from the gold, leading to a hole in the background signal [154]. Moreover, when the gold tip meets such big particle with 14 nm height, the feedback control will retract the tip 14 nm off the surface, which will also reduce the detectable luminescence from the gold tip. This negative effect can also compete with the near-field signal. As an example, the big particle stuck on the nanotube on the upper left part, significantly reduces the signal enhancement by increasing the tip-sample distance. This is a well-known tip artifact in near-field Raman microscopy that can be avoided or at least reduced by the procedure described in the following paragraph [154].

Instead of imaging Raman and PL signals using bandpass filters centered at different spectral windows, spectroscopic imaging provides characterization of different bands simultaneously with spectral information at each pixel. The method has been used for both Figure 31 and Figure 35. An example for spectroscopic imaging is shown in Figure 36(a). Raman images of different Raman features and the PL image of emission around 940 nm are displayed. This method avoids the influence of overlapping bands by selecting specific spectral windows with narrow

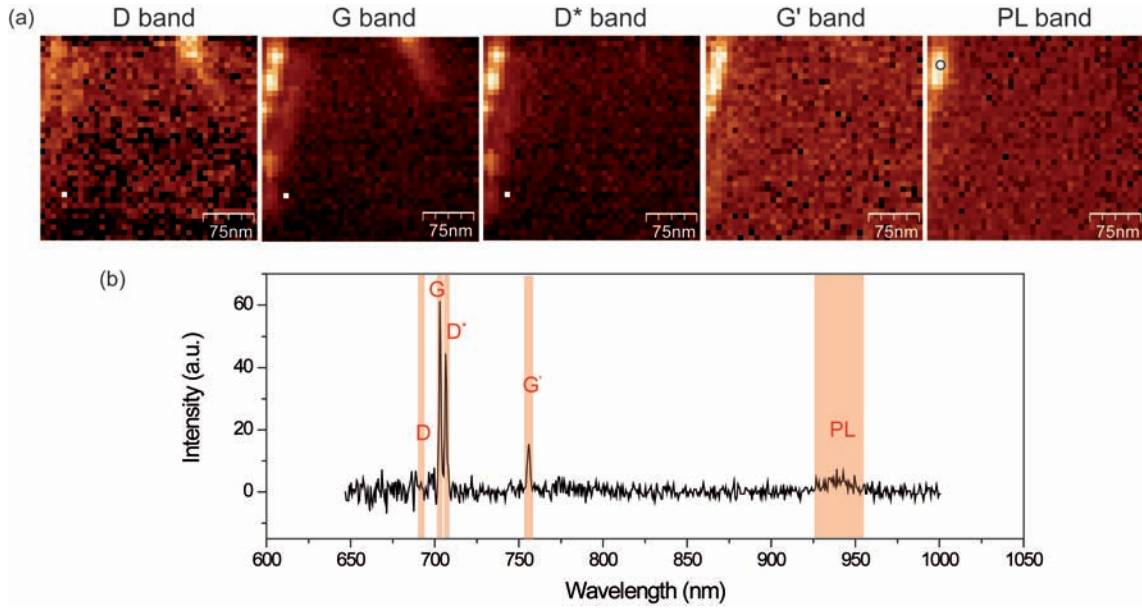


Figure 36: Raman images and PL image (a) obtained by integrating intensities at different spectral windows as shown in (b). Raman images showing the D-band (≈ 690 nm), G-band (≈ 703 nm), D*-band (≈ 706 nm) and G'-band (≈ 760 nm) intensities, the spectral positions marked are in (b). PL image is from emission band ≈ 940 nm, seen also in (b). Spectra are taken from each pixel during scanning. The spectral exposure time is 40 ms. The excitation power is $100 \mu\text{W}$. Spectrum (b) is taken from the pixel marked with the black circle in the PL image in (a).

band width. The G-band image gives three nanotubes in this area, two on the left and one on the upper right. The D-band image shows weak intensity, indicating the presence of defects in all three nanotubes. While the second-order G'-band does not scale with the D-band intensity image as it is not defect related (see section 2.4). However, the D*-band is missing from the nanotube on the upper right, as well as in the PL image. The intensity of the D*-band (1620 cm^{-1} to 1630 cm^{-1}) is also defect related [177]. Whether there is a correlation between D*-band and PL of nanotubes is still unclear. The missing PL from the upper right nanotube can also indicate a metallic nanotube.

Simultaneous Raman scattering and PL images reveal that both phonon modes and excitonic states are non-uniform along the nanotubes. The variation of Raman scattering signals are manifested by the varying intensity along the nanotube, can be attributed to the change of resonance or chiralities. While the non-uniform PL signals are appeared as either variable PL energies

or localized PL signals, evidenced by near-field PL spectroscopy. The variations of PL energy results from inhomogeneous dielectric environments (see section 2.5). Changes of the dielectric constant of the surrounding media have been reported to shift the emission energy by several tens of meV [27, 97, 100, 101]. Transitions in DNA conformation, for example, lead to shifts of up to 25 meV for DNA-wrapped nanotubes. From the topographic measurement, it is clear that the wrapping by DNA (or SDS) is uniform along the nanotubes for our samples. Considerable fluctuations of the dielectric constant can be expected. How nanotubes respond locally to the DNA-wrapping has high potential in nanoscale sensing applications, will be discussed in details in section 6. PL localization could result from chirality variations along the nanotube leading to luminescent and non-luminescent sections as discussed in Figure 34. Furthermore, defect related non-luminescent trap states can quench the emissive state. As nanotubes have surface atoms only, PL appears more sensitive to both intrinsic and extrinsic factors.

5.4 Signal enhancement: Comparison for Raman scattering and PL

In the previous section, simultaneous near-field Raman scattering and PL are achieved for the first time, offering detailed information on the optical properties of nanotubes with high spatial resolution that conventional microscopy can not reach. We now have the unique possibility to quantify the enhancement of Raman scattering and PL simultaneously. Since Raman scattering cross sections are far smaller than those of fluorescence for most systems including fluorescent molecules this is typically not possible in conventional microscopy. Different enhancement factors are expected for Raman scattering and PL because of their different enhancement mechanisms (see section 3.3). Theoretical calculations for a laser illuminated ($\lambda=800$ nm) gold tip with an end diameter of 10 nm have shown an intensity enhancement factor of roughly 3000 over the incident light [124]. The enhanced Raman scattering and PL signal detected in the real experiment largely depends on the tip geometry and the resulting field distribution, and is usually much smaller than the calculated enhancement factor. In the following, I will discuss the different enhancement mechanisms for Raman scattering and PL based on the experimental results. The enhanced field at the tip apex is dominated by the field with the polarization parallel to the tip axis. How Raman and PL signals with the transition dipole along the nanotube axis are enhanced, will also be discussed in this part. PL quenching caused by the presence of metal tip at small tip-sample distance is inevitable and needs to be considered in the near-field PL measurements in order to find an optimum distance for PL enhancement.

Figure 37 displays two examples of near-field Raman scattering and PL images. Distinguished

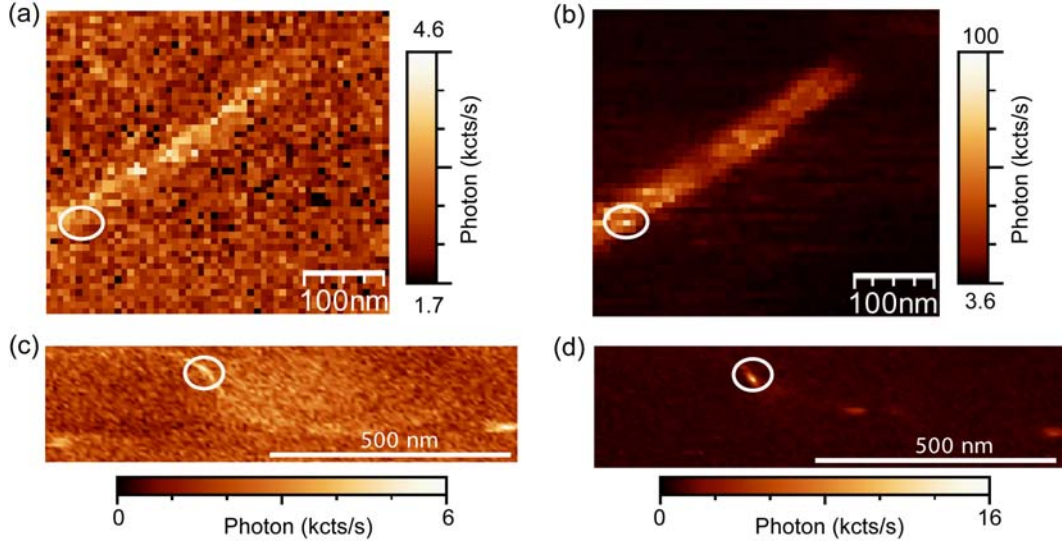


Figure 37: Near-field Raman scattering (a,c) and PL (b,d) images of two nanotubes. Both near-field PL images show higher image contrast. The signal enhancement is calculated by dividing the total signal including the near-field signal and the far-field signal by the far-field signal. The experimental signal enhancements for Raman scattering and PL are estimated at the positions marked with white ellipses. They are 2.3, 25, 3 and 85 for (a) to (d), respectively, indicating a higher signal enhancement for PL than for Raman scattering.

from the image contrast directly, the near-field PL signal seems to be stronger than the near-field Raman signal. The enhancement factor in the experiments is calculated by dividing the total signals detected including near-field optical signal and far-field signal by the far-field signal taking the probed surface area into account. For example, the optical resolution in Figure 37(a,b) is 35 nm, giving a surface area of $\pi(35nm)^2$, whereas the confocal focus area is $\pi(300nm)^2$ (see section 3.1.2) resulting in an area ratio of ≈ 75 . The near-field Raman signal marked with white ellipse in Figure 37(a) has a measured intensity of 3.1 kcounts/s (3100 photons per second detected), the far-field signal is 2.3 kcounts/s. Therefore, the enhancement factor is $(2.3+3.1)/2.3*75$ to be about 170. The same estimation can be used for PL enhancement at the same position on the nanotube, which is calculated in the way as $(100+4.22)/4.22*75=1875$. The enhancement factors are estimated for the nanotube shown in Figure 37(c) and (d), where the surface area ratio is calculated to be 225. The enhancement factor of Raman scattering is $(4.0+2.0)/2.0*225=675$, while that of PL is $(17.0+0.2)/0.2=19125$.

Learned from section 3.3, the Raman scattering signal is increased by an enhancement of both

the incident field and the scattered field. The PL intensity, on the other hand, depends on the excitation rate and the radiative rate of SWNTs. Both rates can be increased by the metal tip acting as an antenna for radiation [140, 148, 165]. From experimental results in Figure 37 it is evident that the signal enhancement of PL is stronger than that of Raman scattering. Assuming the nanotubes are excited far from saturation and ignoring any vectorial field projections on the transition dipole axis, equation 42 indicates that $M_{PL} > M_R$ is only possible if $Q_{PL}/Q_{PL,0} \geq 1$ (Q is defined in equation 22). In other words, the presence of the metal tip leads to a considerable increase of the quantum yield Q . Because the quantum yield cannot be larger than unity, $M_{PL} > M_R$ requires an unperturbed (intrinsic, in the absence of the tip) quantum yield that is very small, i.e., $Q_{PL,0} \leq 1$. In the near-field measurement both radiative rate and non-radiative rate are affected by the presence of the tip: k_r is modified by the enhanced fields at the nanotubes location (Purcell effect) and k_{nr} is increased by non-radiative decay channels result from by energy dissipation inside the metal tip [143, 146]. Consequently, a strong enhancement of the PL rate requires a considerable increase of the radiative rate k_r due to the presence of the metal tip. Our results show for the first time that the very low quantum yield of nanotubes [21, 23] can be significantly increased by increasing the radiative rate k_r . Such enhancement is not possible for systems with a quantum yield close to 1, such as fluorescent dyes or quantum dots.

The simple model discussed so far does not take into account the complex field distribution at the tip involving different polarization directions, which has been visualized by fluorescence of single molecules [178]. How will it be for SWNTs? In the near-field measurements, the gold tips used normally have diameters larger than 10 nm and can be considered as a slight curved metal surface positioned on top of nanotubes having a diameter around 1 nm. In the probed area underneath the tip apex, the electric field is radially symmetric consisting of fields polarized along the tip axis and fields with polarization deviating from the tip axis as shown in Figure 38(a). After decomposing the enhanced field contains both parallel and perpendicular polarized components to the nanotubes axis. The enhanced Raman scattering and PL signals from nanotubes with the presence of a gold tip therefore could originate from different field components as discussed in the following.

The perpendicular polarized field can promote the cross polarized transitions in nanotubes as introduced in section 2.2. Both theoretical calculations and experimental results reveal a large blue shift of cross-polarized excitation energies E_{12} in the range of 200-300 meV compared with the value of $(E_{11} + E_{22})/2$ in the single-particle model due to much smaller exciton binding energies [53, 179, 180]. Figure 38(b) is the 2D photoluminescence excitation (PLE) plot based

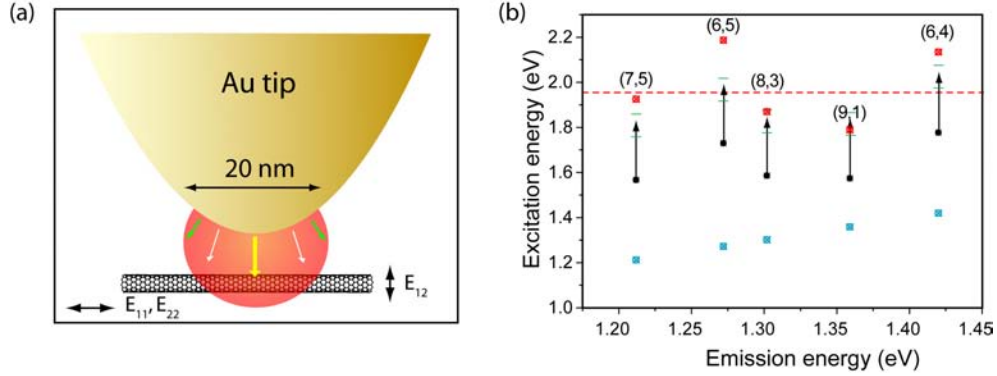


Figure 38: (a) Illustration of a gold tip with diameter of 20 nm positioned on top of a thin nanotube. The electric field underneath the tip consists of both parallel and perpendicular polarizations. E_{11} and E_{22} are parallel transitions, E_{12} is perpendicular transitions. (b) Photoluminescence excitation plot correlating emission and excitation energies. The red dashed line draws the HeNe laser energy. Red symbols denote E_{22} transitions and blue symbols mark E_{11} transitions. Taking 200-300 meV blueshift into account [53, 179, 180], the E_{12} transition energies are in the range between the two short green lines.

on the literature values in [27] for several nanotube species having lowest transition energies within our detector range (below 1050 nm). The red dashed line draws the excitation energy of the HeNe laser. Red symbols denote E_{22} transitions and blue symbols are E_{11} transitions. Taking into account the 200-300 meV blueshift, the E_{12} transition energies are in the range between two short green lines. Apparently, the excitation energy used in our experiment is in resonance with E_{22} of (7,5) nanotubes and E_{12} of (6,5) nanotubes. We come to the conclusion that the perpendicular polarized field along the gold tip axis can resonantly excite the sample in this work, which is chirality enriched with (6,5) nanotubes.

Since the Raman scattering and PL are distinct optical processes involving different electronic states, an explicit comparison of signal enhancement for Raman and PL can only be demonstrated considering both parallel and perpendicular polarizations. The parallel field comes from the transverse component of the laser focus and the parallel component of the enhanced field at the tip apex. As discussed in the previous part of this section, in case of the polarization along the nanotubes axis, the Raman signal is enhanced by both excitation and scattering enhancement, while PL signal is enhanced by the excitation field and the significantly increased quantum yield. In the case of perpendicular polarization, the strong excitation field along the tip axis only allows enhancement of the excitation from E_{12} transition. Since PL is from E_{11}

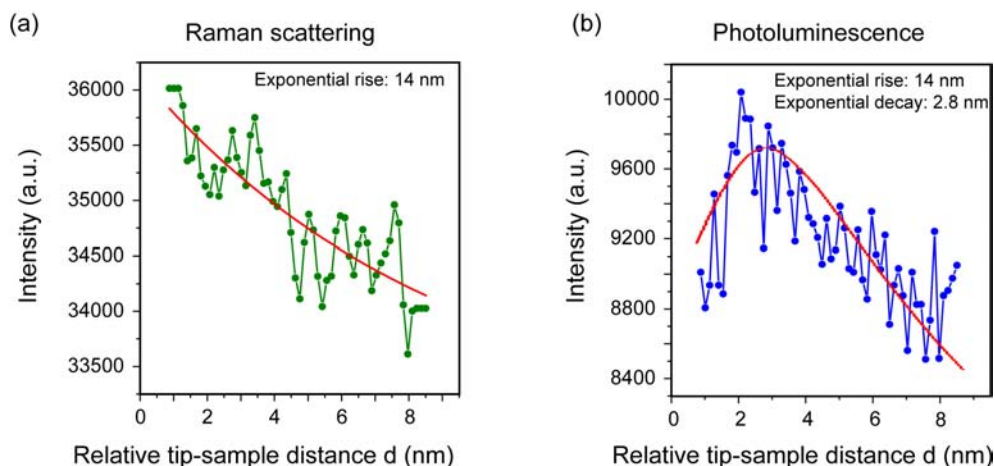


Figure 39: Simultaneously measured distance dependent enhancement for Raman (a) and PL (b), respectively. The intensity of Raman signal increases exponentially with decreasing of the tip-sample distance (green dotted line). The red curve in (a) is fit with exponential function with an exponential rise length about 14 nm. The intensity PL increasing with decreasing of the tip-sample distance first and then decreases as the tip-sample distance get further smaller (blue dotted line). The fitting curve (red curve) gives an exponential rise length about 14 nm and an exponential decay length about 2.8 nm.

relaxation, it can not be enhanced by this field. The enhancement of Raman scattering by the perpendicular field appears more complicated since there are different Raman modes involved. The Raman selection rules determine the observation of modes requiring the right polarization of both incident light and scattered light, e.g. $A(A_{1g})$ symmetry modes can be observed when both incident and scattered light are parallel to each other and $E(E_{1g})$ symmetry modes can be observed when the polarization of incident light is perpendicular to the polarization of scattered light [15]. From the overall Raman signals observed it is therefore difficult to evaluate the enhancement from the perpendicular polarized field. All in all, the enhanced optical response from the nanotubes results mainly from the enhanced excitation field, the observed stronger PL is attributed to the very low quantum yield of nanotubes that allows large-scale boosting.

Signal enhancement of both near-field Raman scattering and PL depend on the tip-sample distance. In near-field PL, energy transfer from the excited molecules to the metal tip followed by non-radiative energy dissipation eliminates the photoluminescence at small tip-sample distance [145–147, 181]. PL of single molecules close to spherical metal particles reveals a complex distance dependent interplay between competing enhancement and quenching pro-

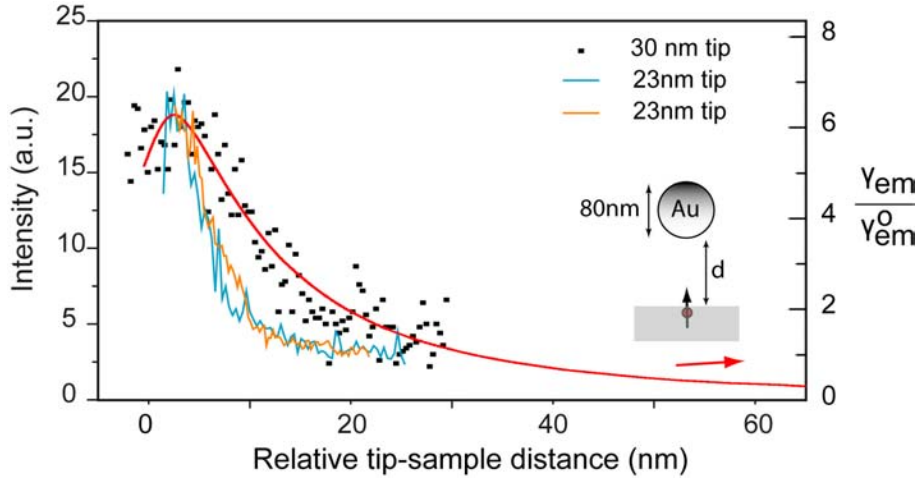


Figure 40: Distance dependent near-field PL measured with different gold tips and the calculated result using a 80 nm gold spherical particle and a dipole orientation perpendicular to the substrate. (red curve) [148]. The orange and blue curves are from different nanotubes using the same gold tip with diameter of 23 nm.

cesses [140, 148, 149]. The tip-sample distance dependent signal enhancement from nanotubes was observed to be different for Raman scattering and PL. Figure 39 presents simultaneously measured distance dependent enhancement for Raman (a) and PL (b), respectively. The intensity of the Raman signal increases exponentially with decreasing tip-sample distance exhibiting an exponential rise length about 14 nm. The intensity of photoluminescence however involves two processes, first enhancement with decreasing tip-sample distance and then quenching as the tip-sample distances get smaller. Both of the two processes can be fit with exponential functions, giving an exponential rise length about 14 nm and an exponential decay length about 2.8 nm. More examples of PL quenching at small tip-sample distances are shown also in Figure 40. Both enhancement and quenching effect caused by the metal tip lead to an intersection of the distance dependence curves. As a result, there exists a maximum of M_{PL} at a finite distance from the surface.

Besides the distance dependence, the influence of the tip size or the tip shape on field enhancement will also effect the signal enhancement at small interaction distance [127–131, 182]. Figure 40 shows the tip-sample distance dependent PL enhancement measured using different gold tips, including the calculated curve for an 80 nm spherical gold particle. The red curve is calculated using multiple multipole (MMP) method for the PL rate of Nile blue molecules with

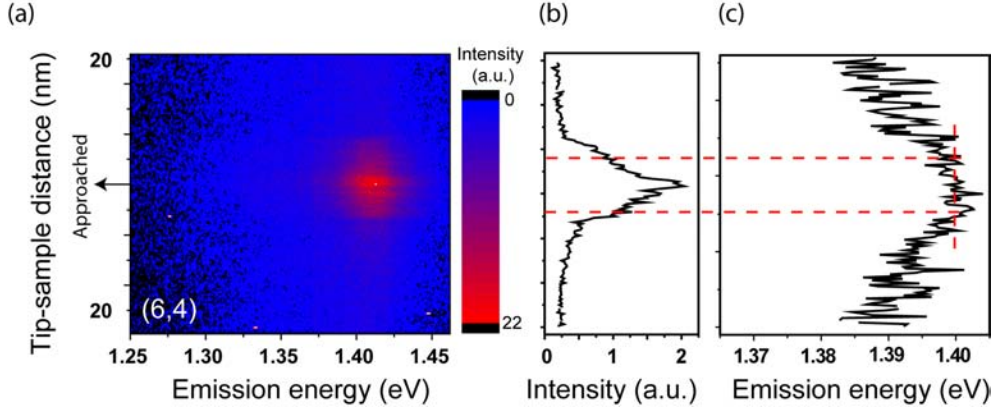


Figure 41: 2D photoluminescence maps taken at a fixed position from a single (6,4) nanotube (a) as a function of tip-sample distance measured during tip approach and retracting. The PL intensity is strongly enhanced at small tip-sample distance and reaches the maximum when the tip is approached marked by the arrows in (a), as shown in (b). The spectra are fit with single Lorentzian peak functions to determine the center emission energies at different tip-sample distances up to 20 nm and shown in (c). Within the near-field range, $\leq 5\text{nm}$ guided by the red dashed line, the emission energies are constant within the experimental precision ($\pm 2\text{meV}$).

the presence of a 80 nm gold spherical particle as a function of particle-sample distance [148]. The black dots are experimental data acquired with a gold tip having the end diameter of 30 nm. The dots match the theoretical curve using the gold spherical particle. Here we can not compare the field enhancement from the gold particle and the gold tip, since the PL signals are from different samples exhibiting quite disparate optical properties. The blue and orange curves are from the same gold tip but different nanotubes. They appear quite similar showing the same degree of exponential increase as the tip-sample distance gets smaller. The blue curve shows a remarkable decrease in the PL intensity as the distance get smaller than the highest PL point. This result is also in agreement with [147], that small cone angles in tip-shaped metal structure are expected to reduce energy dissipation as compared to spherical particles [147]. The photo-bleaching however makes the experiments more difficult in case of high excitation power applied for non-resonant nanotubes. More measurements are necessary for a detailed quantification, are also helpful for finding optimum tip size and tip-sample distance.

The section 5.2.2 discussed the near-field PL variations along the nanotubes that were attributed to both intrinsic and extrinsic properties. Since nanotubes are very close to the gold tip, and the gold tip could be charged, is the energy variations caused by the presence of metal tip?

To figure out this problem, PL spectra were acquired during tip approach and tip retract as shown in Figure 41. Figure 41(a) presents a 2D photoluminescence map composed by all spectra taken at a position from a single (6,4) nanotube (a) as a function of tip-sample distance measured during tip approach and retract. For tip-sample distances larger than 20 nm, the detected signal represents the confocal spectrum resulting from spatial averaging. When the tip is closer within 10 nm distance a strong signal enhancement occurs (Figure 41(b)) and the near-field spectrum resulting from the nanotube section directly underneath the tip is detected. Importantly, in the near-field regime within the last 5 nm, marked with red dashed lines in Figure 41(a), no spectral shift occurs within the precision of the measurement of about ± 2 meV. Moreover, there are no photo blinking or irreversible photo bleaching caused by metal tip in the present measurement. Hence, the presence of the metal tip that is held on the top of nanotubes with a constant distance of about 2 nm does not affect the emission energy variations.

In summary, near-field Raman scattering and PL using TENOM with high spatial resolution down to 15 nm has been presented in this section. Non-uniform phonon modes and excitonic states can be resolved along the nanotubes, providing insights of the intrinsic and extrinsic properties of nanotubes. Observation of PL energies from single nanotubes provides access to the properties of excitonic states in SWNTs with specific chirality (n,m). Both Raman scattering and PL signals are enhanced by the strongly enhanced electric field confined at the tip apex. The enhancement for PL signal is found to be stronger than for Raman scattering signal due to the low quantum yield of nanotubes. TENOM is ideally suited for studying on Raman scattering and systems with low quantum yield.

6 Local optical response of nanotubes to DNA-wrapping

This section is based on the paper "Visualizing the Local Optical Response of Semiconducting Carbon Nanotubes to DNA-wrapping" accepted for publication in Nano Letters.

High resolution PL imaging in section 5.2.2 revealed distinct fluctuations of the PL energies caused by structural defects of the nanotubes or inhomogeneous environments. At present, the influence of the environment is described by its relative dielectric constant ϵ influencing exciton binding energies but also renormalizing the band gap through charge carrier screening [76–80]. As a result, the emission energy of nanotubes is modulated by the dielectric constant, which can be expected to be non-uniform along nanotubes, leading to non-uniform emission energies in single nanotubes measurements [28, 32, 165]. Since nanotubes have potential as optical and electronic sensors [18, 19, 94], understanding of the local response to the environment is essential for applications in sensing schemes.

DNA-wrapped carbon nanotubes are also of great interesting in sorting nanotubes and building chemical sensors [18, 19, 33, 34]. Single-strand DNA-wrapping introduces DNA segments with finite length while the details of the secondary DNA structure will be determined by a complex interplay between π - π stacking interactions between DNA bases and the nanotube surface as well as electrostatic interactions of the phosphate backbone [93, 95, 183] (see also section 2.6). The effect of helical wrapping by the charged DNA backbone was modeled by applying a helical potential causing symmetry breaking of the nanotube electronic structure and small energetic shifts for semiconducting nanotubes (0.01 meV in water) [98, 99]. On the other hand, it is well known that DNA-wrapping redshifts the PL energy depending on the nanotube chirality by several tens of meV compared to the values reported for micelle encapsulated nanotubes in aqueous solution [27, 100, 101], which can be attributed to an increasing ϵ [80]. The surface coverage with DNA segments of finite length is expected to result in a non-uniform dielectric environment along the nanotubes [100]. Limited by diffraction, the PL information collected in confocal microscopy contains the optical response from a nanotube length of about 300 nm which is far too large to clarify details of DNA-nanotube interactions. Tip-enhanced near-field optical microscopy (TENOM) [10, 12, 165]) is ideally suited to visualize and quantify the ϵ influence on the emission energy along the DNA-nanotube hybrid system.

Photoluminescence measurements on single nanotubes using confocal spectroscopy revealed PL energy variation from different nanotube species and also nanotubes with the same chirality (n,m) [28]. Here the confocal spectroscopy was used as a first step to study the PL from

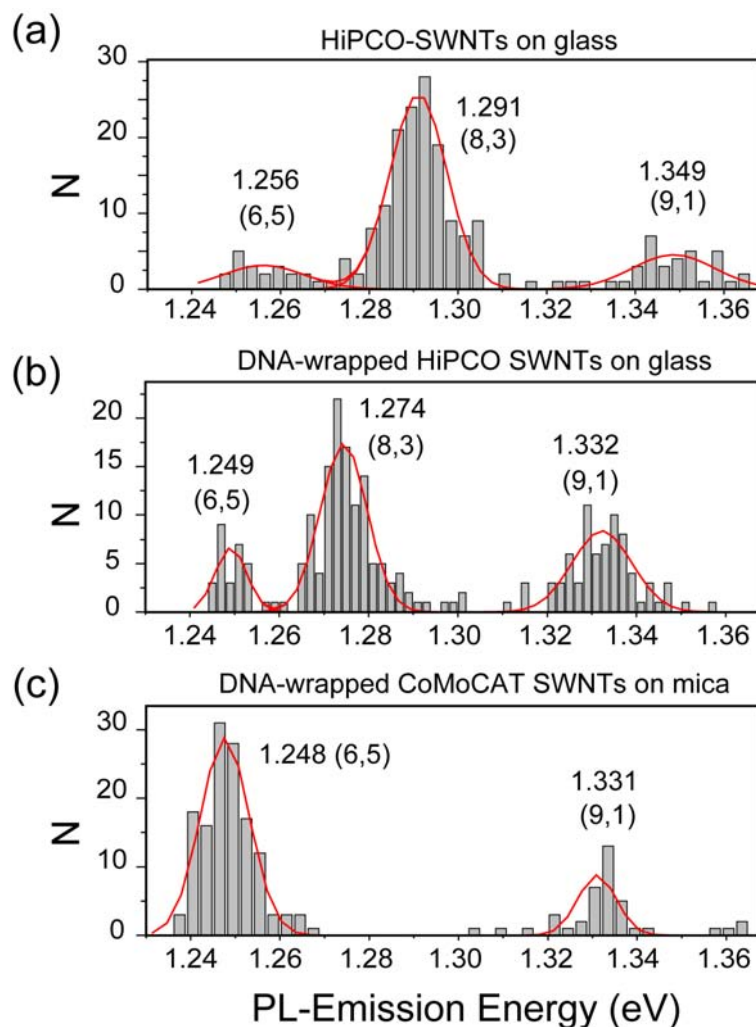


Figure 42: Histogram of PL emission energies from 203 HiPCO nanotubes (a), 235 DNA-wrapped HiPCO nanotubes (b) spin-coated on glass and 232 DNA-wrapped CoMoCAT nanotubes (c) spin-coated on mica upon laser excitation at 632.8 nm. The emission energies vary around center energies that are used for chirality assignment based on literature data [27]. DNA-wrapping causes a redshift for all chiralities. DNA-wrapped HiPCO and CoMoCAT nanotubes on different substrate have almost the same emission energies while the histogram reflects the chirality distribution. (a) and (b) courtesy of Tobias Gokus.

single DNA-wrapped and unwrapped nanotubes deposited on substrates. Figure 42 displays the histogram of PL emission energies from 203 HiPCO nanotubes (a), 235 DNA-wrapped HiPCO nanotubes spin-coated on glass (b) and 232 DNA-wrapped CoMoCAT nanotubes spin-coated on mica (c) obtained using confocal spectroscopy. The emission energies show a Gaussian distribution centered at energies that are assigned to different chiralities based on literature data [27]. The emission energies of DNA-wrapped HiPCO nanotubes are red-shifted by 7-17 meV compared to unwrapped HiPCO nanotubes varying with nanotube chiralities as discussed in [97,100], e.g. (6,5) nanotubes are red-shifted by 7 meV while (9,1) nanotubes are red-shifted by 17 meV. DNA-wrapped CoMoCAT nanotubes on mica and DNA-wrapped HiPCO nanotubes on glass exhibit the same PL energies (Figure 42(b) and (c)) while the chirality distribution differs due to different catalytic growth, e.g. (6,5) enriched in the case of the CoMoCat material. In accordance with [100] DNA-wrapped (6,5) nanotubes show an emission energy of $E_{conf} = 1.249$ eV while unwrapped (6,5) nanotubes emit at $E_0 = 1.256$ eV.

Taking advantage of high resolution TENOM, we are able to study the optical properties focusing on a single DNA-wrapped nanotube. As displayed in Figure 43, near-field PL from a single DNA-wrapped CoMoCAT (6,5) nanotube spin-coated on mica was obtained. Figure 43(a) and (b) are the simultaneously recorded topography and near-field PL images in a $1 \mu m^2 * 1 \mu m^2$ scan area, respectively. The scale bar indicates a lateral resolution of about 15 nm. The topographic height varies from 0.75 nm to 1.8 nm resulting from spatial transitions between DNA-wrapped and unwrapped nanotube segments. While individual DNA segments forming a regular pitch are not resolved as in [95] or in Figure 14, the small height variation confirms the absence of large DNA aggregates and indicates nanotube wrapping by a single DNA layer. The PL image was obtained by measuring spectra at each pixel during the scan with an acquisition time of 0.4s at a laser power of 100 μW . Figure 43(b) represents the integrated intensity from 970 nm to 1030 nm covering the emission range of (6,5) nanotubes [27]. The PL signal is rather extended along the entire nanotube although with somewhat varying intensity. The far-field contribution was also detected along the nanotube, which appears far weaker and broader.

The center emission energies were obtained by fitting each spectrum with a single Lorentzian line shape function and plotted in Figure 43(c) and (d). Apparently, the emission energy varies between 1.259 eV and 1.241 eV along the nanotube, as indicated by the two red dashed lines in Figure 43(c) while the average of all near-field spectra in the gray area centered around 1.249 eV coincides with the average value of (6,5) nanotubes from confocal far-field measurements as shown in Figure 42. Figure 43(d) is the 2D image of the variation of emission energy along

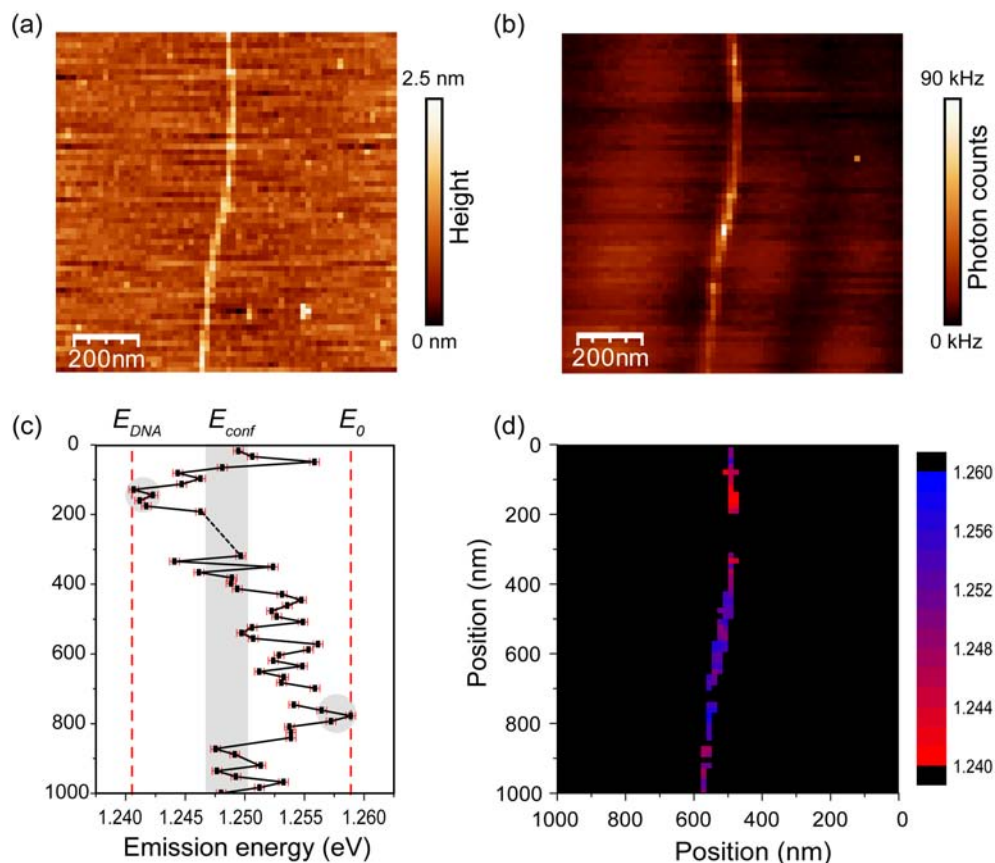


Figure 43: Simultaneously recorded topography (a) and near-field PL image (b) of a DNA-wrapped CoMoCAT (6,5) nanotube on mica. The PL image was obtained by measuring spectra at each pixel and represents the integrated intensity between 970 nm and 1030 nm covering the emission range of (6,5) nanotubes. For each pixel the emission spectrum was fitted with a single Lorentzian lineshape function to extract the central emission energy that is plotted in (c) and (d). Strong energy variations occur between 1.259 eV and 1.241 eV on a length scale of about 20 nm (the error bar is about 0.7 meV indicated by the short red horizontal lines in (c).) The energy fluctuations occur around the confocal average $E_{conf} = 1.249$ eV that is marked by the vertical gray bar while the maximum observed energy corresponds to the confocal average of unwrapped nanotubes $E_0 = 1.256$ eV marked by the dashed line. Apparently, some nanotube segments are not wrapped by DNA.

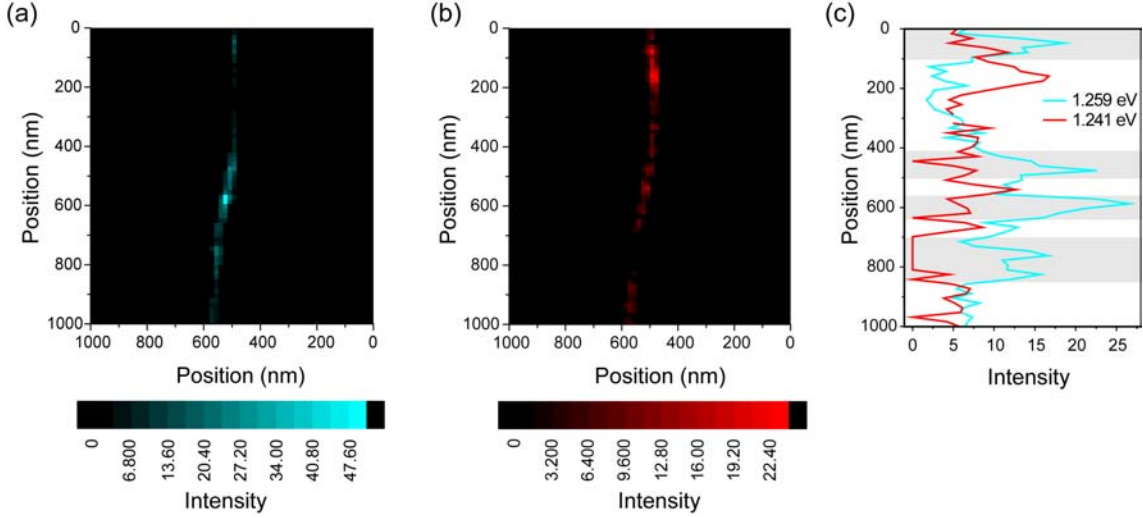


Figure 44: After fitting each spectrum with two Lorentzian peak functions at E_0 and at E_{DNA} , the intensities are plot in (a) and (b) representing these two distinct energetic levels. The intensity profiles in (c) exhibit anti-correlation between the two peaks located in the marked gray areas that can also be seen in images (a) and (b).

the nanotube. Since the highest energy of 1.259 eV corresponds well to the value observed for unwrapped nanotubes of $E_0=1.256$ eV we conclude that we detect parts of the nanotube that are not DNA-wrapped. In order to recover the average value observed in far-field measurements, DNA wrapping needs then to result in a larger redshift that can in fact be seen in the upper part of the nanotube with energies around 1.241 eV. Confocal measurements therefore underestimate the energy stabilization induced by DNA-wrapping by about a factor of 2. Similar near-field data obtained for (6,4) nanotubes indicates a DNA-induced energy shift of 30 meV (Figure 41(c,f)).

Limited by the spatial resolution of our experiment and the finite length of the DNA segments (≈ 20 nm), the probed nanotube length will mostly contain both unwrapped and DNA-wrapped segments leading to a superposition of emission bands at 1.259 eV and 1.241 eV, as can be seen in Figure 46(e). When fitting the spectra with two Lorentzian peaks fixed at 1.259 eV and 1.241 eV representing unwrapped and wrapped sections, Figure 43(d) can be split into two PL images displaying the respective intensities of these sections (Figure 44(a) and (b)). The intensities of the two peaks plot in Figure 44(c) show an anti-correlated behavior along the nanotube in gray areas as expected for two distinct energetic levels.

Spectra were taken at different positions on the same (6,4) nanotube upon approach and re-

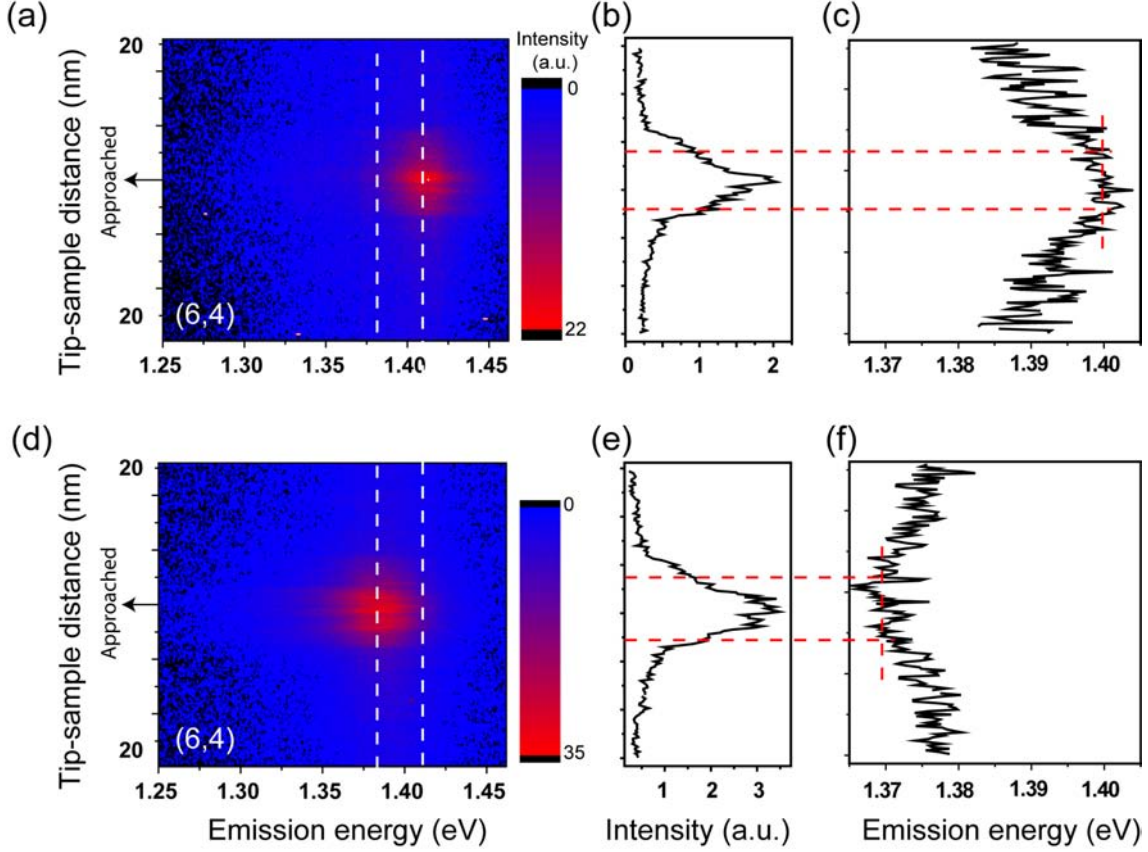


Figure 45: 2D photoluminescence maps taken at two different positions of a single (6,4) nanotube (a, d) as a function of tip-sample distance measured during tip approach and retract. The difference between the two emission energies, marked by two white dashed lines, is due to DNA-wrapping. The PL intensity is strongly enhanced at small tip-sample distance and reaches the maximum when the tip is approached marked by the arrows in (a) and (d), as shown in (b) and (e). The spectra are fit with single Lorentzian peak functions to determine the center emission energies at different tip-sample distances up to 20 nm and shown in (c) and (f) resolving the transition between confocal and near-field dominated peak energies. Within the near-field range, $\leq 5\text{nm}$ guided by the red dashed line, the emission energies are constant within the experimental precision ($\pm 2\text{meV}$).

tracting as shown in Figure 45. A gradual energy transition between confocal far-field and near-field spectra upon approaching the tip can be observed in Figure 45. For tip-sample distances larger than 20 nm, the detected signal represents the confocal spectrum resulting from spatial averaging. When the tip is closer within 10 nm distance a strong signal enhancement occurs (Figure 41(b) and (e)) and the near-field spectrum resulting from the nanotube section directly underneath the tip is detected. The emission energies at 1.41 eV and 1.37 eV marked with white dashed lines in Figure 41(a) and (d) are near-field PL energies from un-wrapped and wrapped segments, respectively. While the peak energies in Figure 41(c) and (f) reveal the confocal energy being about 1.385 eV (energy measured with tip further than 20 nm away) is the averaged energy. The results prove that the observed emission energy variations reported in this work are not affected by the presence of the metal tip but only caused by DNA-wrapping as discussed in section 5.4 for Figure 41. Moreover, the spectra also provide an evidence that emission energies in confocal measurements result from the spatial averaging thereby underestimating redshift caused by DNA-wrapping.

Based on the information of confocal and near-field PL energies, Figure 46 further compares the confocal and near-field PL spectra of the (6,5) nanotube in Figure 43 obtained at position 150 nm and 750 nm as marked by gray circles in Figure 43(c). Both confocal spectra (spectrum (a) and spectrum (b)) show a single broad peak following a Gaussian line shape function with full width at half maximum (FWHM) of 40 meV caused by the superposition of emission from both DNA-wrapped and unwrapped nanotube segments in the focus area. The near-field spectra resulting from a wrapped segment at 1.241 eV (spectrum (c)) and an unwrapped segment at 1.259 eV (spectrum (d)) are significantly sharper with FWHM of 27 meV and 25 meV, respectively. Spectrum (e) taken at position ≈ 80 nm on the other hand clearly shows two Lorentzian peaks (FWHM = 25 meV) at 1.240 meV and 1.259 meV reflecting the simultaneous detection of emission from wrapped and unwrapped segments. In agreement with the energy distribution in Figure 43(c), we mostly observe spectra containing two peaks. The near-field spectra detected here for DNA-wrapped (6,5) nanotubes are not only sharper than the confocal spectra of the material on substrates but are also found to be sharper than the conventional PL spectra of the material in solution of about 34 meV (data not shown).

In the following, we aim at extracting the transition length between red-shifted and non-shifted emissive states. To understand the origin of the different PL spectra we illustrated the energy landscape and its modulation induced by the dielectric environment along the DNA-wrapped nanotube in Figure 46(f) schematically. The PL energy is lowered due to the increased dielectric

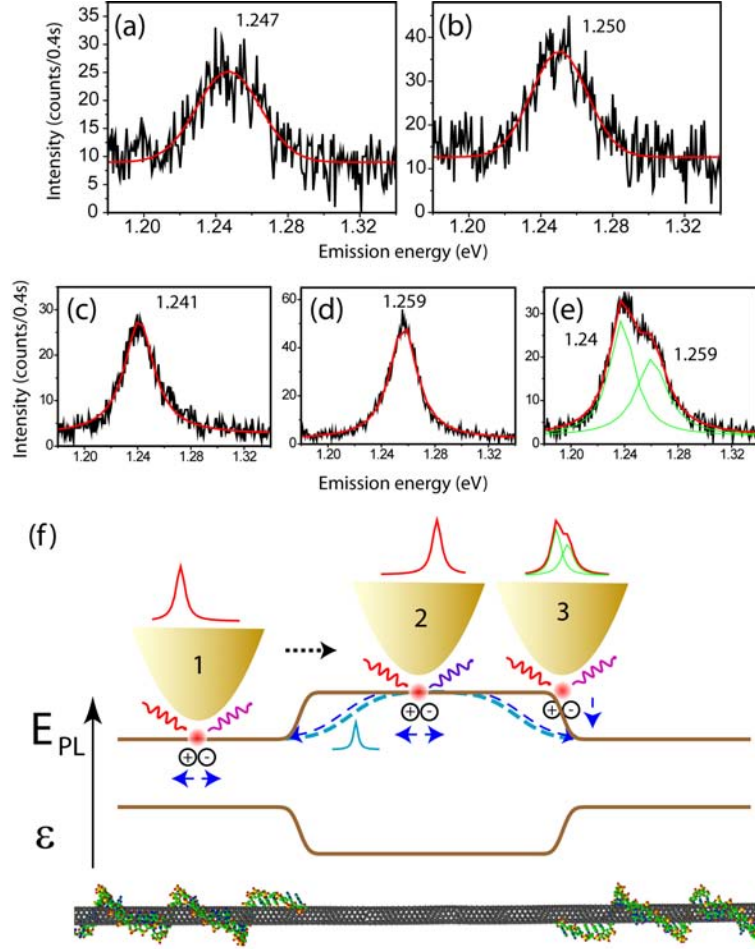


Figure 46: Confocal (a,b) and near-field (c-e) PL spectra of a DNA-wrapped CoMoCAT SWNT on mica together with Gaussian and Lorentzian fit curves for (a,b) and (c-e), respectively. Confocal and near-field spectra were detected at the locations along the nanotube in Figure 43(c) marked by grey circles. Both confocal spectra (a,b) feature a full width at half maximum (FWHM) of 40 meV, while the near-field spectra (c,d) are significantly sharper with a FWHM of 27 meV and 25 meV, respectively. In the near-field spectrum (e) on the other hand two distinct two peaks are clearly resolved with FWHM 25 meV attributed to DNA-wrapped and unwrapped sections of the nanotube. (f) Schematic illustration of the exited state energy E_{PL} landscape (brown line) along the DNA-wrapped nanotube including two wrapped parts with an unwrapped part in between, as indicated by the nanotube below. ϵ denotes the dielectric constant of the local environment reflecting local DNA wrapping. For the tip probing at different positions (numbers 1,2,3) on the nanotube, the expected spectra are shown on top of each position.

constant ε associated to DNA-wrapping. Near-field scanning along the DNA-wrapped nanotube yields different optical responses when the tip is at different positions marked with numbers 1, 2 and 3. At position 1, the nanotube is locally excited on top of a DNA-wrapped segment and radiative exciton recombination occurs locally leading to low emission energy in the spectrum as shown in Figure 46(c) and indicated by the spectrum above the tip. At position 2 the tip probes the high emission energy of the bare nanotube as shown in Figure 46(d). In the case of the tip probing on top of both DNA-wrapped and unwrapped parts depicted at position 3, the spectrum reveals double peaks including both low and high emission energies, as shown in Figure 46(e). The simultaneous observation of two distinct emission peaks as in Figure 46(e) demonstrates that the transition between the two emissive energy levels occurs rapidly with respect to our spatially resolution, i. e. within less than 15 nm. In contrast, slower changes as indicated by the blue dashed line in Figure 46(f) would result in a single emission peak shifting in energy between high and low energy states.

Since nanotubes are extended 1-dimensional systems exciton mobility needs to be considered increasing the complexity of the discussion. An exciton diffusion range of about 100 nm has been deduced from blinking traces [83, 184]. In general, exciton mobility will result in an effective energy redistribution in which locally generated mobile excitons (blue arrows in Figure 46) would be trapped at lower energetic levels within a diffusion radius of about $100/2 \text{ nm} = 50 \text{ nm}$. The ratio of emission intensities from the two states will therefore depend on the competition between exciton decay and exciton mobility which is difficult to quantify experimentally. Moreover, the metal tip is expected to decrease the lifetime of the exciton by increasing both radiative and non-radiative decay rates [140, 148, 165], which will reduce the effective exciton diffusional range thereby increasing the relative contribution of high energy emission. Remarkably, a single high energy peak is only observed at position 750 nm in Figure 43(c-f), where the lower energy peak is absent for a long nanotube section of about 100 nm between 700-800 nm in agreement with this discussion.

Besides modifying the local dielectric environment of the nanotube, DNA-nanotube interactions could also result from the negatively charged DNA backbone causing charge transfer or local doping of the nanotube. Charge carrier doping is predicted to reduce the PL intensity by phonon-assisted indirect exciton ionization [173] and local quenching of PL was indeed observed for hole doping [184]. The nanotubes presented in Figure 2 and Figure 4 on the other hand showed extended and rather uniform emission intensities without indications of local quenching.

In summary, TENOM was applied to study single DNA-wrapped CoMoCAT nanotubes. Two

distinct emission bands are identified and assigned to emission from DNA-wrapped segments unwrapped segments, distinguished by energy shifts of 18 meV for (6,5) and 30 meV for (6,4)-nanotubes, respectively. The PL energy shift along nanotubes induced by DNA segments turns out to be a factor of 2 higher than the value determined from confocal measurements representing spatial averaging. Based on the simultaneous detection of PL bands from both DNA-wrapped and unwrapped segments, the transition between the two energetic levels occurs on a length scale smaller than our spatial resolution of 15 nm can be determined. This results demonstrate that nanotubes act as nanoscale reporters of their local dielectric environment making them ideal candidates for sensing applications of single nanoobjects on a length scale of few nanometers.

7 Exciton transfer and propagation in SWNTs

This section is based on the paper "Exciton Energy Transfer in Pairs of Single-Walled Carbon Nanotubes" published in Nano Letters.

Single-walled carbon nanotubes feature unique electronic properties making them ideal candidates for ultra-high density devices in electronics, photonics and optoelectronics [15–17]. At nanoscale distances exciton energy transfer from large to small bandgap nanotubes is expected to occur facilitating novel architectures including crossbars and 3D arrays but also imposing design restrictions. Photoluminescence in semiconducting nanotubes results from exciton recombination that decay on picosecond time-scales [22–24] and is found to be quenched in bundles [21, 185, 186]. Very recently, resonant exciton energy transfer between semiconducting nanotubes has been observed for SWNTs in micelles suspensions for the first time and was explained by near-field coupling corresponding to fluorescence resonance energy transfer (FRET) well-known for molecular systems [187]. In ref [188], spectroscopic signatures of internanotube transfer were observed, and it was suggested that efficient coupling results from carrier migration requiring direct physical contact. In ensemble measurements, however, the identification of donor and acceptor spectral signatures is complicated by overlapping contributions from different nanotube species, including phonon-assisted absorption and possible emission from lower lying defect-associated states [189–191]. Up to now, the range of exciton transfer and its efficiencies are unknown, which can be extracted preferentially from single bundles. In this section, I will present energy transfer observed between two semiconducting nanotubes and based on the data will estimate transfer efficiencies and time scales.

7.1 Exciton energy transfer between two semiconducting nanotubes

The sample used in this section consists of DNA-wrapped CoMoCAT nanotubes spin-coated on mica. CoMoCAT SWNTs were sorted by using discriminating surfactants and wrapped by DNA after sorting. The density gradient ultracentrifugation isolates the narrow distributed, chirality enriched nanotubes [90–92]. Chirality enriched materials increase the probability for observing two interacting semiconducting nanotubes with similar excited state energies, supporting resonant energy transfer and facilitating their optical detection.

Figure 47 illustrates the topography (a) and the simultaneously recorded near-field PL image (b) of nanotubes. The PL image represents the intensity detected in the spectral range from

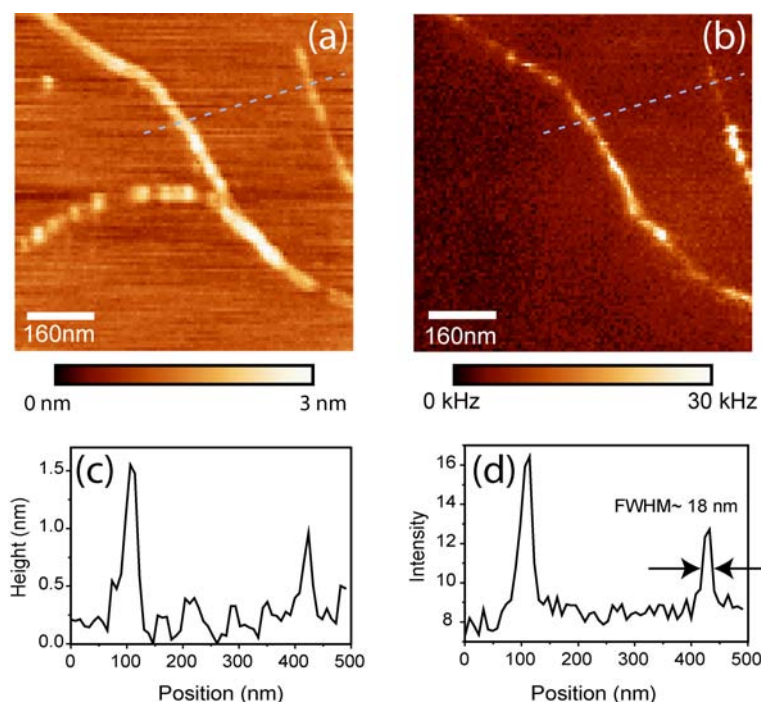


Figure 47: Simultaneously recorded topography (a) and near-field PL image (b) of DNA-wrapped single-walled carbon nanotubes on mica. The scan area is $800 \times 800 \text{ nm}^2$. The PL image was formed by detecting all emission between 860 nm and 1050 nm upon laser excitation at 632.8 nm using $5 \mu\text{W}$. c, d, Cross sections taken along the dashed lines in (a) and (d) respectively. The height of the nanotube structure extending from the upper left to the lower right corresponds to what is expected for single DNA-wrapped nanotubes and varies from 1.5 nm to 2.5 nm. The optical resolution of $\approx 18 \text{ nm}$ is derived from the FWHM of the peaks in the cross section in (d).

860 nm to 1050 nm and features a spatial resolution of 18 nm. The sharp and intense PL spots of the nanotube on the right indicate the presence of highly localized excited states that could be formed by lower lying states related to charged defects or environmental perturbations [165]. In contrast, the nanotube structure extending from the upper left to the lower right exhibits rather uniform and extended PL intensity, a typical observation for DNA-wrapped nanotubes and nanotubes in SDS micelles [165]. The nanotube oriented horizontally extending from the left into the center of the topographic image is not visible in the PL image and is therefore either metallic or its luminescence energy is outside of our detection range.

In the following, we focus on the nanotube structure extending from the upper left to the lower right that is clearly visible in both images. The topographic height of the structure is around 1.5 - 2.5 nm (Figure 47 (a), (c)), a value expected for single DNA-wrapped nanotubes [95]. However, based on the topographic data, it will be extremely difficult to distinguish single nanotubes from thin bundles. The uniform height of the structure and the absence of larger adherent particles that could modify the tip-nanotube distance and thus affect the signal enhancement provided by the tip [10, 12, 148] allows us to directly compare intensities at different nanotube sections and to attribute changes to nanotube properties.

Figure 48 presents PL images derived from spectra taken at each pixel of the sample area from Figure 47. After splitting the emission into selected spectral windows, the structure extending from the upper left to the lower right in Figure 47(a) and (b) is found to contain two clearly distinct emission peaks originating from a (9, 1) and a (6, 5) nanotube as evidenced by the emission energies of about 925 nm and 1000 nm, respectively (Figure 47(c) and (d)). The red-shift compared to the 912 nm emission energy reported for the (9, 1) nanotube and the 975 nm for (6, 5) [27] results from DNA-wrapping [164].

Emission from the (9, 1) nanotube (Figure 48(a)) occurs in four bright segments, while emission from the (6, 5) nanotube (Figure 48(b)) is more extended for about 1 μm . This can also be seen in the intensity profiles shown in Figure 48(d) taken along the two dashed lines in Figure 48(a) and (b). The four bright segments in the cross section of the (9, 1) nanotube feature lengths between 80 and 150 nm. As four independent short (9, 1) nanotubes attached regularly along the (6, 5) nanotube would be very unlikely and since the PL of the (9, 1) does not disappear completely in between the bright segments, it is evident that we observe a bundle formed by a (9, 1) and a (6, 5) nanotube. Moreover, characteristic G-band Raman scattering was observed from the (9, 1) nanotube that is resonantly enhanced at $E_{\text{Laser}} = E_{22}^{(9,1)} + \hbar\omega_G$ extending along the detected PL spots marked by dashed arrows in Figure 48(e) [27, 36]. Raman scattering from the (6, 5) nanotube is not detected because of weak electronic resonances and low excitation power.

Remarkably, the PL of the (6, 5) nanotube is found to be stronger when the PL of the (9, 1) nanotube decreases, seen for example in the centre of the cross sections between 460 and 640 nm and around 280 nm and 740 nm. Strong PL of the (9, 1) nanotube on the other hand occurs in sections where (6, 5) emission is weaker, e. g. at 420 nm and between 780 and 920 nm. We attribute this anti-correlation of the PL intensities to energy transfer from the large bandgap (9, 1) nanotube to the small bandgap (6, 5) nanotube as expected in bundles. However, the fact

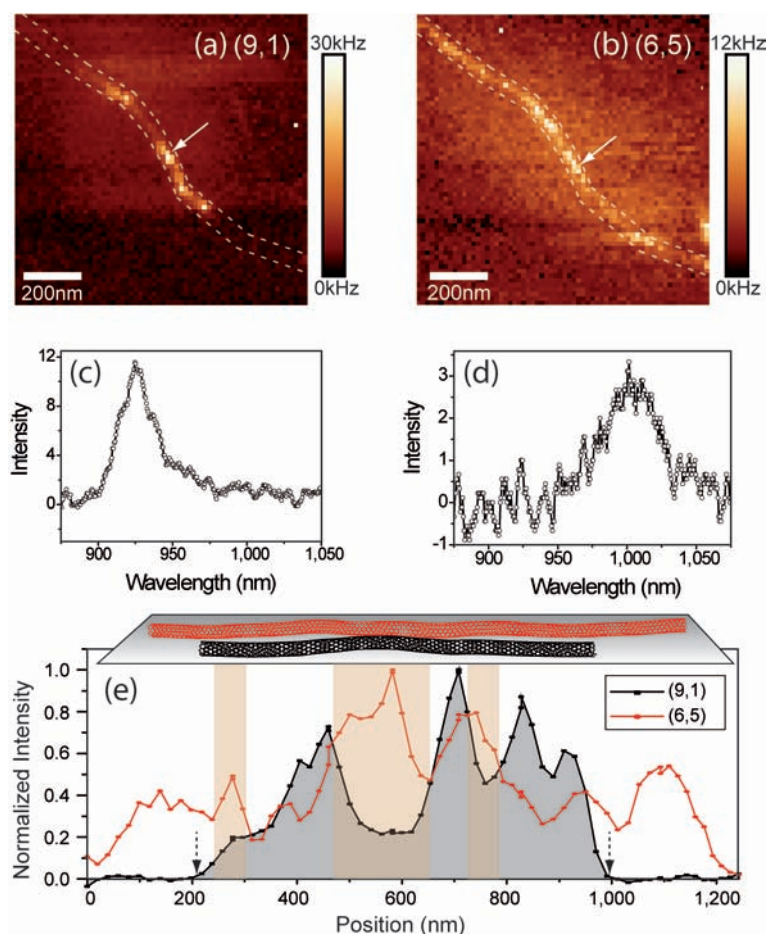


Figure 48: Near-field PL images with 64×64 pixel of the DNA-wrapped single-walled carbon nanotubes seen in Figure 47 obtained by measuring spectra at each pixel. (a) and (b) represent the integrated intensities within selected spectral windows ranging from 910 to 940 nm for (a) covering the emission of (9,1) nanotubes and from 990 to 1020 nm for (b) covering the (6,5) emission. Evidently, the nanotube structure seen in Figure 47 is a nanotube bundle composed of two nanotubes with different chiralities. The chirality assignment is based on the emission spectra detected at the positions marked with the white arrows shown in (c) and (d) that exhibit the characteristic energies of (9,1) and (6,5) nanotubes, respectively. The scan area is $1 \times 1 \mu\text{m}^2$. Laser excitation at 632.8 nm with $100 \mu\text{W}$ and an integration time of 400 ms per spectrum were used. (e) presents intensity profiles taken along the (9,1) (black line) and the (6,5) nanotube (red line) summed between the two dashed lines in (a) and (b), respectively. The two dashed arrows mark beginning and end of the (9,1) nanotube determined from the simultaneously detected G-band Raman signal (not shown).

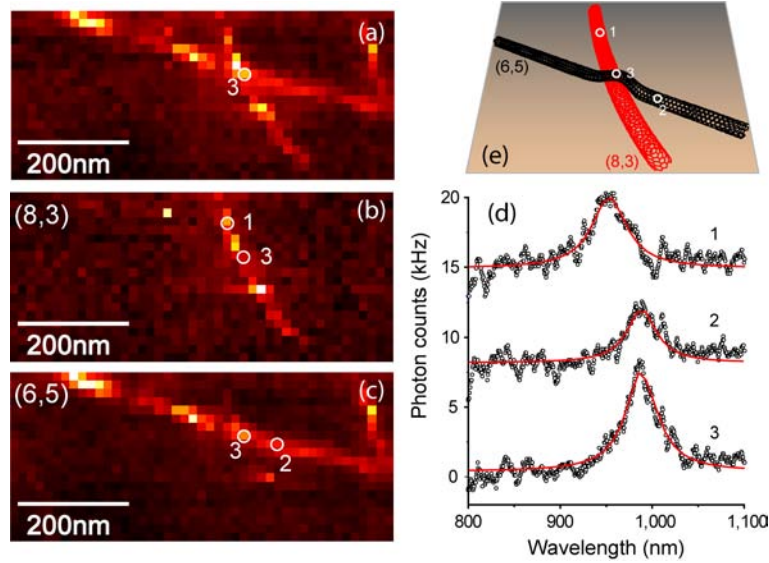


Figure 49: Near-field PL image of two intersecting nanotubes obtained by measuring spectra at each pixel representing the integrated intensity within selected spectral windows. (a) Total intensity. The intensity integrated from 915 nm to 945 nm is shown in (b) and from 970 nm to 1010 nm in (c). (d) Spectra taken at the pixels marked by white circles and numbers 1-3 in (a), (b) and (c). (e) Simplified schematic of the intersecting nanotubes.

that PL from (9, 1) is still detectable even within the bundle clearly shows that the efficiency of the energy transfer is limited. Spatial variations of the transfer efficiency can be understood in terms of varying inter-nanotube distances. The finite length of DNA-segments and resulting partial DNA-wrapping could allow for different nanotube-nanotube spacing.

Besides several cases for energetic coupling of nanotubes within bundles we observed indications for transfer in nanotube intersections. An example is presented in Figure 49 (a)-(c). Based on their emission energies (spectrum 1 and 2 in Figure 49(d)), the nanotubes crossing in the centre of the image are identified as (8, 3) and (6, 5), respectively. At the intersection however, only the PL of the small bandgap nanotube (6, 5) is observed (spectrum 3 in Figure 49(d)). The topographic height at the crossing point is about 3 nm (data not shown), indicating that the maximum wall-to-wall distance between the two intersecting nanotubes is around 1.5 nm based on nanotube diameters of 0.75 nm. The reduced intensity of the large bandgap nanotube (8, 3) at the intersection implies that energy transfer occurs in the present configuration for wall-to-wall distances between 0 and 1.5 nm. Notably, emission from the (8, 3) nanotube is found to

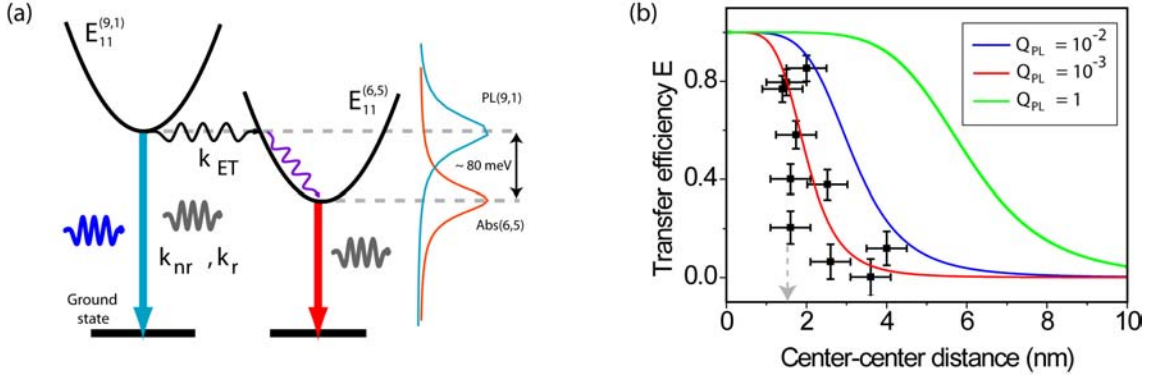


Figure 50: (a) Energy level scheme of resonant transfer in a single donor-acceptor pair formed by a (9, 1) and a (6, 5) nanotube. (b) Distance dependence of the energy transfer efficiency $E(d) = 1 - I(d)/I_0$ for a single (9, 1) / (6, 5) pair determined from the data shown in Figure 48. The inter-nanotube distance was determined from the centre of Gaussian line shape functions fitted to cross sections taken at different positions along the nanotube bundle in the PL images. The gray arrow indicates the distance at which the two nanotubes touch. The solid lines are calculated Förster energy transfer efficiencies accounting for a PL quantum yield of $Q_{PL} = 1$ (green line), $Q_{PL,0} = 10^{-2}$ (blue line) and $Q_{PL,0} = 10^{-3}$ (red line), respectively.

recover within few nanometer distance to the intersection (Figure 49(b)) indicating that the range of efficient transfer is limited in agreement with our findings for the nanotube bundle in Figure 48.

Based on the image data presented in Figure 48 we now estimate the efficiency, the range and the time-constant of energy transfer. As the nanotubes in Figure 47(a) can not be distinguished by our topographic data, optical information can be used to determine the position of two spectrally isolated emitters with nanometer accuracy far below the resolution limit of the experiment [192, 193]. Cross sections perpendicular to the nanotubes were taken at different locations in (Figure 48(a),(b)) and were fit with Gaussian line shape functions to determine the in-plane position with maximum intensity for the two spectral windows (data not shown). Center-to-center distances ranging from $d = 1$ to 4 nm were found between the maxima of the two nanotubes in corresponding cross sections. For each distance we determined the transfer efficiency $E(d) = 1 - I(d)/I_0$ using the measured intensities $I(d)$ and I_0 of the (9, 1) nanotube. The data points (Figure 50(b)) reveal a very fast decay and support our assignment of the PL intensity variations to variations of distance dependent energy transfer.

To derive the energy transfer rate k_{ET} , the ratio of the PL intensities n is expressed as the ratio of the PL quantum yields Q_{PL} with and $Q_{PL,0}$ without energy transfer

$$n = I/I_0 = Q_{PL}/Q_{PL,0} = \frac{k_r + k_{nr}}{k_r + k_{nr} + k_{ET}}. \quad (50)$$

Here k_r and k_{nr} denote the radiative and the non-radiative rate in the presence of the metal tip. The total decay rate of individual DNA-wrapped (9, 1) nanotubes in the absence of a metal tip at room temperature is about $k = k_r + k_{nr} \approx (8ps)^{-1}$ being dominated by k_{nr} [29]. In the case of tip-enhancement, this value will represent a lower limit since the tip is expected to increase both radiative and non-radiative decay rates [148, 165]. As a result, the maximum transfer rate $k_{ET} \approx k(1 - n)/n$ observed in our measurements is about $0.5/ps - 1/ps$.

7.2 Förster-type energy transfer modeling in 1D nanotubes

Using our findings for the transfer range and the time scales we can discuss contributions from different possible transfer mechanisms. Electron tunneling observed for nanotube intersections and between the constituents of multi-walled nanotubes requires overlapping wavefunctions and will be short ranged on a sub-nanometer scale [194]. Förster-type transfer efficiencies can be calculated for molecular systems as a function of the dipole-dipole distance.

For two dipoles with distance R as shown in Figure 51, The energy transfer efficiency can simply be calculated by the ratio of transferred intensity I_{ET} and the original intensity I_0 ,

$$E(R) = \frac{I_{ET}}{I_0} = \frac{I_0 - I}{I_0}. \quad (51)$$

The energy transfer rate k_{ET} can be expressed as [102]

$$k_{ET} = k_r \left(\frac{R_0}{R} \right)^6 \quad (52)$$

From equation 50, 51 and 52, we can obtain the Förster energy transfer efficiency accounting for the quantum yield $Q_{PL,0}$ of the emitter expressed as [102]

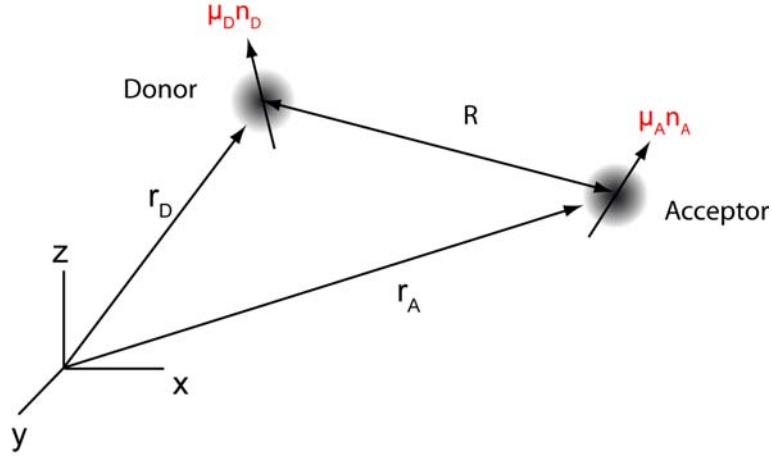


Figure 51: Energy transfer between two dipoles (donor and acceptor) with the distance R . The donor dipole is oriented in the direction μ_D with the unit vector n_D , the acceptor is oriented in the direction μ_A with the unit vector n_A . r_D and r_A denote the distance of two dipoles to the zero coordinate.

$$E(R) = \frac{1}{1 + Q_{PL,0}^{-1} \left(\frac{R}{R_0}\right)^6} \quad (53)$$

Here k is the total decay rate including both radiative and non-radiative relaxation. The Förster radius R_0 is calculated by [102]

$$R_0 = \frac{9c^4 \kappa^2}{8\pi} \int_{-\infty}^{\infty} \frac{f_D(\omega) \Gamma_A(\omega)}{n_r^4 \omega^4} d\omega \quad (54)$$

where $f_D(\omega)$ and $\Gamma_A(\omega)$ are the fluorescence spectrum of the donor and the absorption spectrum of the acceptor, respectively. n is the refractive index. κ is the orientational factor given by [102]

$$\kappa^2 = [n_A \cdot n_D - 3(n_R \cdot n_D)(n_R \cdot n_A)]^2 \quad (55)$$

Here n_A and n_D are unit vectors in the direction of μ_A and μ_D , respectively. The factor κ^2 has a value in the range $\kappa^2 = [0 \dots 4]$.

For extended quasi one dimensional nanotubes the near-field radiation pattern and thus the effective transfer rates are expected to be different than in the case of point dipoles [195]. For

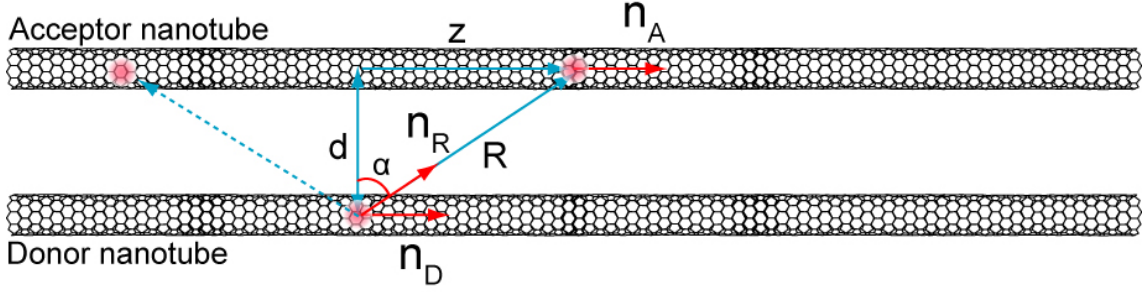


Figure 52: Förster-type energy transfer modeling between two parallel nanotubes separated by a distance d . n_R , n_A and n_D are unit vectors in the direction of \vec{R} , \vec{A} and \vec{D} . α is the angle between \vec{R} and \vec{d} . Energy from the locally excited donor marked with red shadow can be transferred to the acceptor along the whole acceptor nanotube.

two parallel nanotubes at distance d , see in Figure 52, the total transfer rate from a locally excited donor (red shadow) to the acceptor nanotube (red shadows all possible along the nanotube) can be estimated by integrating the rates along the z axis of the acceptor following

$$k_{ET} = k_{rad} \int_{-\infty}^{\infty} \left(\frac{R_0}{R}\right)^6 dz \quad (56)$$

where $R = \sqrt{d^2 + z^2}$ is the dipole-dipole separation. The total transfer efficiency is thus

$$E(d) = \frac{1}{1 + Q_{PL,0}^{-1} \int_{-\infty}^{\infty} \left(\frac{R}{R_0}\right)^6 dz} \quad (57)$$

Using the experimentally determined absorption cross section per nanometre length of (6, 5) nanotubes $\Gamma_A = 10^{-13} \text{cm}^2/380 \text{nm}$ [196], the absorption and PL spectra of the participating nanotubes and the orientational factor $\kappa = 1 - 3\sin^2\alpha$ with α being the angle between \vec{R} and \vec{d} and the refractive index of mica ($n_r = 1.56$), the transfer efficiencies calculated by equation 57 are shown in Figure 50(b) together with the experimentally determined values from Figure 48. Good agreement can be seen for a quantum yield of $Q_{PL,0} = 10^{-3}$, a typical value discussed for nanotubes on substrates. Exciton transfer clearly depends very sensitively on the nanotube-nanotube distance and is limited to only few nanometres because of competing fast non-radiative relaxation processes leading to low $Q_{PL,0}$.

According to Förster theory, the energy transfer efficiency depends on the spectral overlap of emission and absorption bands and will therefore be controlled by the chirality tuple $(n, m)_{donor}/(n, m)_{acceptor}$ of a particular donor-acceptor nanotube pair. The present observation of efficient transfer for the (9,1)/(6,5) nanotube pair spaced by few nanometers and having a spectral shift of about 80 meV between emission and absorption maxima supports the discussion in ref [187] on the energy transfer in bundles. In addition, phonon-assisted absorption of the accepting nanotube is likely to increase spectral overlap [191]. While in the case of the (8,3)/(6,5) nanotube pair in Figure 49, the overlap will be large due to a small spectral shift of about 30 meV, the particular cross configuration will reduce transfer by decreasing the orientational factor κ . In general, maximum transfer efficiency and range are expected for parallel nanotubes within bundles.

In summary, exciton energy transfer in pairs of semiconducting nanotubes using high-resolution optical microscopy and spectroscopy was observed for the first time. Transfer efficiencies between two nanotubes were quantified for different internanotube distances and explained by Förster-type electromagnetic near-field coupling. The range of efficient transfer is found to be limited to a few nanometers because of competing fast non-radiative relaxation responsible for low photoluminescence quantum yield. For highly luminescent materials, on the other hand, transfer is predicted to be long-ranged and needs to be considered in the design of integrated exciton based devices.

8 Exciton propagation towards the end of nanotubes

Nanotube ends are of great importance for applications as 1D wires and for understanding the effect of local defects on the properties of crystalline materials. Theoretical modeling based on tight-binding calculations [197] and experimental results using scanning tunneling spectroscopy (STS) [198–200] indicate dramatic changes in the electronic structure towards the carbon nanotube ends. In particular, the lowest singularity in the density of states diminishes and is replaced by a single prominent peak close to the Fermi level or at higher energies depending on structural details, i. e. open or closed ends. These band modifications are confined to the nanotube end with spatial extensions of few nanometers only. Propagation of mobile excitons in the axial direction on the other hand is expected to lead to quenching at the ends resulting in reduced PL [86]. In this section I aim at visualizing the excited states towards the nanotube ends and the spatial extension of the quenching effects cause by the ends.

Figure 53 shows simultaneously obtained topography (a) and near-field PL (b) images of a DNA-wrapped carbon nanotube end. The nanotube topography ends at the position marked with the white dashed line, while PL already fades out before the line. (c) plots the profiles along the black dashed line in both (a) and (b). The line-circle curve represents the topographic height variation and the line-triangle represents the PL intensity variation. Both intensities are normalized to 1 for better comparison. The decay of the topography profile reflects the convolution between the tip shape and the step-function representing the nanotube end. Here we interpret the position at which the topography signal dropped by a factor 2 as the end of the nanotube x_c indicated by the blue dashed line in Figure 53(c). The topography is therefore fit with a Gaussian instrument response function (IRF)

$$F_{IRF} = \exp\left(-2 \cdot \left(\frac{x - x_c}{\omega}\right)^2\right), \quad (58)$$

with ω determined by the tip diameter which can be determined by the topographic resolution. In this measurement, the nanotube end is at position 128 nm and the tip diameter is 30 nm. The upper red curve is the fit curve. The PL intensity profile clearly decays slower. The slower decay can also be distinguished by the distance between the positions with signals at half maximum, marked with the red dashed line and the blue dashed line. To model the decay rate at the nanotube end k_{end}^0 is assumed to be a finite number that is much more larger than the decay rate k away from the nanotube end. Here we assume that the quenching rate k_{end} increases

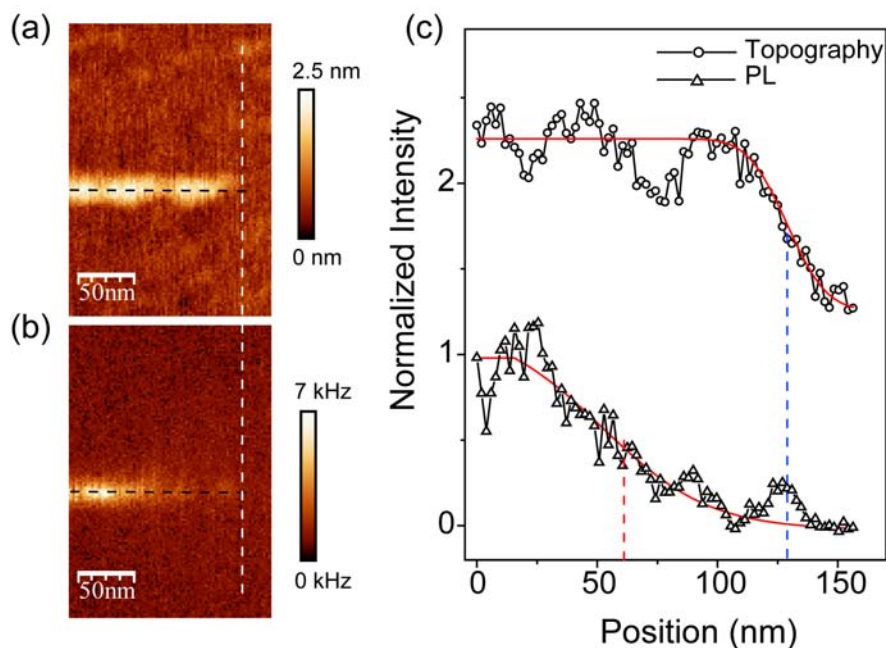


Figure 53: Simultaneously obtained topography (a) and near-field PL (b) images of a DNA-wrapped carbon nanotube end upon laser excitation at 632.8 nm. The excitation power is $5\mu W$. (c) shows profiles along the two black dashed lines in (a) and (b), representing topographic height and PL intensity, respectively. The blue dashed line indicates the position of the end of the nanotube taken at half the topographic height. The topographic profile is fit with an instrument response function (IRF) with the width determined by the topographic resolution which is 16 nm in this example (the upper red curve). The PL profile is fit by an exponential decay convoluted with the optical IRF functions account for quenching effect, giving a PL decay length of 20 nm (the lower red curve).

towards the nanotube end as an exponential function of the distance. k_{end} therefore can be expressed as

$$k_{end} = k_{end}^0 \cdot \exp\left(-\frac{x_c - x}{L}\right), \quad (59)$$

where L denotes the PL decay length, or in other words the spatial extension of PL quenching rate. The lower red curve is the convolution of the IRF function account for quenching effect in equation 59, giving a PL decay length of 20 nm. This length is longer than the length of structure induced band modification at the end [197–200], which is a good indication of exciton diffusion along the nanotube [86].

In order to provide further support for this result, similar near-field measurements were performed on another nanotube end and the data is shown in Figure 54. Figure 54 displays near-field PL (a) and topography (b) images of another nanotube end. It clearly reveals that the PL vanishes early than the topography where marked with the white dashed line. In Figure 54(c), the 3D topography image is composed together with PL intensities indicated with colors. From the color bar we can see that the nanotube appears dark towards the end. The profiles in (d) are taken along the black dashed lined in (a) and (b), respectively. By fitting the topography and PL intensity profiles using the same method as described for Figure 53, a PL decay length of 15 nm is obtained.

The data presented here including other examples giving PL decay lengths in the range of 15–40 nm clearly support the idea of non-radiative decay of mobile excitons at quenching states confined to the nanotube end. Since in TENOM the optical resolution is generally found to exceed the topographic resolution [10, 12] the slower decay of the PL signal is not caused by different signal formation processes. What’s more, the presence of the metal tip will enhance the non-radiative decay all over the nanotubes including the ends with variable degrees, the excitons diffusion caused PL decay range at the nanotube end therefore is expected to be shorter than the diffusion range reported in [184] under a complete different condition.

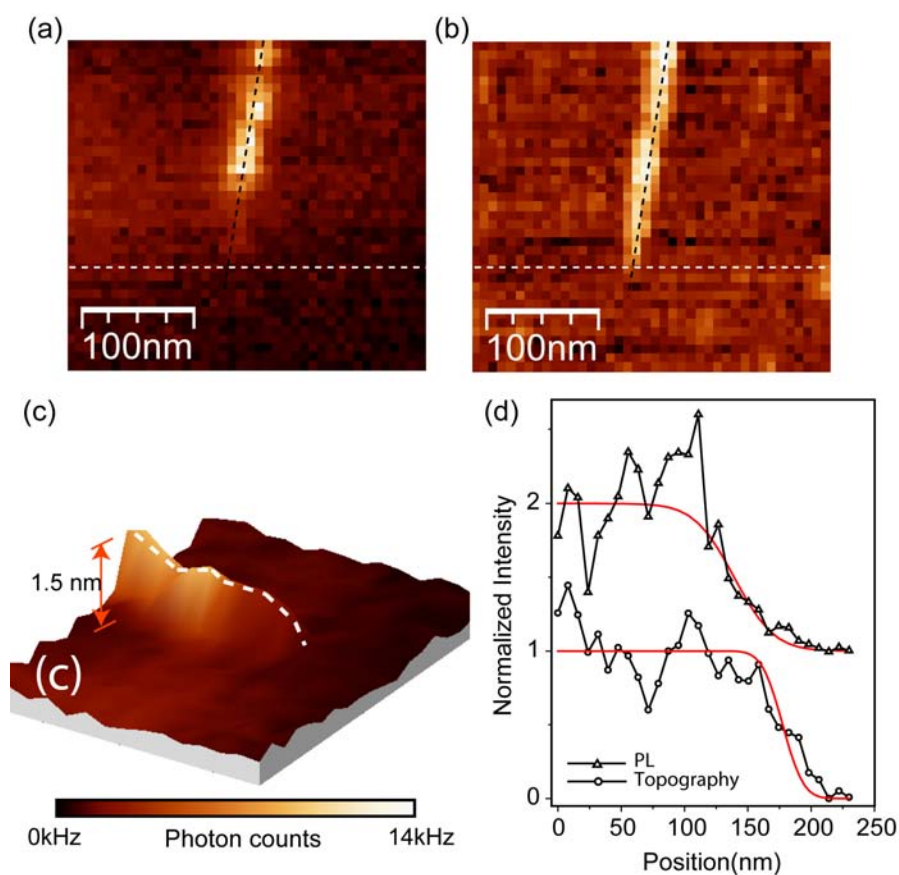


Figure 54: Simultaneously obtained near-field PL (a) and topography (b) images of a DNA-wrapped carbon nanotube end upon laser excitation at 632.8 nm. The excitation power is $5\mu W$. (c) is the 3D image composed by both topography and PL intensity. The height variation is indicated by the scale while the color bar is for the PL intensity variation. (d) shows profiles along the two black dashed lines in (a) and (b), representing PL intensity and topographic height, respectively. The red curves are fit curves as described for Figure 53. The PL decay length is 15 nm.

9 Conclusion and outlook

This thesis presented tip-enhanced near-field optical spectroscopy and microscopy on individual single-wall carbon nanotubes (SWNTs). The main emphasis was put on the exciton properties in semiconducting nanotubes studied by visualizing the photoluminescence (PL) with nanoscale resolution. The new results achieved in this thesis are summarized in the following:

Simultaneous near-field Raman scattering and PL measurements revealed non-uniform phonon modes and excitonic states along single nanotubes, providing new insights into intrinsic and extrinsic properties. Observation of PL from single nanotubes gave access to the properties of excitonic states in SWNTs with specific chirality (n,m). Near-field PL spectra taken along the nanotubes revealed spatially fluctuating emission energies. Both electron-electron interaction energy and exciton binding energy in nanotubes are sensitive to the dielectric environment because of the direct contact of each atom with the environment that controls charge carrier screening. PL energies can therefore be significantly modified by the renormalized band gap and the exciton binding energy. PL signals along single nanotubes appear either localized or extended. Trapping of excitons at impurity sites or at structural defects as well as coupling to optically inactive excitons are discussed to extinguish the PL causing localized emission. The origin of the localized PL with regular spacing of 50 to 60 nm presented in this work for the first time however is still unclear. Based on the literature, it could be explained by localized charges near the nanotubes that originate from the substrate surface or the metal tip.

Near-field Raman and PL data acquired on the same nanotube allowed for a quantitative comparison of enhancement factors. The enhancement factors are expected to be different because of the different transitions involved in Raman scattering and PL. The experimental observation showed that the enhancement of PL signals can be stronger than that of Raman scattering signals. In my thesis, I discussed enhancement of Raman and PL signals in case of both parallel and perpendicular polarized fields with respect to the nanotube axis. The very efficient PL enhancement is attributed to the low initial quantum yield of nanotubes and can be expected for any weakly emitting species. In addition, PL quenching is observed in tip approach curves competing with PL enhancement leading to an optimum tip-sample distance of about 2 to 4 nm.

DNA-wrapping is found to redshift the PL energy locally by 18 meV for (6,5) and 30 meV for (6,4) nanotubes compared to micelle-encapsulated nanotubes by increasing the dielectric constant ϵ . Two distinct emission bands are resolved in the near-field spectra and assigned

to emission from DNA-wrapped and unwrapped segments. The energy difference between two emission peaks is found to be a factor of two higher than the value determined from confocal measurements representing spatial averaging. The PL image formed by integrating the low energy intensity associated with DNA-wrapped segments shows a non-uniform wrapping of DNA along the nanotube. The transition length between the two energetic levels is smaller than the spatial resolution of 15 nm determined by the tip diameter used in the presented measurements. These results demonstrate that nanotubes are very promising candidates for sensing applications on the nanoscale.

Near-field PL microscopy of a thin nanotube bundle consisting of two semiconducting nanotubes showed exciton energy transfer from the larger band gap nanotube to the smaller band gap nanotube. Transfer efficiencies calculated by experimental data and theory based on Förster-type energy transfer considering the quantum yield revealed a very small range of efficient transfer. Energy transfer occurring only at the cross point of a nanotube intersection confirmed the limited transfer range. For highly luminescent materials theoretical estimates predict long-range energy transfer, which is important to be considered in the design of integrated exciton based devices.

Exciton diffusion has been visualized indirectly by the observation of the PL decay towards the nanotube ends. The observation supports the idea of non-radiative decay of mobile excitons at quenching states confined to the nanotube ends. The PL decay range of 15-40 nm is in general agreement with the exciton diffusional range deduced from blinking traces using confocal microscopy.

The results presented in this thesis provide new insights and observations of optical properties of carbon nanotubes and demonstrate TENOM as a powerful tool for investigations of nanostructures. The highest optical resolution up to date with spectroscopic contrast has been achieved using this technique. The enormous signal enhancement allows for the observation of nanotubes that are not detectable by conventional microscopy. My thesis forms the basis for a series of novel experiments. TENOM could be combined with time-resolved techniques such as time-correlated single photon counting (TCSPC) to explore picosecond dynamics in single nanostructures. For electronic applications, conducting nanotubes and nanowires could be probed by a biased tip. In order to clarify the chemical structure of the defects observed in TENOM, high resolution transmission electron microscopy (HRTEM) measurements need to be performed on the same nanotubes.

In the past few years, TENOM has been developed aiming at increasing both spatial resolution and signal enhancement. Standard tapping mode AFM tips have been applied as near-field probes [201], however the signal enhancement is small during the small fraction of its oscillation cycle close to the sample surface. Novel hybrid probes combining AFM tips and optical fibers and metalized AFM tips have been developed to increase the applicability of near-field microscopy [9, 117]. The tip-on-aperture (TOA) probe formed by growing a tiny metal antenna at the end of an aperture probe is used to reduce the background signal associated with far-field laser illumination [202, 203]. Tips with finite length are designed to increase the field enhancement [128–130, 204, 205]. Based on the enormous progress achieved within recent years, I believe that a spatial resolution of few nanometers can be reached and that TENOM develops into more widely used microscopic technique.

References

- [1] D. W. Pohl, W. Denk, and M. Lanz. Optical stethoscopy: Image recording with resolution $\lambda/20$. *Appl. Phys. Lett.*, 44:651–653, 1984.
- [2] A. Lewis, M. Isaacson, A. Harootunian, and A. Muray. Development of a 500 Å resolution light microscope. *Ultramicroscopy*, 13:227–231, 1984.
- [3] E. Betzig and J. K. Trautman. Near-field optics: Microscopy, spectroscopy, and surface modification beyond the diffraction limit. *Science*, 257:189–195, 1992.
- [4] R. C. Dunn. Near-field scanning optical microscopy. *Chem. Rev.*, 99:2891–2928, 1999.
- [5] J. Wessel. Surface-enhanced optical microscopy. *J. Opt. Soc. Am. B*, 2:1538, 1985.
- [6] B. Knoll and F. Keilmann. Near-field probing of vibrational absorption for chemical microscopy. *Nature*, 399:134, 1999.
- [7] E. J. Sánchez, L. Novotny, and X. S. Xie. Near-field fluorescence microscopy based on two-photon excitation with metal tips. *Phys. Rev. Lett.*, 82:4014, 1999.
- [8] S. M. Stöckle, Y. D. Suh, V. Deckert, and R. Zenobi. Nanoscale chemical analysis by tip-enhanced raman spectroscopy. *Chem. Phys. Lett.*, 318:131, 2000.
- [9] N. Hayazawa, Y. Inouye, Z. Sekkat, and S. Kawata. Near-field raman scattering enhanced by a metallized tip. *Chem. Phys. Lett.*, 335:369, 2001.
- [10] A. Hartschuh, E. J. Sánchez, X. S. Xie, and L. Novotny. High-resolution near-field raman microscopy of single-walled carbon nanotubes. *Phys. Rev. Lett.*, 90:095503–095506, 2003.
- [11] A. Hartschuh, M. R. Beversluis, A. Bouhelier, and L. Novotny. Tip-enhanced optical spectroscopy. *Philosophical Transactions: Mathematical, physical and engineering science*, pages 807–819, 2004.
- [12] Kawata, S. and Shalaev, V. M., editor. *Tip enhancement*. Advances in Nano-Optics and Nano-Photonics. Elsevier, Amsterdam, 2007.
- [13] S. Iijima. Helical microtubules of graphitic carbon. *Nature.*, 354:56–58, 1991.
- [14] S. Iijima and T. Ichihashi. Single-shell carbon nanotubes of 1-nm diameter. *Nature.*, 363:603–605, 1993.

- [15] Jorio, A., Dresselhaus, M. S., and Dresselhaus, G., editor. *Carbon Nanotubes*, volume 111 of *Topics in Applied Physics*. Springer, Berlin / Heidelberg, 2008.
- [16] P. Avouris and J. Chen. Nanotube electronic and optoelectronic. *Materials Today*, 9:46–54, 2006.
- [17] W. Lu and C. M. Lieber. Nanoelectronics from the bottom up. *Nat. Mater.*, 6:841–850, 2007.
- [18] D. A. Heller, E. S. Jeng, T.-K. Yeung, B. M. Martinez, A. E. Moll, J. B. Gastala, and M. S. Strano. Optical detection of DNA conformational polymorphism on single-walled carbon nanotubes. *Science*, 311:508–511, 2006.
- [19] K. Welsher, Z. Liu, D. Daranciang, and H. Dai. Selective Probing and Imaging of Cells with Single Walled Carbon Nanotubes as Near-Infrared Fluorescent Molecules. *Nano Lett.*, 8:586–590, 2008.
- [20] H. Jin, D. A. Heller, and M. S. Strano. Single-Particle Tracking of Endocytosis and Exocytosis of Single-Walled Carbon Nanotubes in NIH-3T3 Cells. *Nano. Lett.*, 8:1577–1585, 2008.
- [21] M. J. O’Connell, S. M. Bachilo, C. B. Huffman, V. C. Moore, M. S. Strano, E. H. Haroz, K. L. Rialon, P. J. Boul, W. H. Noon, C. Kittrell, J. Ma, R. H. Hauge, R. .B. Weisman, and R. Smalley. Band gap fluorescence from individual single-walled carbon nanotubes. *Science*, 297:593–596, 2002.
- [22] A. Hagen, M. Steiner, M. B. Raschke, C. Lienau, T. Hertel, H. Qian, A. J. Meixner, and A. Hartschuh. Exponential decay lifetimes of excitons in individual single-walled carbon nanotubes. *Phys. Rev. Lett.*, 95:197401–197404, 2005.
- [23] F. Wang, G. Dukovic, L. E. Brus, and T. F. Heinz. Time-resolved fluorescence of carbon nanotubes and its implication for radiative lifetimes. *Phys. Rev. Lett.*, 92:177401–177404, 2004.
- [24] Y. Z. Ma, J. Stenger, J. Zimmermann, S. M. Bachilo, R. E. Smalley, R. B. Weisman, and G. R. Fleming. Ultrafast carrier dynamics in single-walled carbon nanotubes probed by femtosecond spectroscopy. *J. Chem. Phys.*, 120:3368, 2004.
- [25] F. Wang, G. Dukovic, L. E. Brus, and T. F. Heinz. The optical resonances in carbon nanotubes arise from excitons. *Science*, 308:838–841, 2005.

- [26] J. Maultzsch, R. Pomraenke, S. Reich, E. Chang, D. Prezzi, A. Ruini, E. Molinari, M. S. Strano, C. Thomsen, and C. Lienau. Exciton binding energies in carbon nanotubes from two-photon photoluminescence. *Phys. Rev. B*, 72:241402(R)–241405 (R), 2005.
- [27] S. M. Bachilo, M. S. Strano, C. Kittrell, R. H. Hauge, R. Smalley, and R. .B. Weisman. Structure-assigned optical spectra of single-walled carbon nanotubes. *Science*, 298:2361–2366, 2002.
- [28] A. Hartschuh, H. N. Pedrosa, L. Novotny, and T. D. Krauss. Simultaneous fluorescence and Raman scattering from single carbon nanotubes. *Science*, 301:1354–1356, 2003.
- [29] T. Gokus, H. Harutyunyan, F. Henrich, P. T. Araujo, M. Kappes, A. Jorio, M. Allegrini, A. A. Green, M. C. Hersam, and A. Hartschuh. Exciton decay dynamics in individual carbon nanotubes at room temperature. *Appl. Phys. Lett.*, 92:153116, 2008.
- [30] N. Anderson, A. Hartschuh, and L. Novotny. Nanoscale vibrational analysis of single-walled carbon nanotubes. *J. Am. Chem. Soc.*, 127:2533–2537, 2005.
- [31] N. Anderson, A. Hartschuh, and L. Novotny. Chirality changes in carbon nanotubes studied with near-field Raman spectroscopy. *Nano Lett.*, 7:577–582, 2007.
- [32] H. Htoon, M. J. O’Connell, P. J. Cox, S. K. Doorn, and V. I. Klimov. Low temperature emission spectra of individual single-walled carbon nanotubes: Multiplicity of subspecies within single-species nanotube-ensembles. *Phys. Rev. Lett.*, 93:027401–027404, 2004.
- [33] M. Zheng, A. Jagota, E. D. Semke, B. A. Diner, R. S. Mclean, S. R. Lustig, R. E. Richardson, and N. G. Tassi. DNA-assisted dispersion and separation of carbon nanotubes. *Nat. Mater.*, 2:338–342, 2003.
- [34] C. Fantini, A. A. Jorio, A. P. Santos, V. S. T. Peressinotto, and M. A. Pimenta. Characterization of DNA-wrapped carbon nanotubes by resonance Raman and optical absorption spectroscopies. *Chem. Phys. Lett.*, 439:138–142, 2007.
- [35] M. S. Dresselhaus, G. Dresselhaus, and R. Saito. physics of carbon nanotubes. *Carbon*, 33:883–891, 1995.
- [36] M. S. Dresselhaus, G. Dresselhaus, R. Saito, and A. Jorio. Raman spectroscopy of carbon nanotubes. *Phys. Rep.*, 409:47–99, 2005.

- [37] M. S. Dresselhaus, G. Dresselhaus, and R. Saito. Carbon fibers based on C60 and their symmetry. *Phys. Rev. B.*, 45:6234–6242, 1992.
- [38] R. Saito, G. Dresselhaus, and M. S. Dresselhaus. *Physical Properties of Carbon Nanotubes*. Imperial College Press, London, 1998.
- [39] R. Saito and H. Kataura. *Optical Properties and Raman Spectroscopy of Carbon Nanotubes*, volume 80 of *Carbon Nanotubes, Topics Appl. Physics*. Springer-Verlag, Berlin, Heidelberg, 2001.
- [40] R. A. Jishi, D. Inomata¹, K. Nakao¹, M. S. Dresselhaus, and D. Dresselhaus. Electronic and lattice properties of carbon nanotubes. *J. Phys. Soc. Jpn.*, 63:2252–2260, 1993.
- [41] J. W. Mintmire, D. H. Robertson, and C. T. White. Properties of Fullerene Nanotubes. *J. Phys. Chem. Solids*, 54:1835–1840, 1993.
- [42] J. W. Mintmire and C. T. White. Universal Density of States for Carbon Nanotubes. *Phys. Rev. Lett.*, 81:2056–2059, 1998.
- [43] L. Chico, V. H. Crespi, L. X. Benedict, S. G. Louie, and M. L. Cohen. Pure carbon nanoscale devices: Nanotube heterojunctions. *Phys. Rev. Lett.*, 76:971–974, 1996.
- [44] C. T. White, D. H. Robertson, and J. W. Mintmire. Helical and rotational symmetries of nanoscale graphitic tubules. *Phys. Rev. B.*, 47:5485–5488, 1993.
- [45] R. Saito, M. Fujita, G. Dresselhaus, and M. S. Dresselhaus. Electronic structure of chiral graphene tubules. *Appl. Phys. Lett.*, 60:2204–2206, 1992.
- [46] S. G. Louie. *Electronic Properties, Junctions, and Defects of Carbon Nanotubes*, volume 80 of *Carbon Nanotubes, Topics Appl. Physics*. Springer-Verlag, Berlin, Heidelberg, 2001.
- [47] H. Kataura, Y. Kumazawa, Y. Maniwa, I. Umezu, S. Suzuki, Y. Ohtsuka, and Y. Achiba. Optical Properties of Single-Wall Carbon Nanotubes. *Synthetic Metals*, 103:2555–2558, 1999.
- [48] C. L. Kane and E. J. Mele. Electron interactions and scaling relations for optical excitations in carbon nanotubes. *Phys. Rev. Lett.*, 93:197402, 2004.
- [49] H. Ajiki and T. Ando. Aharonov-Bohm effect in carbon nanotubes. *Physica B*, 201:349–352, 1994.

- [50] H. Ajiki. Magneto-optical spectra of carbon nanotubes: effect of Aharonov-Bohm flux on depolarization effect. *Physica B*, 323:206–208, 2006.
- [51] G. S. Duesberg, I. Loa, M. Burghard, K. Syassen, and S. Roth. Polarized Raman Spectroscopy on Isolated Single-Wall Carbon Nanotubes. *Phys. Rev. Lett.*, 85:5436–5439, 2000.
- [52] M. F. Islam, D. E. Milkie, C. L. Kane, A.G. Yodh, and J.M. Kikkawa. Direct Measurement of the Polarized Optical Absorption Cross Section of Single-Wall Carbon Nanotubes. *Phys. Rev. Lett.*, 93:037404, 2004.
- [53] Y. Miyauchi, M. Oba, and S. Maruyama. Cross-polarized optical absorption of single-walled nanotubes by polarized photoluminescence excitation spectroscopy. *Phys. Rev. B.*, 74:205440, 2006.
- [54] J. Lefebvre and P. Finnie. Excited Excitonic States in Single-Walled Carbon Nanotubes. *Nano Lett.*, pages ASAP Article, 10.1021/nl080518h, 2008.
- [55] M. Menon, E. Richter, and K. R. Subbaswamy. Structural and vibrational properties of fullerenes and nanotubes in a nonorthogonal tight-binding scheme. *J. Chem. Phys.*, 104:5875–5882, 1996.
- [56] O. Dubay and G. Kresse. Accurate density functional calculations for the phonon dispersion relations of graphite layer and carbon nanotubes. *Phys. Rev. B.*, 67:035401, 2003.
- [57] J. Maultzsch, S. Reich, C. Thomsen, H. Requardt, and P. Ordejón. Phonon dispersion in graphite. *Phys. Rev. Lett.*, 92:075501, 2004.
- [58] Ge. G. Samsonidze, R. Saito, A. Jorio, M. A. Pimenta, A. G. Souza Filho, A. Grüneis, G. Dresselhaus, and M. S. Dresselhaus. The Concept of Cutting Lines in Carbon Nanotube Science. *J. Nanosci. Nanotech.*, 3:431–458, 2003.
- [59] M. S. Dresselhaus and P. C. Eklund. Phonons in carbon nanotubes. *Adv. Phys.*, 49:705–814, 2000.
- [60] S. G. Chou, F. Plentz, J. Jiang, R. Saito, D. Nezich, H. B. Ribeiro, A. Jorio, Ge. G. Pimenta, M. A. and Samsonidze, A. P. Santos, M. Zheng, G. B. Onoa, E. D. Semke, G. Dresselhaus, and Dresselhaus M. S. Phonon-assisted excitonic recombination channels observed in dna-wrapped carbon nanotubes using photoluminescence spectroscopy. *Phys. Rev. Lett.*, 94:127402, 2005.

- [61] H. Htoon, M. J. O'Connell, S. K. Doorn, and V. I. Klimov. Single carbon nanotubes probed by photoluminescence excitation spectroscopy: The role of phonon-assisted transitions. *Phys. Rev. Lett.*, 94:127403, 2005.
- [62] X. Qiu, M. Freitag, V. Perebeinos, and Ph. Avouris. Photoconductivity Spectra of Single-Carbon Nanotubes: Implications on the Nature of Their Excited States. *Nano Lett.*, 5:749–752, 2005.
- [63] A. Jorio, R. Saito, J. H. Hafner, C. M. Lieber, M. Hunter, T. McClure, G. Dresselhaus, and M.S. Dresselhaus. Structural (n,m) determination of isolated single-wall carbon nanotubes by resonant raman scattering. *Phys. Rev. Lett.*, 86:1118–1121, 2001.
- [64] P. T. Araujo, I. O. Maciel, P. B. Pesce, M. A. Pimenta, S. K. Doorn, H. Qian, A. Hartschuh, M. Steiner, L. Grigorian, K. Hata, and A. Jorio. The Relation Between Radial Breathing Mode Frequency and Tube Diameter for Pristine Single Wall Carbon Nanotubes and Environmental Effects. *Phys. Rev. B.*, page accepted, 2008.
- [65] A. M. Rao, P. C. Eklund, Sh. Bandow, A. A. Thess, and R. E. Smalley. Evidence for charge transfer in doped carbon nanotube bundles from Raman scattering. *Nature*, 388:257–259, 1997.
- [66] A. Jorio, A. G. Souza Filho, G. Dresselhaus, M. S. Dresselhaus, A. K. Swan, M. S. Ünlü, B. B. Goldberg, M. A. Pimenta, J. H. Hafner, C. M. Lieber, and R. Saito. G-band resonant raman study of 62 isolated single-wall carbon nanotubes. *Phys. Rev. B*, 65:155412, 2002.
- [67] S.D.M. Brown, A. Jorio, P. Corio, M.S. Dresselhaus, R. Saito, and K. Kneipp. Origin of the Breit- Wigner-Fano lineshape of the tangential G-band feature of metallic carbon nanotubes. *Phys. Rev. B.*, 63:155414, 2001.
- [68] S. Piscanec, M. Lazzeri, J. Robertson, A. C. Ferrari, and F. Mauri. Optical phonons in carbon nanotubes: Kohn anomalies, Peierls distortions, and dynamic effects. *Phys. Rev. B.*, 75:035427, 2007.
- [69] C. Thomsen and S. Reich. Double resonant raman scattering in graphite. *Phys. Rev. Lett.*, 85:5214–5217, 2000.
- [70] R. P. Vidano, D. B. Fischbach, L. J. Willis, and T. M. Loehr. Observation of Raman band shifting with excitation wavelength for carbons and graphite. *Solid state communication*, 39:341–344, 1981.

- [71] S. Reich, C. Thomsen, and J. Maultzsch. *Carbon Nanotubes: Basic Concepts and Physical Properties*. Wiley-VCH, Berlin, 2004.
- [72] E. Chang, G. Bussi, A. Ruini, and E. Molinari. Excitons in carbon nanotubes: An ab initio symmetry-based approach. *Phys. Rev. Lett.*, 92:196401, 2004.
- [73] C. D. Spataru, S. Ismail-Beigi, L. X. Benedict, and S. G. Louie. Excitonic effects and optical spectra of single-walled carbon nanotubes. *Phys. Rev. Lett.*, 92:077402–077405, 2004.
- [74] J. Maultzsch, R. Pomraenke, S. Reich, E. Chang, D. Prezzi, A. Ruini, E. Molinari, M. S. Strano, C. Thomsen, and C. Lienau. Exciton binding energies in carbon nanotubes from two-photon photoluminescence. *Phys. Rev. B*, 72:241402(R)–241405(R), 2005.
- [75] G. Dukovic, F. Wang, D. Song, M. Y. Sfeir, T. F. Heinz, and L. E. Brus. Structural Dependence of Excitonic Optical Transitions and Band-Gap Energies in Carbon Nanotubes. *Nano Lett.*, 5:2314–2318, 2005.
- [76] V. Perebeinos, J. Tersoff, and Ph. Avouris. Scaling of excitons in carbon nanotubes. *Phys. Rev. Lett.*, 92:257402–257405, 2004.
- [77] A. G. Walsh, A. N. Vamivakas, Y. Yin, S. B. Cronin, M. S. Ünlü, B. B. Goldberg, and A. K. Swan. Screening of Excitons in Single, Suspended Carbon Nanotubes. *Nano Lett.*, 7:1485–1488, 2007.
- [78] O. Kiowski, S. Lebedkin, F. Hennrich, S. Malik, H. Rsnér, K. Arnold, C. Srgers, and M. M. Kappes. Photoluminescence microscopy of carbon nanotubes grown by chemical vapor deposition: Influence of external dielectric screening on optical transition energies. *Phys. Rev. B*, 75:075421, 2007.
- [79] Y. Ohno, S. Iwasaki, Y. Murakami, S. Kishimoto, S. Maruyama, and T. Mizutani. Chirality-dependent environmental effects in photoluminescence of single-walled carbon nanotubes. *Phys. Rev. B*, 73:235427, 2006.
- [80] J. H. Choi and M. S. Strano. Solvatochromism in single-walled carbon nanotubes. *Appl. Phys. Lett.*, 90:223114, 2007.
- [81] J. Jiang, R. Saito, Ge. G. Samsonidze, A. Jorio, S. G. Chou, G. Dresselhaus, and M. S. Dresselhaus. Chirality dependence of exciton effects in single-wall carbon nanotubes: Tight-binding model. *Phys. Rev. B*, 75:035407, 2007.

- [82] L. Cognet, D. T. Tysboulski, J.-D. R. Rocha, C. D. Doyle, J. M. Tour, and R. B. Weisman. Stepwise quenching of exciton fluorescence in carbon nanotubes by single-molecule reactions. *Science*, 316:1465–1468, 2007.
- [83] C. Georgi, N. Hartmann, T. Gokus, A. A. Green, M. C. Hersam, and A. Hartschuh. Photo-induced luminescence blinking and bleaching in individual Single-Walled Carbon Nanotubes. *Chem. Phys. Chem.*, doi:10.1002/cphc.20080079, 2008.
- [84] J. Crochet, M. Clemens, and T. Hertel. Quantum Yield Heterogeneities of Aqueous Single-Wall Carbon Nanotube Suspensions. *J. Am. Chem. Soc.*, 129:8058–8059, 2007.
- [85] J. Lefebvre, D. G. Austing, J. Bond, and P. Finnie. Photoluminescence imaging of suspended single-walled carbon nanotubes. *Nano Lett.*, 6:1603–1608, 2006.
- [86] A. Rajan, M. S. Strano, D. A. Heller, T. Hertel, and K. Schulten. Length-Dependent Optical Effects in Single Walled Carbon Nanotubes. *J. Phys. Chem. B*, 112(19):6211–3, 2008.
- [87] H. Qian, C. Georgi, N. Anderson, A. A. Green, M. C. Hersam, L. Novotny, and A. Hartschuh. Exciton transfer and propagation in carbon nanotubes studied by near-field optical microscopy. *physica status solidi*, page submitted for publication, 2008.
- [88] A. Thess, R. Lee, P. Nikolaev, H. Dai, P. Petit, J. Robert, C. Xu, Y. H. Lee, S. G. Kim, A. G. Rinzler, D. T. Colbert, G. E. Scuseria, D. Tomanek, J. E. Fischer, and R. E. Smalley. Crystalline Ropes of Metallic Carbon Nanotubes. *Science*, 273:483–487, 1996.
- [89] M. Zheng, A. Jagota, M. S. Strano, A. P. Santos, P. Barone, S. G. Chou, B. A. Dinder, M. S. Dresselhaus, R. S. Mclean, G. B. Onoa, G. G. Samsonidze, E. D. Semke, M. Usrey, and D. J. Walls. Structure-based carbon nanotube sorting by sequence-dependent dna assembly. *Science*, 302:1545, 2003.
- [90] M. S. Arnold, S. I. Stupp, and M. C. Hersam. Enrichment of single-walled carbon nanotubes by diameter in density gradients. *Nano Lett.*, 5:713–718, 2005.
- [91] M. S. Arnold, A. A. Green, J. F. Hulvat, S. I. Stupp, and M. C. Hersam. Sorting carbon nanotubes by electronic structure using density differentiation. *Nature Nanotechnology*, 1:60–65, 2006.
- [92] A. A. Green and M. C. Hersam. Ultracentrifugation of single-walled nanotubes. *Materials Today*, 10:59–60, 2007.

- [93] R. R. Johnson, A. T. Charlie Johnson, and M. L. Klein. Probing the Structure of DNA-Carbon Nanotube Hybrids with Molecular Dynamics. *Nano Lett.*, 8:69–75, 2008.
- [94] S. Manohar, T. Tang, and A Jagota. Structure of Homopolymer DNA-CNT Hybrids. *J. Phys. Chem. C*, 111:17835–17845, 2007.
- [95] H. Jin, E. S. Jeng, D. A. Heller, P. V. Jena, R. Kirmse, J. Langowski, and M. S. Strano. Divalent Ion and Thermally Induced DNA Conformational Polymorphism on Single-walled Carbon Nanotubes. *Macromolecules*, 40:6731–6739, 2007.
- [96] S. Malik, S. Vogel, H. Rösner, K. Arnold, F. Hennrich, A-K. Köhler, C. Richert, and M. M. Kappes. Physical chemical characterization of DNASWNT suspensions and associated composites. *Composites Science and Technology*, 67:916–921, 2007.
- [97] D. A. Heller, S. Baik, T. E. Eurell, and M. S. Strano. Single-walled carbon nanotube spectroscopy in live cells: Towards long-term labels and optical sensors. *Adv. Mater.*, 17:2793–2799, 2006.
- [98] P. J. Michalski and E. J. Mele. Carbon nanotubes in helically modulated potentials. *Phys. Rev. B.*, 77:085429, 2008.
- [99] V. I. Puller and S. V. Rotkin. Helicity and broken symmetry of DNA-nanotube hybrids. *Europhys. Lett.*, 77:27006, 2007.
- [100] E. S. Jeng, A. E. Moll, A. C. Roy, J. B. Gastala, and M. S. Strano. Detection of DNA Hybridization Using the Near-Infrared Band-Gap Fluorescence of Single-Walled Carbon Nanotubes. *Nano Lett.*, 6:371–375, 2006.
- [101] S.G. Chou, H.B. Ribeiro, E.B. Barros, A.P. Santos, D. Nezich, Ge.G. Samsonidze, C. Fantin, M.A. Pimenta, A. Jorio, F. Plentz Filho, M.S. Dresselhaus, G. Dresselhaus, R. Saito, M. Zheng, G.B. Onoa, E.D. Semke, A.K. Swan, M. S. Ünlü, and B.B. Goldberg. Optical characterization of DNA-wrapped carbon nanotube hybrids. *Chem. Phys. Lett.*, 397:296–301, 2004.
- [102] Novotny, L. and Hecht, B. *Principles of nano-optics*. Cambridge University Press, Cambridge, 2006.
- [103] S. W. Hell. Far-Field Optical Nanoscopy. *Science*, 316:1153–1158, 2007.

- [104] J.-J. Greffet and R. Carminati. Image formation in near-field optics. *Progress in Surface Science*, 56:133–237, 1997.
- [105] A. Yildiz, J. N. Forkey, S. A. McKinney, T. Ha, Y. E. Goldman, and P. R. Selvin. Myosin V Walks Hand-Over-Hand: Single Fluorophore Imaging with 1.5-nm Localization. *Science*, 300:2061–2065, 2003.
- [106] R. E. Thompson, D. R. Larson, and W. W. Webb. Precise Nanometer Localization Analysis for Individual Fluorescent Probes. *Biophys. J.*, 82:2775–2783, 2002.
- [107] R. J. Ober, S. Ram, and E. S. Ward. Localization Accuracy in Single-Molecule Microscopy. *Biophys. J.*, 86:1185–1200, 2004.
- [108] N. Bobroff. Position measurement with a resolution and noise-limited instrument. *Rev. Sci. Instrum.*, 57:1152–1157, 1986.
- [109] S. W. Hell and J. Wichmann. Breaking the diffraction resolution limit by stimulated emission: stimulated-emission-depletion fluorescence microscopy. *Optics Letters*, 19:780–782, 1994.
- [110] E. Betzig, G. H. Patterson, R. O. Sougrat, W. Lindwasser, S. Olenych, J. S. Bonifacino, M. W. Davidson, J. Lippincott-Schwartz, and H. F. Hess. Imaging Intracellular Fluorescent Proteins at Nanometer Resolution. *Science*, 313:1642–1645, 2006.
- [111] M. J. Rust, M. Bates, and X. Zhuang. Sub-diffraction-limit imaging by stochastic optical reconstruction microscopy (STORM). *Nature Methods*, 3:793–796, 2006.
- [112] M. Orrit and J. Bernard. Single Pentacene Molecules Detected by Fluorescence Excitation in a p-Terphenyl Crystal. *Phys. Rev. Lett.*, 65:2716–2719, 1990.
- [113] L. Novotny and C. Hafner. Light propagation in a cylindrical waveguide with a complex, metallic, dielectric function. *Phys. Rev. E.*, 50:4094–4106, 1994.
- [114] L. Novotny and D. W. Pohl. Light propagation in scanning near-field optical microscopy. *NATO Adv. Stud. Inst. E*, 184:21–33, 1995.
- [115] E. Betzig, P. L. Finn, and J. S. Weiner. Combined shear force and near-field scanning optical microscopy. *Appl. Phys. Lett.*, 60:2484–2486, 1992.
- [116] X. S. Xie and R. C. Dunn. Probing Single Molecule Dynamics. *Science*, 265:361–364, 1994.

- [117] L. K. Kapkiai, D. Moore-Nichols, J. Carnell, J. R. Krogmeier, and R. C. Dunn. Hybrid near-field scanning optical microscopy tips for live cell measurements. *Appl. Phys. Lett.*, 84:3750–3752, 2004.
- [118] R. Kersting, H.T. Chen, N. Karpowicz, and G.C. Cho. Terahertz microscopy with submicron resolution. *J. Opt A*, 7:184–189, 2005.
- [119] R. Kersting, F. F. Bürsgens, G. Acuna, and G. C. Cho. *Advances in Solid State Physics*. Springer Verlag, Berlin Heidelberg New York, 2008.
- [120] R. Hillenbrand and F. Keilmann. Material-specific mapping of metal/semiconductor/dielectric nanosystems at 10 nm resolution by backscattering near-field optical microscopy. *Appl. Phys. Lett.*, 80:25–27, 2002.
- [121] J. Gersten and A. Nitzan. Spectroscopic properties of molecules interacting with small dielectric particles. *J. Chem. Phys.*, 75:1139–1152, 1981.
- [122] R. Ruppin. Decay of an excited molecule near a small metal sphere. *J. Chem. Phys.*, 76:1681–1684, 1982.
- [123] A. Bouhelier, M. Beversluis, A. Hartschuh, and L. Novotny. Near-field second-harmonic generation induced by local field enhancement. *Phys. Rev. Lett.*, 90:013903, 2003.
- [124] L. Novotny, R. X. Bian, and X. S. Xie. Theory of nanometric optical tweezers. *Phys. Rev. Lett.*, 79:645–648, 1997.
- [125] L. Novotny, E. J. Sánchez, and X. S. Xie. Near-field optical imaging using metal tips by higher-order hermite-gaussian beams. *Ultramicroscopy*, 71:21–29, 1998.
- [126] R. E. Larsen and H. Metiu. Resolution and polarization in apertureless near-field microscopy. *J. Chem. Phys.*, 114:6851, 2001.
- [127] Y. C. Martin, H. F. Hamann, and H. K. Wickramasinghe. Strength of the electric field in apertureless near-field optical microscopy. *J. Appl. Phys.*, 89:5774–5778, 2001.
- [128] J. T. I. Krug, E. J. Sánchez, and X. S. Xie. Design of near-field probes with optimal field enhancement by finite difference time domain electromagnetic simulation. *J. Chem. Phys.*, 116:10895–10901, 2002.
- [129] L. Novotny. Effective Wavelength Scaling for Optical Antennas. *Phys. Rev. Lett.*, 98:266802, 2007.

- [130] R. Kappeler, D. Erni, C. Xudong, and L. Novotny. Field Computations of Optical Antennas. *J. Comp. Theor. Nanosc.*, 4:686–691, 2007.
- [131] C. Sönnichsen, T. Franzl, T. Wilk, G. von Plessen, and J. Feldmann. Drastic Reduction of Plasmon Damping in Gold Nanorods. *Phys. Rev. Lett.*, 88:077402, 2002.
- [132] S. Nie and S. R. Emory. Probing single molecules and single nanoparticles by surface-enhanced raman scattering. *Science*, 275:1102, 1997.
- [133] J. Steidtner and B. Pettinger. Tip-Enhanced Raman Spectroscopy and Microscopy on Single Dye Molecules with 15 nm Resolution. *Phys. Rev. Lett.*, 100:236101, 2008.
- [134] A. Hartschuh, M. R. Beversluis, A. Bouhelier, and L. Novotny. Tip-enhanced optical spectroscopy. *Phil. Trans. R. Soc. Lond. A.*, 362:807–819, 2004.
- [135] L. T. Nieman, G. M. Krampert, and R. E. Martinez. An apertureless near-field scanning optical microscope and its application to surface-enhanced raman spectroscopy and multiphoton fluorescence imaging. *Rev. Sci. Instrum.*, 72:1691, 2001.
- [136] N. Hayazawa et al. Near-field raman imaging of organic molecules by an apertureless metallic probe scanning optical microscope. *J. Chem. Phys.*, 117:1296, 2002.
- [137] B. Pettinger, B. Ren, G. Picardi, R. Schuster, and G. Ertl. Tip-enhanced Raman spectroscopy (TERS) of malachite green isothiocyanate at Au(111): bleaching behavior under the influence of high electromagnetic fields. *J. Raman Spectrosc.*, 36:541–550, 2005.
- [138] B. Pettinger, B. Ren, G. Picardi, R. Schuster, and G. Ertl. Nanoscale probing of adsorbed species by tip-enhanced Raman spectroscopy. *Phys. Rev. Lett.*, 92:096101, 2004.
- [139] A. Hartschuh, H. Qian, A. J. Meixner, N. Anderson, and L. Novotny. Tip-enhanced optical spectroscopy for surface analysis in biosciences. *Surf. Int. Anal.*, 38:1472–1480, 2006.
- [140] S. Kühn, U. Hakanson, L. Rogobete, and V. Sandoghdar. Enhancement of single molecule fluorescence using a gold nanoparticle as an optical nano-antenna. *Phys. Rev. Lett.*, 97:017402–017405, 2006.
- [141] M. Ringler, A. Schwemer, M. Wunderlich, A. Nichtl, K. Kürzinger, T. A. Klar, and J. Feldmann. Shaping Emission Spectra of Fluorescent Molecules with Single Plasmonic Nanoresonators. *Phys. Rev. Lett.*, 100:203002, 2008.

- [142] T. Kalkbrenner, U. Håkanson, A. A. Schädle, S. Burger, C. Henkel, and V. Sandoghdar. Optical Microscopy via Spectral Modifications of a Nanoantenna. *Phys. Rev. Lett.*, 95:200801, 2005.
- [143] R. R. Chance, A. Prock, and R. Silbey. Lifetime of an emitting molecule near a partially reflecting surface. *J. Chem. Phys.*, 60:2744–2748, 1974.
- [144] W. L. Barnes. Fluorescence near interfaces: the role of photonic mode density. *J. Mod. Opt.*, 45:661–699, 1998.
- [145] N. A. Issa and R. Guckenberger. Fluorescence near metal tips: The roles of energy transfer and surface plasmon polaritons . *Optics Express*, 15:12131–12144, 2007.
- [146] M. Thomas, R. Carminati, J. R. Arias-Gonzalez, and J.-J. Greffet. Single-molecule spontaneous emission close to absorbing nanostructures. *Appl. Phys. Lett.*, 85:3863–3865, 2004.
- [147] L. Rogobete, F. Kaminski, M. Agio, and V. Sandoghdar. Design of plasmonic nanoantennae for enhancing spontaneous emission. *Optics Letters*, 32:1623–1625, 2007.
- [148] P. Anger, P. Bharadwaj, and L. Novotny. Enhancement and quenching of single molecule fluorescence. *Phys. Rev. Lett.*, 96:113002–113006, 2006.
- [149] P. Bharadwaj, P. Anger, and L. Novotny. Nanoplasmonic enhancement of single molecule fluorescence. *Nanotechnology*, 18:044017–044022, 2007.
- [150] K. Karrai and R. D. Grober. Piezoelectric tip-sample distance control for near field optical microscopes. *Appl. Phys. Lett.*, 66:1842–1844, 1995.
- [151] T. R. Albrecht, P. Grütter, D. Horne, and D. Rugar. Frequency modulation detection using highd cantilevers for enhanced force microscope sensitivity. *J. Appl. Phys.*, 69:668–673, 200.
- [152] S. Quabis, R. Dorn, O. Glöckl, M. Eberler, and G. Leuchs. Focusing light to a tighter spot. *Opt. Comm.*, 179:1–, 2000.
- [153] A. J. Nam, A. Teren, T. A. Lusby, and A. J. Melmed. Benign making of sharp tips for STM and FIM: Pt, Ir, Au, Pd, and Rh. *J. Vac. Sci. Technol. B*, 13:1556–1559, 1995.
- [154] M. R. Beversluis, A. Bouhelier, and L. Novotny. Continuum generation from single gold nanostructures through near-field mediated intraband transitions. *Phys. Rev. B.*, 68:115433, 2003.

- [155] A. Hartschuh, N. Anderson, and L. Novotny. Near-field raman spectroscopy using a sharp metal tip. *J. Microscopy.*, 210:234, 2003.
- [156] L. Billot, L. Berguiga, M. L. De la Chapellea, Y. Gilbert, and R. Bachelot. Production of gold tips for tip-enhanced near-field optical microscopy and spectroscopy: analysis of the etching parameters. *Eur. Phys. J. Appl. Phys.*, 31:139–145, 2005.
- [157] S. M. Bachilo, L. Balzano, J. E. Herrera, F. Pompeo, D. E. Resasco, and R. .B. Weisman. Narrow (n,m)-distribution of single-walled carbon nanotubes grown using a solid supported catalyst. *J. Am. Chem. Soc.*, 125:11186–11187, 2003.
- [158] I. O. Maciel, N. Anderson, M. A. Pimenta, A. Hartschuh, H. Qian, M. Terrones, H. Terrones, J. Campos-Delgado, A. M. Rao, L. Novotny, and A. Jorio. Electron and phonon renormalization at defect/doping sites in carbon nanotubes. *Nature Mater.*, page Submitted for publication, 2008.
- [159] W. Zhou, Y. H. Ooi, R. Russo, P. Papanek, D. E. Luzzi, J. E. Fischer, M. J. Bronikowski, P. A. Willis, and R. E. Smalley. Structural characterization and diameter-dependent oxidative stability of single wall carbon nanotubes synthesized by the catalytic decomposition of CO. *Chem. Phys. Lett.*, 350:6–14, 2001.
- [160] H. Qian, C. Georgi, N. Anderson, A. A. Green, M. C. Hersam, L. Novotny, and A. Hartschuh. Exciton Energy Transfer in Pairs of Single-Walled Carbon Nanotubes. *Nano Lett.*, 8(5):1363–1367, 2008.
- [161] H. Qian, C. Georgi, T. Gokus, N. Hartmann, A. A. Green, M. C. Hersam, L. Novotny, and A. Hartschuh. "Visualizing the Local Optical Response of Semiconducting Carbon Nanotubes to DNA-wrapping. *Nano Lett.*, accepted, 2008.
- [162] M. T. Woodside and P. L. McEuen. Scanned Probe Imaging of Single-Electron Charge States in Nanotube Quantum Dots. *Science*, 296:1098–1101, 2002.
- [163] P. L. McEuen, M. Bockrath, D. H. Cobden, Y. G. Yoon, and S. G. Louie. Disorder, pseudospins, and backscattering in carbon nanotubes. *Phys. Rev. Lett.*, 83:5098–5101, 1999.
- [164] J. A. Fagan, J. R. Simpson, B. J. Bauer, S H. De Paoli Lacerda, M. L. Becker, J. Chun, K. B. Migler, A. R. Hight Walker, and Hobbie E. K. Length-Dependent Optical Effects in Single-Wall Carbon Nanotubes. *J. Am. Chem. Soc.*, 129:10607–10612, 2007.

- [165] A. Hartschuh, H. Qian, A. J. Meixner, N. Anderson, and L. Novotny. Nanoscale optical imaging of excitons in single-walled carbon nanotubes. *Nano Lett.*, 5:2310–2313, 2005.
- [166] S. J. Tans and C. Dekker. Potential modulations along carbon nanotubes. *Nature.*, 404:834–835, 2000.
- [167] N. Mason, M. J. Biercuk, and C. M. Marcus. Local Gate Control of a Carbon Nanotube Double Quantum Dot. *Science*, 303:655–658, 2004.
- [168] M. Bockrath, W. Liang, D. Bozovic, J. H. Hafner, C. M. Lieber, M. Tinkham, and H. Park. Resonant electron scattering by defects in single-walled carbon nanotubes. *Science*, 291:283–285, 2001.
- [169] H. Hirori, K. Matsuda, Y. Miyauchi, S. Maruyama, and Y. Kanemitsu. Exciton Localization of Single-Walled Carbon Nanotubes Revealed by Femtosecond Excitation Correlation Spectroscopy. *Phys. Rev. Lett.*, 97:257401, 2006.
- [170] H. Zhao and S. Mazumdar. Electron-electron interaction effects on the optical excitations of semiconducting single-walled carbon nanotubes. *Phys. Rev. Lett.*, 93:157402–157405, 2004.
- [171] S. Reich, C. Thomsen, and J. Robertson. Exciton resonances quench the photoluminescence of zigzag carbon nanotubes. *Phys. Rev. Lett.*, 95:077402–077405, 2005.
- [172] F. Wang, G. Dukovic, E. Knoesel, L. E. Brus, and T. F. Heinz. Observation of rapid auger recombination in optically excited semiconducting carbon nanotubes. *Phys. Rev. B*, 70:241403, 2004.
- [173] V. Vasili Perebeinos and Ph. Avouris. Phonon and Electronic Non-radiative Decay of Excitons in Carbon Nanotubes. *cond. Mat. arXiv:0804.0767v2*, 2008.
- [174] J. Lefebvre, D. G. Austing, J. Bond, and P. Finnie. Photoluminescence imaging of suspended single-walled carbon nanotubes. *Nano Lett.*, 6:1603–1608, 2006.
- [175] M. A. Pimenta, G. Dresselhaus, M. S. Dresselhaus, L. G. Cancado, A. Jorio, and R. Saito. Studying disorder in graphite-based systems by Raman spectroscopy. *Phys. Chem. Chem. Phys.*, 9:1276–1291, 2006.
- [176] S. K. Doorn, M. J. O’Connell, L. Zheng, Y. T. Zhu, S. Huang, and J. Liu. Raman spectral imaging of a carbon nanotube intramolecular junction. *Phys. Rev. Lett.*, 94:016802–016805–, 2005.

- [177] Y. A. Kim, H. Muramatsu, T. Hayashi, M. Endo, M. Terrones, and M.S. Dresselhaus. Thermal stability and structural changes of double-walled carbon nanotubes by heat treatment. *Chem. Phys. Lett.*, 398:87–92, 2004.
- [178] H. G. Frey, S. Witt, K. Felderer, and R. Guckenberger. High-resolution imaging of single fluorescent molecules with the optical near-field of a metal tip. *Phys. Rev. Lett.*, 93:200801–200804, 2004.
- [179] H. Zhao and S. Mazumdar. Electron-Electron Interaction Effects on the Optical Excitations of Semiconducting Single-Walled Carbon Nanotubes. *Phys. Rev. Lett.*, 93:157402, 2004.
- [180] S. Uryu and T. Ando. Exciton absorption of perpendicularly polarized light in carbon nanotubes. *Phys. Rev. B.*, 74:155411, 200.
- [181] E. Dulkeith, M. Ringler, T. A. Klar, and J. Feldmann. Gold Nanoparticles Quench Fluorescence by Phase Induced Radiative Rate Suppression. *Nano. Lett.*, 5:585–589, 2005.
- [182] J. Azoulay, A. Débarre, A. Richard, and P. Tchénio. Quenching and enhancement of single-molecule fluorescence under metallic and dielectric tips. *Europhys. Lett.*, 51:374–380, 2000.
- [183] P. W. Barone, S. Baik, D. A. Heller, and M. S. Michael, S. STRANO. Near-infrared optical sensors based on single-walled carbon nanotubes. *Nat. Mater.*, 4:86–92, 200.
- [184] L. Cognet, D. A. Tsybouski, J. D. R. Rocha, C. D. Doyle, J. M. Tour, and R. B. Weisman. Stepwise Quenching of Exciton Fluorescence in Carbon Nanotubes by Single-Molecule Reactions. *Science*, 316:1465–1468, 2008.
- [185] T. Hertel, R. Fasel, and G. Moos. Charge-carrier dynamics in single-wall carbon nanotube bundles: a time-domain study. *Appl. Phys. A*, 75:449–465, 2002.
- [186] S. Reich, M. Dworzak, A. Hoffmann, C. Thomsen, and M. S. Strano. Excited-state carrier lifetime in single-walled carbon nanotubes. *Phys. Rev. B*, 71:033402, 2005.
- [187] P. H. Tan, A. G. Rozhin, P. Hu, V. Scardaci, W. I. Milne, and A. C. Ferrari. Photoluminescence spectroscopy of carbon nanotube bundles: Evidence for exciton energy transfer. *Phys. Rev. Lett.*, 99:137402–4, 2007.

- [188] O. N. Torrens, D. E. Milkie, and J. M. Kikkawa. Photoluminescence from intertube carrier migration in single-walled carbon nanotubes. *Nano Lett.*, 6:2864–2867, 2006.
- [189] O. Kiowski, K. Arnold, S. Lebedkin, F. Hennrich, and M. M. Kappes. Direct Observation of Deep Excitonic States in the Photoluminescence Spectra of Single-Walled Carbon Nanotubes. *Phys. Rev. Lett.*, 99:237402, 2007.
- [190] M. Jones, W. K. Metzger, T. J. McDonald, C. Engtrakul, R. J. Ellingson, G. Rumbles, and M. J. Heben. Extrinsic and intrinsic effects on the excited-state kinetics of single-walled carbon nanotubes. *Nano Lett.*, 7:300–306, 2007.
- [191] F. Plentz, H. B. Ribeiro, A. Jorio, M. S. Strano, and M. A. Pimenta. Direct Experimental Evidence of Exciton-Phonon Bound States in Carbon Nanotubes. *Phys. Rev. Lett.*, 95:247401, 2005.
- [192] A. Yildiz, M. Tomishige, R. D. Vale, and P. R. Selvin. Kinesin walks hand-over-hand. *Science*, 303:676–678, 2004.
- [193] T. Heinlein, A. Biebricher, P. Schlüter, Roth C. M., D. P. Herten, J. Wolfrum, M. Heilemann, C. Müller, P. Tinnefeld, and M. Sauer. High-resolution colocalization of single molecules within the resolution gap of far-field microscopy. *Chem. Phys. Chem.*, 6:949–955, 2005.
- [194] B. Bourlon, C. Miko, L. Forro, D. C. Glatzli, and A. Bachtold. Determination of the Intershell Conductance in Multiwalled Carbon Nanotubes. *Phys. Rev. Lett.*, 93:176806–4, 2004.
- [195] I. V. Bondarev, G. Ya. Slepian, and S. A. Maksimenko. Spontaneous decay of excited atomic states near a carbon nanotube. *Phys. Rev. Lett.*, 89:115504–115507, 2002.
- [196] L. J. Carlson, S. E. Maccagnano, J. Silcox, and T. D. Krauss. Fluorescence efficiency of individual carbon nanotubes. *Nano Lett.*, pages –, 2007.
- [197] A. De Vita, J. Ch. Charlier, X. Blase, and R. Car. Electronic structure at carbon nanotube tips. *Appl. Phys. A*, 68:283–286, 1999.
- [198] D. L. Carroll, P. Redlich, P. M. Ajayan, J. Ch. Charlier, X. Blase, A. De Vita, and R. Car. Electronic Structure and Localized States at Carbon Nanotube Tips. *Phys. Rev. Lett.*, 78:2811–2814, 1997.

- [199] Ph. Kim, T. W. Odom, J. Huang, and C. M. Lieber. Electronic density of states of atomically resolved single-walled carbon nanotubes: Van hove singularities and end states. *Phys. Rev. Lett.*, 82:1225–1228, 1999.
- [200] L. C. Venema, J. W. Janssen, M. R. Buitelaar, J. W. G. Wildöer, S. G. Lemay, L. P. Kouwenhoven, and C. Dekker. Spatially resolved scanning tunneling spectroscopy on single-walled carbon nanotubes. *Phys. Rev. B.*, 62:5238–5244, 2000.
- [201] C. Xie, C. Mu, J. R. Cox, and J. M. Gerton. Tip-enhanced fluorescence microscopy of high-density samples. *App. Phys. Lett.*, 89:143117, 2006.
- [202] H. G. Frey, F. Keilmann, A. Kriele, and R. Guckenberger. Enhancing the resolution of scanning near-field optical microscopy by a metal tip grown on an aperture probe. *Appl. Phys. Lett.*, 81:530–532, 2002.
- [203] . pages –, 200.
- [204] P. Mühlischlegel, H.-J. Eisler, B. Hecht, and D. W. Pohl. Resonant optical antennas. *Science*, 308:1607–1609, 2005.
- [205] T. H. Taminiau, F. D. Stefani, F. B. Segerink, and N. F. Van Hulst. Optical antennas direct single-molecule emission. *Nature Photonics*, 2:234–237, 2008.
- [206] K. S. Novoselov, A. K. Geim, S. V. Morozov, D. Jiang, Y. Zhang, S. V. Dubonos, I. V. Grigorieva, and A. A. Firsov. Electric Field Effect in Atomically Thin Carbon Films. *Science*, 306:666–669, 2004.
- [207] K. S. Novoselov, D. Jiang, F. Schedin, T. J. Booth, V. V. Khotkevich, and S. V. Morozov. Two-dimensional atomic crystals. *Proc. Natl. Acad. Sci. U.S.A.*, 102:10451–10453, 2005.
- [208] C. Casiraghi, A. Hartschuh, E. Lidorikis, H. Qian, H. Harutyunyan, T. Gokus, K. S. Novoselov, and A. Ferrari. Rayleigh imaging of graphene and graphene Layers. *Nano. Lett.*, 7:2711–2717, 2007.
- [209] Z. H. Ni, H. M. Wang, J. Kasim, H. M. Fan, T. Yu, Y. H. Wu, Y. P. Feng, and Z. X. Shen. Graphene Thickness Determination Using Reflection and Contrast Spectroscopy. *Nano. Lett.*, 7:2758–2763, 2007.
- [210] L. G. Cancado, M. A. Pimenta, B. R. A. Neves, M. S. S. Dantas, and A. Jorio. Influence of the atomic structure on the Raman spectra of graphite edges. *Phys. Rev. Lett.*, 93:247401–247404, 2004.

- [211] A. C. Ferrari, J. C. Meyer, V. Scardaci, C. Casiraghi, M. Lazzeri, F. Mauri, S. Piscanec, D. Jiang, K. S. Novoselov, S. Roth, and A. K. Geim. Raman Spectrum of Graphene and Graphene Layers. *Phys. Rev. Lett.*, 97:187401, 2006.
- [212] P. J. Schuck, D. P. Fromm, A. Sundaramurthy, G. S. Kino, and W. E. Moerner. Improving the Mismatch between Light and Nanoscale Objects with Gold Bowtie Nanoantennas. *Phys. Rev. Lett.*, 94:017402, 2005.
- [213] H. Fischer and O. J. F. Martin. Engineering the optical response of plasmonic nanoantennas. *Optics Express*, 16:9144–9154, 2008.
- [214] F. Jäckel, A. A. Kinkhabwala, and W. E. W. E. Moerner. Gold bowtie nanoantennas for surface-enhanced Raman scattering under controlled electrochemical potential. *Chem. Phys. Lett.*, 446:339–343, 2007.

A Near-field measurement on graphite and graphene

Graphene is a two-dimensional (2D) crystal structure, which is the basic structure for building other sp^2 carbon nanomaterials, such as nanographite sheets and carbon nanotubes. Graphene has peculiar electronic properties, as described in section 2.2, the conduction band and the valence band touch at the K point in the hexagonal Brillouin zone at the Fermi level. In the vicinity of these points, the electron energy has a linear relationship with the wavevector, where the electrons are like massless Dirac-Fermions [38].

Recently, high quality graphene samples have been obtained from micromechanical cleavage of graphite [206, 207]. Even a monolayer graphene becomes visible on an oxidized Si substrate as it adds up sufficiently to the optical path of reflected light so that the interference color changes with respect to the substrate (phase contrast) [206–209]. Besides the atomic force microscopy (AFM) [206, 207], both Raman and Rayleigh scattering have been proved as a quick and precise method for determining the number of graphene layers without destroying the crystal lattice [208, 209]. Confocal Raman measurements on graphite reveals strong defect-induced D-band mode at the edge [175, 210]. High resolution TENOM propose the study on the spatial extent of D-mode at the edge of graphite and graphene.

The micromechanical cleavage method was applied on the transparent glass cover slide substrate for TENOM setup. The laser excitation source used is HeNe laser at 632.8 nm. The signals detected are Raman G-band and D-band by two APDs followed by two bandpass filter centered at 700 nm and 690 nm, respectively. Mostly, we can observe the multilayer graphite easily, because the Raman G-band of a single sheet of graphene appears extremely weak to be visualized. Figure 55 displays the confocal Raman images of a HOPG (highly ordered pyrolytic graphite) crystallite deposited on a glass. As expected, the G-band signal appears all over the graphite originating from C-C stretching, while the D-band occurs only at the edge. The spectra taken at two positions, one in the interior of the crystallite marked with number 1, and the other at the edge marked with number 2, clearly reveal that the defects rich graphite edge gives rise of the D-band, can also be distinguished from the corresponding spectrum 1 and 2 in Figure 55(c). The strong D-band signal at the graphite edge observed here is in agreement with [175, 210], that has been studied for characterization of the crystallographic orientation of atoms near the edge.

Based on the confocal information, near-field measurements at the edge were performed aiming at the defects extension as well as G-band information at the edge. The first results were

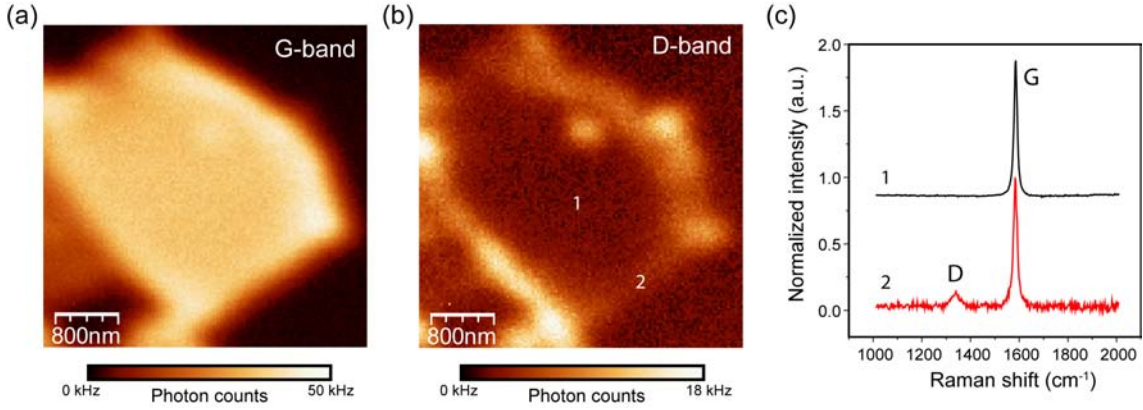


Figure 55: Confocal Raman G-band (a) and D-band (b) images of graphite in a scan area of $4 \times 4 \mu\text{m}^2$. The excitation source is HeNe laser at 632.8 nm and the power is 1.6 mW. G-band signals are detected over all the graphite surface while D-band signals are only at the edge. Spectra taken at the interior of the graphite marked with number 1 and at the edge of the graphite marked with number 2 are shown in (c). D-band in the spectrum is only observed at the edge.

presented in Figure 56 taken from the same graphite flake as in Figure 55. Figure 56(a) is the topography of this flake appearing almost uniform in the interior while the corner is folded towards the inside. Determined by the topographic height of about 5 nm in the cross-section in Figure 56(c) taken along the white dashed line in Figure 56(a), the number of layers are approximately 13 taking account the different interaction between the glass and graphene (the distance between graphite layers are 0.33 nm) [208]. Figure 56(b) is simultaneously obtained image representing signal around 690 nm, where D-band is located. Unfortunately, the graphite flake appears a dark shadow compared with the background signal. The shadowing because of the luminescence of the gold tip discussed in section 5.3 is dominated in the whole region covered by graphite. The cross-section (d) taken along the dashed line in Figure 56(b) shows the clear decrease of intensity into the interior of graphite.

However, a very weak stripe can be seen in the topography as pointed by the arrow in Figure 56(a). Zoom in images were made in the area marked with white rectangular as displayed in Figure 56(e) and (f). In both topography and D-band images, the stripe is clearly visualized. One possibility can be that the graphite has wrinkled because of cleavage forces during preparation or, there is a thin stripe in between the glass substrate and graphite that pushes up the graphite. In both case, this area can be considered as defect rich since the smooth surface has

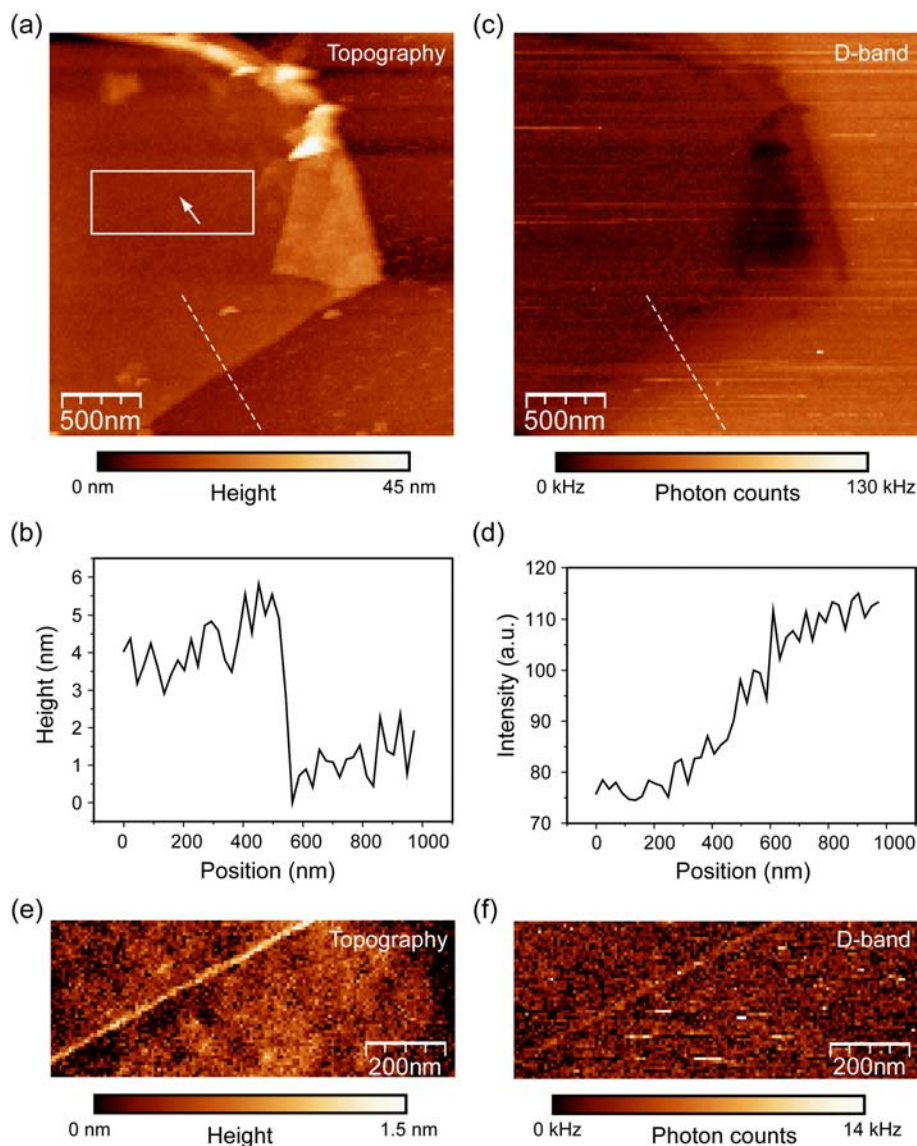


Figure 56: Simultaneously obtained topography (a) and D-band (b) images of a graphite flake. (c) and (d) are cross-sections taken along the white dashed line in (a) and (b), respectively. The topographic height of about 5 nm indicating there are approximately 13 layers. The graphite appears dark in the D-band image because of the tip artifacts. Topography (e) and near-field D-band (f) images taken in the area marked with rectangular in (a) showing a graphite wrinkle formed on the smooth surface.

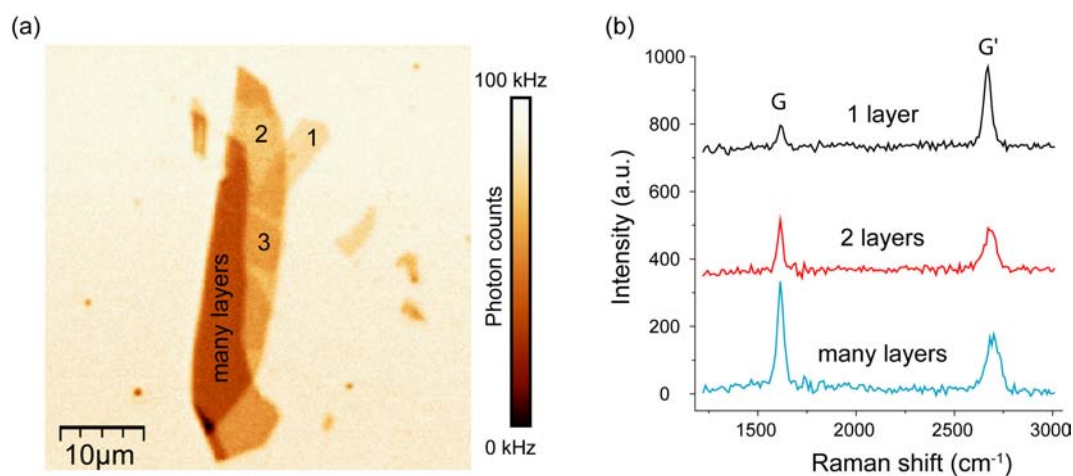


Figure 57: (a) Confocal Rayleigh scattering image of multilayer graphite consists of 1,2,3 and many layers using HeNe laser at 632.8 nm excitation in a scan area of $4 \times 4 \mu\text{m}^2$. The image contrast is proportional to the number of layers [208]. (b) Raman spectra of graphene sheet, 2 layers graphite and many layers graphite.

been disturbed, therefore a corresponding D-band image is observed.

Unfortunately, a single sheet of graphene is always accompanied with multilayer graphite during preparation. Figure 56(a) shows confocal Rayleigh scattering image of a flake consists of different number of layers of graphite, as indicated by the numbers labeled. Single graphene sheets can be easily identified by Raman scattering distinguished from the higher intensity and narrower band width of second-order G'-peak [211]. Figure 56(b) gives the Raman spectra from graphene, 2 layers graphite and many layers graphite, respectively. G'-peak changes in shape, width, and position for an increasing number of layers, reflecting the change in the electron bands via a double resonant Raman process [211]. Similar as Figure 56(b), near-field measurement on graphene gives negative contrast shadow. The strong luminescence from the gold tip as background signal covers the signal from the graphene. Higher energy excitation is required in order to increase the excitation efficiency and reduce the background from gold tip luminescence in the non-resonance wavelength range of gold plasmons. Further measurements with nanoscale resolution are worth to try to study optical properties at the edge of graphene as a function of the distance towards the edge, or different polarizations of the edge.

B Tip artifacts and near-field enhancement by a double tip

Images measured with an atomic force microscope are always a convolution of the probe geometry and the shape of the features being imaged as well as in TENOM. If the tip has been crashed, or has an undefined structure, we can often get a "double tip" effect, where both the tips are scanning the surface. This artifacts lead to wrong quantifications of the sample surface and distort the spectroscopic data due to the improper coupling between tip and incident field. Artifact therefore should be clearly identified for avoiding misinterpretation in near-field optical measurements.

As an example, Figure 58 presents the simultaneously obtained topography (a), near-field Raman scattering (b) and near-field PL (c) of DNA-wrapped nanotubes spin-coated on glass scanned by a double tip. The double tip is identified by the two parallel lines rendered by a single nanotube in the topography. However, in both near-field Raman scattering and PL images, the same nanotube appears as only a single nanotube. The cross-sections are taken along the dashed lines marked in images (a), (b) and (c), respectively. Remarkably, the peaks from Raman scattering and PL are located in between the two peaks from topography formed by the tips. Since near-field signals can reflect the enhanced incident field, the strongest fields are not at the tip apex but in between the two small tips. Similar structure, bowtie antennas in near-field measurements have been reported to enhance the sample signals with the enhanced and localized fields in between the two bowties [212–214].

In order to extract the involved strong confined electric field as excitation source from a double tip, in Figure 59, we illustrate the field distribution at the end of a tip consists of two protruding small tips using the method described in section 3.2. The SEM images of a real existing gold tip are served as a double tip model. This double tip was formed during the etching procedure already. A double tip can also be formed during scanning. First, when the polarization of the driving field is parallel to the tip, as shown in Figure 59(a), the charge density has highest amplitude on both tip ends lead to strong electric fields at the foremost of the tips. The total electric field is summed from the two tips thus the highest electric field occurs in the middle. As the distance between two tips gets larger, the field in between two tips however will get smaller and finally will be separated into two excitation fields. Since the distance of two nanotubes images (determined from the topography in Figure 58(d)) is smaller than 50 nm, we can also estimate the field confinement to be smaller than 50 nm. Second, although the contribution from the transverse mode of the focus is rather small, which is perpendicular to

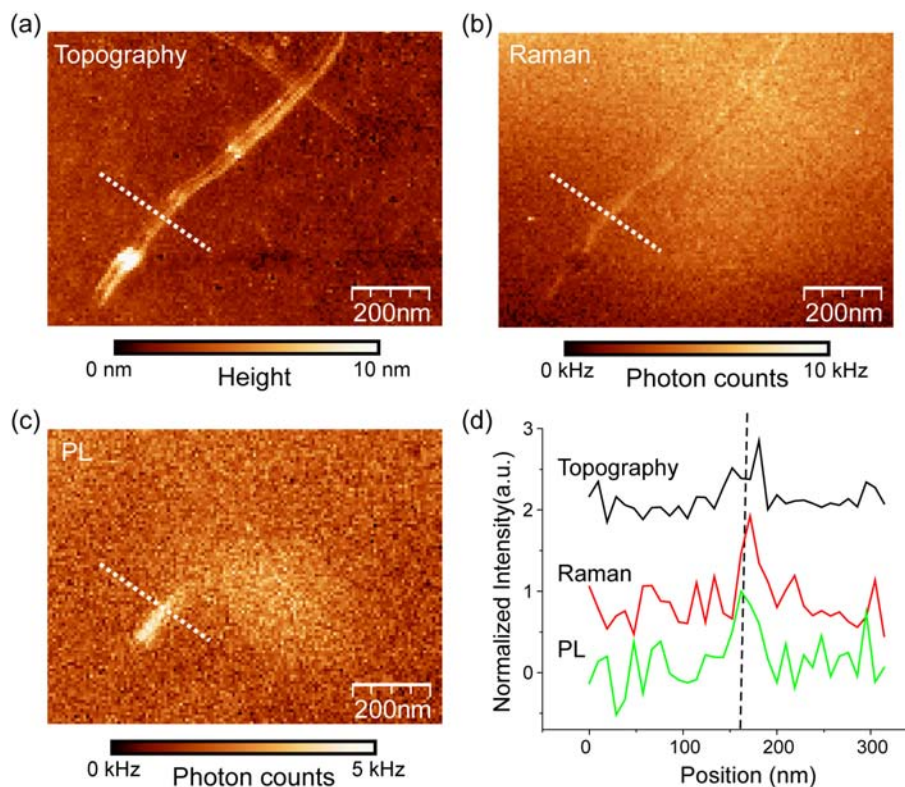


Figure 58: Simultaneously obtained topography (a), near-field Raman scattering (b) and near-field PL (c) of DNA-wrapped nanotubes spin-coated on glass scanned by a double tip. The excitation source is HeNe laser at 632.8 nm in radially polarized mode. Both tips scanned the nanotube giving two parallel lines rendered by a single nanotube. Near-field Raman and PL appear a single nanotube. (d) is cross-section taken along the dashed lines in (a), (b) and (c). The peak positions of Raman and PL are in between the two peaks of topography formed by two tips. Apparently, the enhanced signal occurs not at the tip apex but in between the two small tips.

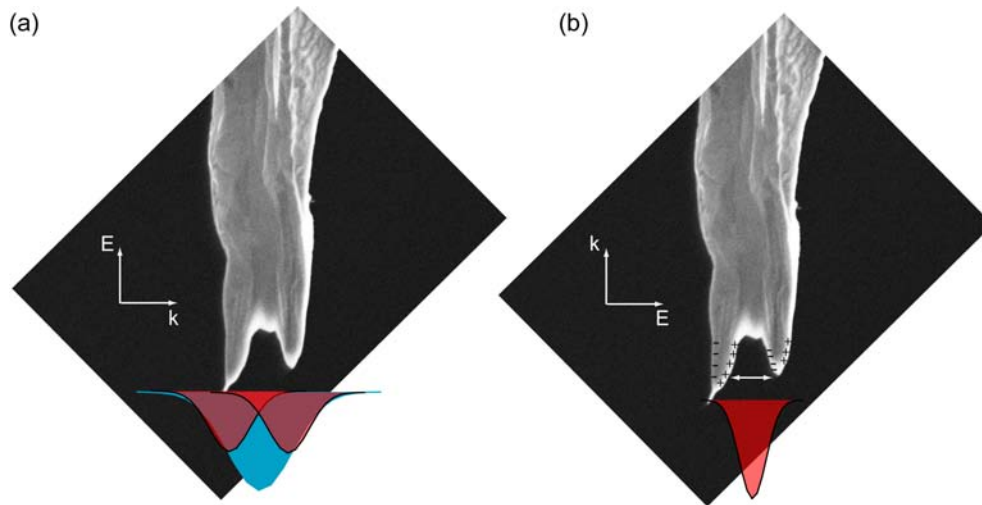


Figure 59: The double tip model is from a SEM image of a real gold tip consists of two protruding small tips. (a) The polarization of the driving field is parallel to the tip, from the contribution of the longitudinal field component. The total electric field underneath the double tip is summed by the fields from two small tips, which occurs in between the two tips. (b) The polarization of the driving field is perpendicular to the tip, from the contribution of transverse mode. Charges accumulate on the surface and form a strongest field in between two tips in the transverse direction.

the tip axis, in case of double tip, charges accumulate on the surface and form a strongest field in between two tips in the transverse direction, as illustrated in Figure 59(b). Considering both polarizations, the enhanced field for a double tip with small separation can still be considered as a single point excitation source. The field distribution as a function of tip-tip distance will be difficult to quantify by experiments, As the formation of double tips is all by accident up to now. Theoretical calculations will be helpful for understanding of some unusual phenomenons appeared in the experiments.

C Abbreviations

TENOM	Tip-enhanced Near-field Optical Microscopy
SWNT	Single-Wall Carbon Nanotube
1D	One-dimensional
2D	Two-dimensional
PL	Photoluminescence
DOS	Density of States
vHSs	van Hove singularities
oTA	Transverse Acoustic
iTA	in-plane transverse Acoustic
LA	Longitudinal Acoustic
oTO	out-of-plane transverse Optic
iTO	in-plane transverse Optic
LO	Longitudinal Optics
RBM	Radial Breathing Mode
BWF	Breit-Wigner-Fano
MD	Molecular density
NA	Numerical aperture
STED	Stimulated emission depletion
PLAM	Photo-activated localization microscopy
STORM	Stochastic optical reconstruction microscopy
SNOM	Scanning near-Field optical microscopy
AFM	Atomic force microscopy
SERS	Surface enhanced Raman scattering
SH	Second-harmonic
CCD	Charged coupled device
APD	Avalanche photodiode
FWHM	Full width at half maximum
FM	Frequency modulated
PLL	Phase locked loop
FIM	Field-ion microscopy
STM	Scanning Tunneling Microscopy
TEM	Transmission Electron Microscopy

PLE	Photoluminescence excitation
SDS	Sodium dodecyl sulfate
MMP	Multiple multipole
FRET	Fluorescence Resonance Energy Transfer
STS	Scanning Tunneling Spectroscopy

D Curriculum vitae

Personal Data

Name: Qian huihong

Sex: Female

Date of birth: 31, 05, 1980

Place of birth: Zhangjiagang, Jiangsu Province, People's Republic of China

Nationality: People's Republic of China

Education

PHD

06.2006-present

Department Chemie und Biochemie and CeNS, Ludwig-Maximilians-Universität München, Germany

03.2005-05.2006

Institute of Physical and Theoretical Chemistry, University of Tübingen, Germany

Master of Science 10.2002 — 11.2004

Institute of Physical and Theoretical Chemistry, University of Siegen, Germany

Master thesis: "Fluorescence and Raman studies on the same Single-Wall Carbon Nanotube"

Bachelor of Chemical engineering 09.1998 — 07.2002

Department of Chemistry and Chemical Engineering, Shanghai Jiaotong University, Shanghai, People's Republic of China

Bachelor thesis: "Studies on aggregating of cyanine dyes with different concentrations in solution"

School

09.1995 — 07.1998 Liangfeng Senior High School, Zhangjiagang, Jiangsu

09.1992 — 07.1995 Luyuan Junior High School, Zhangjiagang, Jiangsu

09.1986 — 07.1992 Luyuan Primary School, Zhangjiagang, Jiangsu

E Publications

During the course of my Ph.D research the following peer-reviewed papers have been published:

H. Qian, C. Georgi, N. Anderson, A. A. Green, M. C. Hersam, L. Novotny, A. Hartschuh, "Exciton transfer and propagation in carbon nanotubes studied by near-field optical microscopy", *Physica Status Solidi*, accepted (2008).

H. Qian, P. T. Araujo, C. Georgi, T. Gokus, N. Hartmann, A. A. Green, A. Jorio, M. C. Hersam, L. Novotny, A. Hartschuh, "Visualizing the Local Optical Response of Semiconducting Carbon Nanotubes to DNA-wrapping", *Nano Lett.* accepted (2008).

P. T. Araujo, I. O. Maciel, P. B. Pesce, M. A. Pimenta, S. K. Doorn, H. Qian, A. Hartschuh, M. Steiner, L. Grigorian, K. Hata, A. Jorio, "A The Relation Between Radial Breathing Mode Frequency and Tube Diameter for Pristine Single Wall Carbon Nanotubes and Environmental Effects", *Physical Review B* accepted (2008).

I. O. Maciel, N. Anderson, M. A. Pimenta, A. Hartschuh, H. Qian, M. Terrones, H. Terrones, J. Campos-Delgado, A. M. Rao, L. Novotny, and A. Jorio. "Electron and phonon renormalization at defect/doping sites in carbon nanotubes", *Nature Mater.*, submitted for publication (2008).

H. Qian, N. Anderson, C. Georgi, L. Novotny, A. Hartschuh, "Tip-enhanced optical microscopy", *Phil. Trans. R. Soc. Lond.*, submitted for publication (2008).

L. Song, A.W. Holleitner, H. Qian, A. Hartschuh, M. Dblinger, E.M. Weig, J.P. Kotthaus, "A carbon nano-filament-bead necklace", *Journal of Physical Chemistry B* accepted (2008).

H. Qian, C. Georgi, N. Anderson, A. A. Green, M. C. Hersam, L. Novotny, A. Hartschuh, "Exciton energy transfer in pairs of single-walled carbon nanotubes", *Nano Lett.* **8**, 1363 (2008).

C. Casiraghi, A. Hartschuh, E. Lidorikis, H. Qian, H. Harutyunyan, T. Gokus, K. S. Novoselov, A. C. Ferrari, "Rayleigh Imaging of Graphene and Graphene Layers", *Nano Lett.* **7**, 2711 (2007).

M. Steiner, H. Qian, A. Hartschuh, A. J. Meixner, "Controlling non-equilibrium phonon populations in single-walled carbon nanotubes", *Nano Lett.* **7**, 2239 (2007).

A. Hartschuh, H. Qian, A. J. Meixner, N. Anderson, L. Novotny, "Tip-enhanced optical spectroscopy of single-walled carbon nanotubes" in "Advances in Nano-Photonics", S. Kawata, V.M. Shalaev (eds.) (2007).

R. Korlacki, M. Steiner, H. Qian, A. Hartschuh, A.J. Meixner, "Optical Fourier Transform Spectroscopy of Single-Walled Carbon Nanotubes and Single Molecules", *Chem. Phys. Chem.* **8**, 1049 (2007) (cover article).

H. Qian, T. Gokus, N. Anderson, L. Novotny, A.J. Meixner, A. Hartschuh, "Near-field imaging and spectroscopy of electronic states in single-walled carbon nanotubes" *Phys. Stat. Sol. (b)*, **243**, 3146 (2006).

A. V. Failla, H. Qian, H. Qian, A. Hartschuh, A. J. Meixner, "Orientational imaging of sub-wavelength Au particles with higher order laser modes", *Nano Lett.* **6**, 1374 (2006).

A. Hartschuh, H. Qian, A. J. Meixner, N. Anderson, L. Novotny, "Tip-enhanced optical spectroscopy for surface analysis in bioscience", *Surface and Interface Analysis* (special issue on Biosurfaces) **338**, 1472 (2006).

A. Hartschuh, H. Qian, A. J. Meixner, N. Anderson, L. Novotny, "Nanoscale optical imaging of single-walled carbon nanotubes", *J. Lumin.* **119-120**, 204 (2006).

A. Hartschuh, H. Qian, A. J. Meixner, N. Anderson, L. Novotny, "Nanoscale optical imaging of excitons in single-walled carbon nanotubes", *Nano Lett.* **5**, 2310 (2005).

A. Hagen, M. Steiner, M. B. Raschke, C. Lienau, T. Hertel, H. Qian, A. J. Meixner, A. Hartschuh, "Exponential decay lifetimes of excitons in individual single-walled carbon nanotubes", *Phys. Rev. Lett.* **95**, 197401 (2005).

C. Gao, Y. Z. Jin, H. Kong, R. L. D. Whitby, S. F. A. Acquah, G. Y. Chen, H. Qian, A. Hartschuh, S. R. P. Silva, S. Henley, P. Fearon, H. W. Kroto, D. R. M. Walton, "Polyurea-functionalized multiwalled carbon nanotubes: Synthesis, morphology, and Raman spectroscopy", *J. Phys. Chem. B* **109**, 11925 (2005).

A. Hartschuh, H. N. Pedrosa, J. Peterson, P. Anger, H. Qian, A. J. Meixner, M. Steiner, L. Novotny, T. D. Krauss, "Single carbon nanotube optical spectroscopy", *Chem. Phys. Chem.* **6**, 577 (2005).

F Conferences and workshops

NIM-workshop on Interactions in Hybrid Nanosystems, Frauenwörth, Chiemsee, May 1-4, 2008

Poster: Exciton energy transfer in pairs of DNA-wrapped carbon nanotubes

IWEPNM 2007, International Winterschool on Electronic Properties of Novel Materials, Kirchberg, Tirol, Austria, 01.03. - 08. 03. 2008.

Poster: Exciton transfer and propagation in carbon nanotubes studied by near-field optical microscopy

Colloquium Spectroscopicum Internationale XXXV, Xiamen, China, 23.-27.09. 2007.

Oral presentation: Tip-enhanced Near-field Optical Spectroscopy of Carbon Nanotubes

NT07, eighth International Conference on the Science and Application of Nanotubes, Ouro Preto, Minas Gerais, Brazil, 24. 06. - 29. 06. 2007.

Poster: Nanoscale optical characterization of single carbon nanotubes

MSIN07, Metrology, Standardization and Industrial Quality of Nanotubes, Rio de Janeiro, Brazil, 22.06.2007

CeNS Winter School in Mauterndorf, Austria, "Nanosystems: From Quantum Devices to Biological Engines", Mauterndorf, Austria, 12. 02. - 16. 02. 2007.

Poster: Nanoscale optical imaging of single carbon nanotubes

NFO9, 9th International conference on near-field optics, nanophotonics and related techniques, Lausanne, Switzerland, 10. 09. -15. 09. 2006.

Oral presentation: High-resolution near-field optical spectroscopy of single-walled carbon nanotubes

International Linz Winter workshop on Single Molecule Biophysics, Linz, Austria 03. 02. -06. 02. 2006.

Poster: Nanoscale Raman and photoluminescence spectroscopy on individual Single-walled Carbon Nanotubes

DPC 2005,15th International Conference on Dynamical Processes in Excited States of Solids, Shanghai, China, 01.08. - 05.08.2005.

Oral presentation: Nanoscale Raman and photoluminescence spectroscopy on individual nanoobjects

Hauptversammlung der Deutschen Bunsen-Gesellschaft für Physikalische Chemie, Frankfurt, Germany, 05.-07.05.2005.

Poster: High Resolution Imaging and Spectroscopy of Single Carbon Nanotubes

SPM and Organic Materials XIII, Bielefeld, Germany, 06. 09- 08. 09. 2004.